Fall 12-2017

The Impact of Fe-Ti Oxide Concentration on the Structural Ridgity of the Lower Oceanic Crust, Atlantis Bank, Southwest Indian Ridge

Daniel Winkler
University of Southern Mississippi

THE IMPACT OF Fe-Ti OXIDE CONCENTRATION ON THE STRUCTURAL RIDGITY OF THE LOWER OCEANIC CRUST, ATLANTIS BANK, SOUTHWEST INDIAN RIDGE

by

Daniel Winkler

A Thesis
Submitted to the Graduate School,
the College of Science and Technology,
and the Department of Geography and Geology
at The University of Southern Mississippi
in Partial Fulfillment of the Requirements
for the Degree of Master of Science

December 2017

THE IMPACT OF Fe-Ti OXIDE CONCENTRATION ON THE STRUCTURAL RIDGITY OF THE LOWER OCEANIC CRUST, ATLANTIS BANK, SOUTHWEST INDIAN RIDGE

by Daniel Winkler

December 2017

Approved by:

_____
Dr. Jeremy Deans, Committee Chair
Assistant Professor, Geography and Geology

_____
Dr. Frank Heitmuller, Committee Member
Associate Professor, Geography and Geology

_____
Dr. Mark Puckett, Committee Member
Professor, Geography and Geology

_____
Dr. David Cochran,
Department Chair, Geography and Geology

_____
Dr. Karen S. Coats
Dean of the Graduate School

Published by the Graduate School

ABSTRACT

THE IMPACT OF Fe-Ti OXIDE CONCENTRATION ON THE STRUCTURAL RIDGITY OF THE LOWER OCEANIC CRUST, ATLANTIS BANK, SOUTHWEST INDIAN RIDGE

by Daniel Winkler

December 2017

Fe-Ti oxides are important components of oceanic core complexes (OCC) formed at slow-spreading mid-ocean ridges since Fe-Ti oxides are more susceptible to crystal-plastic deformation than silicate minerals. This study investigated the predicted relationship between the presence and concentration of Fe-Ti oxides and the presence and intensity of crystal-plastic deformation in gabbroic samples from Atlantis Bank, Southwest Indian Ridge (SWIR). Atlantis Bank is an oceanic core complex that formed through the exhumation of lower oceanic crust along a detachment fault. OCCs form along slow-spreading ridges and are characterized by the complex interactions between magmatism and lithospheric extension, thus making these complexes more susceptible to crystal-plastic deformation at higher temperatures. Atlantis Bank has been the focus of many scientific expeditions including: Ocean Drilling Program Holes 735B, and 1105A, International Oceanic Discovery Program Hole U1473A, and submersible studies. This study utilized samples from all three holes from near the seafloor to a depth of 1.5 km below the seafloor. This study calculated Fe-Ti oxide concentrations within the samples using the open source software package *Fiji* and statistically analyzed them using the open source software package *R*. The results indicate that Fe-Ti oxide concentration does correlate with crystal-plastic foliation (CPF) intensity, showing that 76.3% of samples

with 5% or more Fe-Ti oxides have a corresponding CPF value of 2 or more (porphyroclastic foliation to ultramylonitc). These results indicate that there is a relationship between Fe-Ti oxide concentration and the CPF intensity within the samples taken from Atlantis Bank, SWIR.

ACKNOWLEDGMENTS

Recognition is given to the organizations IODP, ODP, NSF, and USM for making this project possible. Specifically, I express my gratitude to Dr. Jeremy Deans for assisting with data collection and navigating through many layers of the IODP and ODP websites and data collection pages.

DEDICATION

I would like to recognize the staff at USM and my fellow graduate students for all their assistance and help through this process. Specifically, professor Dr. Jake Schaefer for initially aiding me with the *R* software. I would also like to recognize my wife, Jessica Winkler, and family for keeping me going and not letting me lose focus on the end goal of completing this study.

TABLE OF CONTENTS

LIST OF TABLES

LIST OF ILLUSTRATIONS

LIST OF ABBREVIATIONS

USM	The University of Southern Mississippi
MBSF	Meters below the seafloor
MBSL	Meters below sea level
MCC	Metamorphic core complex
OCC	Oceanic core complex
CCSF	Core composite depth below the seafloor
CPF	Crystal-plastic fabric
SWIR	Southwest Indian Ridge
IODP	International Oceanic Discovery Program
ODP	Oceanic Drilling Program
NSF	National Science Foundation

CHAPTER I - INTRODUCTION

1.1 Background

The purpose of this study was to determine how the Fe-Ti oxide content of gabbro formed in the lower oceanic crust affects the intensity and distribution of deformation, thus providing insight into the structural rigidity of the lower oceanic crust formed at slow-spreading mid-ocean ridges. Fe-Ti oxides, such as ilmenite and magnetite, are physically weak compared to silicates due to their generally lower tenacity (i.e., resistance to deformation) and ability to deform plastically at lower temperatures (Agar and Lloyd, 1997; Till Moskowitz, 2013). This inherent weakness suggests that their presence could facilitate the onset of deformation (i.e., preferentially partition strain) and contribute to an increase in its intensity (i.e., preferentially continue to accommodate strain). Therefore, a rock unit with low Fe-Ti oxide content should be more resistant to deformation than a rock unit of higher Fe-Ti oxide content, with all other variables and conditions remaining equal. Several workers (Atkinson, 1977; Agar and Lloyd, 1997; Dick et al., 2000; John and Cheadle, 2010) have suggested a link between the presence of Fe-Ti oxides and deformation; however, to date, none have clearly quantified the amount of Fe-Ti oxide in a suite of samples or compared the amount of Fe-Ti oxide to the extent of crystal-plastic deformation in a statistically significant manner. To test the possibility of this relationship between Fe-Ti oxides and degree of deformation, this study utilized image processing software called *Fiji* to determine the percent Fe-Ti oxide content of thin section images and compare them to each of the samples' degree of deformation. Possible questions to be answered could be: Would the presence of the Fe-Ti oxide minerals cause the deformation? What is the concentration of Fe-Ti oxides in gabbros at Atlantis Bank,

and how are the Fe-Ti oxides distributed throughout Atlantis Bank? Based on this what kind of correlation exists between the presence and concentration of Fe-Ti oxides and CPF and how does this vary across Atlantis Bank?

The study was conducted using 589 thin sections from drill core and data gathered by the Oceanic Drilling Program (ODP) Hole 735B, 32°43’S, 57°17’E, 1500m deep; ODP Hole 1105A, 32º43'S, 57º16'E, 160m deep; and the International Oceanic Discovery Program (IODP) Hole U1473A, 32°42’S, 57°17’E, 800m deep, on the Atlantis Bank oceanic core complex, Southwest Indian Ridge (SWIR) (Figure 1.1 C) (Shipboard Scientific Party, 1991; Pettigrew et al., 1999; Dick et al., 2000; MacLeod et al., 2017). Oceanic core complexes are dome-like complexes that formed during asymmetric spreading along slow-spreading ridges exposing lower crustal and upper mantle rocks along a detachment shear zone/fault. As these complexes are exhumed, basaltic magma is injected into the lower crust, thus creating a tight link between magmatism and deformation. Atlantis Bank is an oceanic core complex (OCC) formed along the Southwest Indian Ridge (SWIR), which is between the Antarctic and African tectonic plates (Figure 1.1 A&B). Oceanic core complexes can make up to 60% of the seafloor around slow-spreading ridges, such as the SWIR (Smith et al., 2008; Miranda and John, 2010). This simple fact makes OCCs, such as Atlantis Bank important for further study to gain a better understanding of how and why OCCs form as they are an integral part of oceanic crust formation. The main OCCs that have been studied, beyond just seafloor mapping, are: Atlantis Massif along the Mid-Atlantic Ridge, Atlantis Bank along the Southwest Indian Ridge, and Kane Mega Mullion along the Mid-Atlantic Ridge; also, Godzilla Mega Mullion located in the Parece Vela Basin in the Philippine Sea. Even

though these OCCs have been sampled extensively by either dredging or rock cores by the programs ODP, IODP and the National Science Foundation (NSF), there are some differences that make Atlantis Bank the more ideal choice for this type of study. Atlantis Bank is ideal for rheological studies due to the grain size of the rocks present, preservation of high-temperature microstructures due to rapid cooling (John et al., 2004; Mehl and Hirth, 2008) and the localized nature of Atlantis Bank's deformation (Shipboard Scientific Party, 1999; Miranda and John, 2010). Additionally, Atlantis Bank provides evidence for the interplay of magma intrusion and deformation, with the three holes providing a diverse distribution of samples both geographically and by depth.

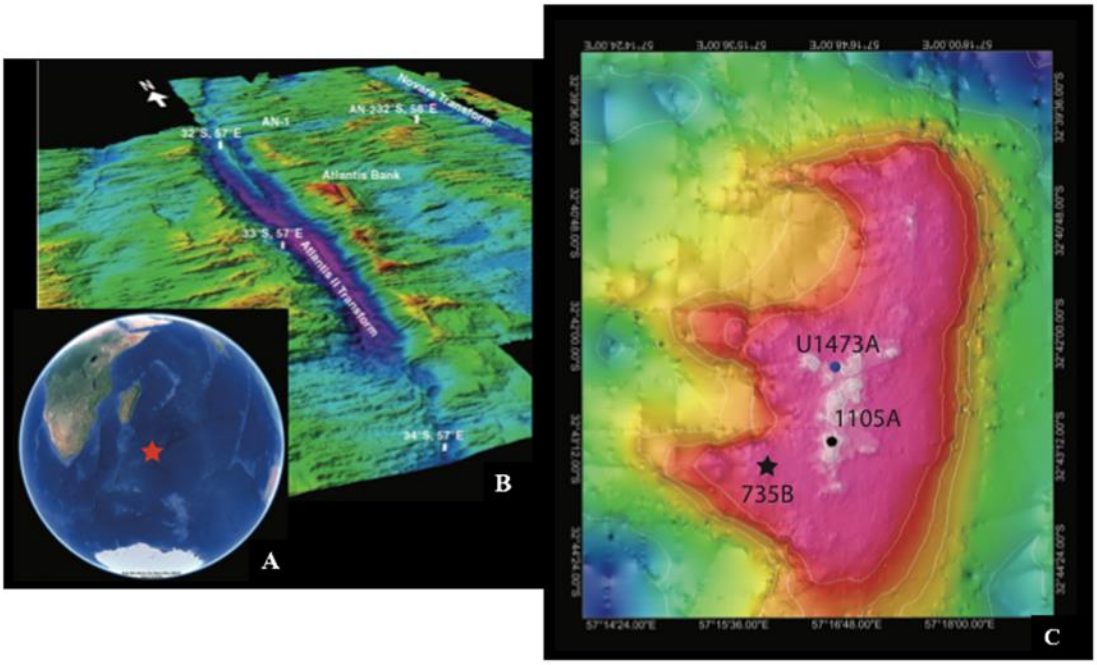

Figure 1.1 Study Area.

Study area for this project. A) Atlantis Bank's location on a global scale between the African and Antarctic plates. B) Atlantis Bank's location in relation to the nearby transform networks along the Southwest Indian Ridge (African plate to the west and the Antarctic plate to the east). C) Bathymetric map of Atlantis Bank with the locations of the three holes being used (ODP Hole 735B, denoted with a star, is the deepest hole at Atlantis Bank).

CHAPTER II – GEOLOGICAL INFORMATION

2.1 Geologic Setting

Mafic rocks, such as basalt and gabbro, dominate the oceanic crust, with some inclusions of felsic veins and a few sections with limited amounts serpentinite. The general sequence of the lithologic units that comprise oceanic crust is based on crust formed at fast-spreading ridges and ophiolites (Figure 2.1); however, depending on how the oceanic crust formed and evolved there could be lithologic units that are structurally omitted from this sequence. For example, the crustal sequence found at Atlantis Bank along the SWIR, and many other oceanic core complexes, is missing the basaltic sequences, including pillow basalts, basaltic lava flows, and sheeted dike complexes, at the seafloor, and instead have exposures of gabbro at the seafloor (Dick et al., 1991; 2000; 2016; MacLeod et al., 2017). The reason for this variation is related to the mid-ocean ridge rate of spreading.

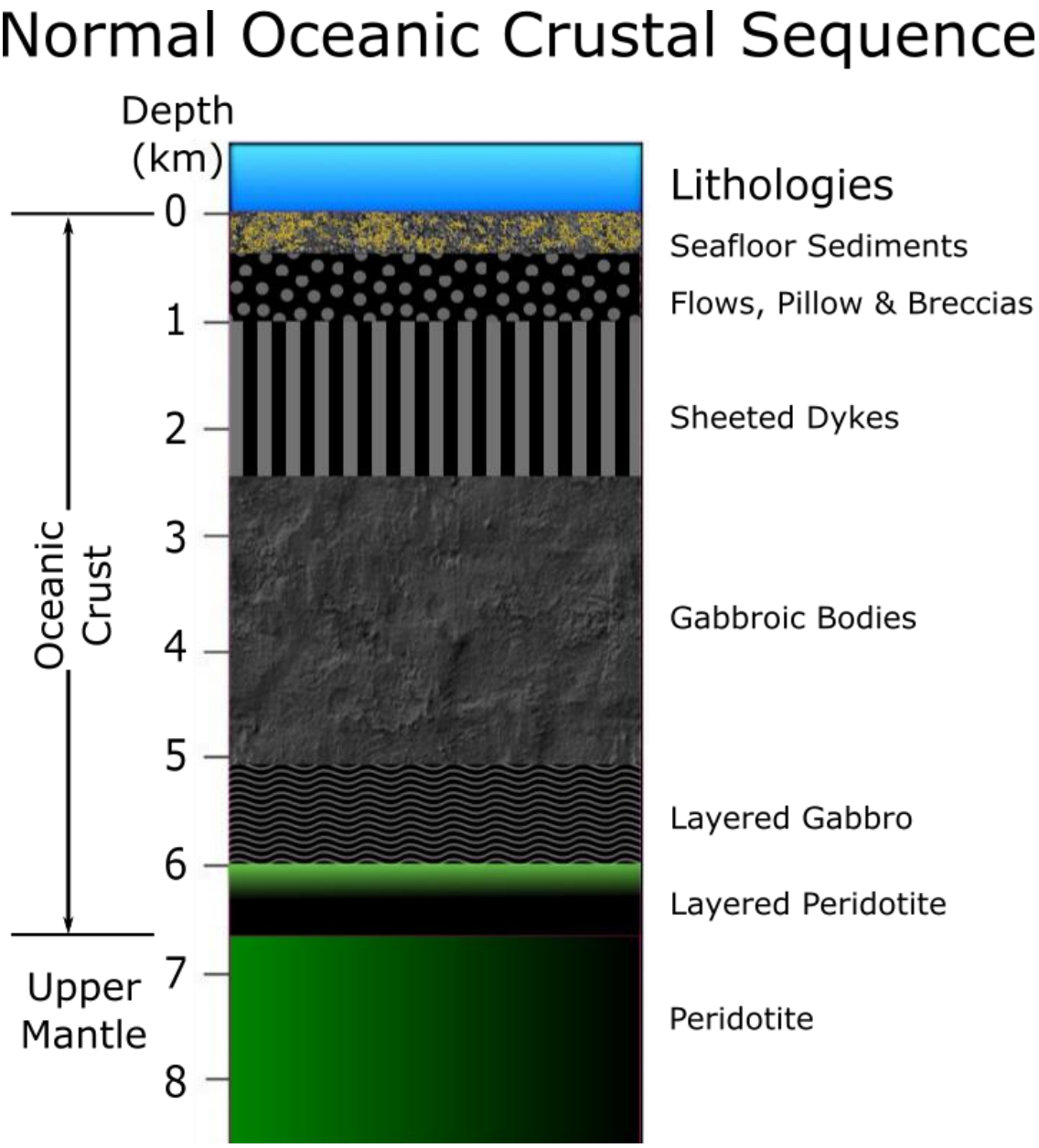

Figure 2.1 Oceanic Lithologic Sequence

Lithologic sequence expected for oceanic crust.

Mid-ocean ridges are part of the last stage of continental rifting created from the influence of the convective forces within the Earth's mantle that are expressed by the formation of continental rifts that rip apart continents. Once the continents get far enough apart, an ocean basin will form in the topographically low area that is created between

them by the rift. At this stage the surficial rift would, if it continues to rift, become a mid-ocean ridge and begin production of oceanic crust. These ridges can have many different characteristics that are controlled by various factors ranging from length of the ridge, rate of spreading and mantle influence. On Earth, the longest plate boundaries are divergent and include many different spreading ridges of varying length and influence with the three major systems being: The East Pacific Rise, the Mid-Atlantic Ridge, and the Indian Ridge system (Southeast Indian Ridge, Mid-Indian Ridge, and SWIR).

All oceanic spreading ridges are responsible for the creation of oceanic crust; each ridge creates this material at differing rates and in different ways. There are generally two classes of spreading ridges based on spreading rate: fast spreading ridges and slow spreading ridges. The main fast spreading ridge is the East Pacific Rise (EPR); fast ridges such as the EPR are responsible for the majority of the oceanic crust production on Earth. Fast spreading ridges also form the normal oceanic crust lithologic sequence as illustrated in Figure 2.1. While fast spreading ridges may be responsible for the production of more ocean crust, there are more slow spreading ridges by comparison of number and length, which would therefore make them an integral portion of the Earth's crustal system and plate tectonic cycle.

2.1.2 Slow-Spreading Ridges and Core Complexes

There are broadly two types of core complexes, metamorphic core complexes (MCC) and oceanic core complexes (OCC); the two types are very closely tied to the environments in which they are found. The MCC variety is found in continental crustal regions, and the OCC variety is found in oceanic crustal regions; both structures however, are created by lithospheric extension. A core complex is characterized by

exposures of plutonic and metamorphic rocks that have been exhumed structurally higher than younger volcanic and sedimentary rocks (Lister and Davis, 1989). The mechanism of this structural change is a detachment shear zone/fault system, with the driving force behind the characteristic dome shape being uplift facilitated by isostatic rebound associated with the crustal thinning and intrusion of magma into the footwall of the complex. Detachment faults/shear zones are identified based on their distinctive dome-shaped and imbricated fault surfaces that cap the core complex (Karson, 1999; Smith et al., 2008; Miranda and John, 2010).

There are two basic processes that drive the normal fault system to create the domed structure seen at core complexes; heterogeneous crustal thinning and unloading imbalance by way of isostasy. Crustal thinning is driven by the extensional nature of the system where the hanging wall portion is continually removed and thinned from over the foot-wall leading to exhumation of the footwall. This extension leads to the creation of a 'negative' load over the footwalls crust; the absence of the hanging wall's overburden and intrusion of magma facilitates the isostatic rebound of lithosphere uplifting the footwall further to attempt to balance out the negative load (Wernicke et al., 1988; Lister and Davis, 1989).

With increasing depth, there is a change from mainly brittle deformation near the seafloor to mainly ductile deformation (e.g., Schroeder and John, 2004; Miranda and John, 2010). This distribution of deformation also indicates that ductile deformation is more distributed in the footwall compared to a more restricted zone of brittle deformation. The rocks that form and cool near the ridge axis form high strain zones including mylonite, then if cooled further during exhumation will be overprinted by semi-

brittle structures like faults, fractures, and cataclasite. The detachment shear zone/fault system therefore provides a down-temperature record of the exhumation of the lower crust/upper mantle.

2.1.3 Geologic Setting of Atlantis Bank, Southwest Indian Ridge

The area of interest for this study is Atlantis Bank, which is a bathymetric high located along the SWIR, with a current depth of ~700 meters below sea level (MBSL); the top of Atlantis Bank is a wave cut platform indicating it was near sea level at some point in the past before subsiding to its current depth (Dick et al., 2000; Schwartz et al., 2005, Palmiotto et al., 2013). The SWIR is a tectonic boundary between the African and Antarctic tectonic plates, and is classified as a slow-spreading ridge because the total spreading rate is lower than 55 mm/year; the SWIR has a current average rate spreading rate of ~22 mm/year (Schwartz et al., 2005; Sauter et al., 2011). The gabbro present at Atlantis Bank and ODP Hole 735B, ODP Hole 1105A and IODP Hole U1473A exhibit characteristics different from those seen at fast-spreading ridges and most ophiolite complexes (Dick et al., 2000). When Atlantis Bank formed ~11 Ma, the spreading ridge had an asymmetrical spreading rate with the African plate spreading ~5.5 mm/year almost due north and the Antarctic plate, with Atlantis Bank, spreading ~8.5 mm/year due south (Hosford et al., 2003; Baines et al., 2008). Atlantis Bank is located ~18 km east of the present-day transform zone, the Atlantis II Fracture zone, and ~100 km south of the SWIR axis and has a plateau exposed over an area of ~300 km^2 (Allerton and Tivey, 2001; Baines et al., 2008). Atlantis Bank was calculated to have formed between 10 and 13 Ma as determined by paleomagnetic records; this age has been corroborated by U/Pb isotopic dating of zircons in evolved gabbros and felsic dikes (John et al., 2004; Schwartz

et al., 2005; Baines et al., 2009; Rioux et al., 2016). Atlantis Bank's domed shape was created by a detachment fault/shear zone associated with OCC formation, which caused the exhumed lower oceanic crust to be exposed at/near the sea floor. The hanging wall of Atlantis Bank is located to the north on the African plate, whereas the domed bathymetric high of Atlantis Bank is the footwall portion of the OCC (Dick et al., 1991; 2000; Allerton and Tivey, 2001; Schwartz et al., 2005; Baines et al., 2008; Miranda and John, 2010).

CHAPTER III – STUDY AREA INFORMATION

3.1 Deformation at Atlantis Bank, Southwest Indian Ridge

The distribution of deformation around and within Atlantis Bank varies greatly, which is demonstrated with the distribution of crystal-plastic fabric intensity for all three holes (Figure 3.1) (Shipboard Scientific Party, 1991; 1999; Miranda and John, 2010; MacLeod et al., 2017). Atlantis Bank has a record of magmatic deformation, crystal-plastic deformation, and brittle deformation. Magmatic deformation occurs while the magma, which contains melt and crystals, facilitates movement in the form of crystal alignment without any internal strain of the mineral crystals, such as bending or warping. Magmatic deformation occurs during intrusion and emplacement of basaltic igneous material. As the crustal column cools and is exhumed, crystal-plastic fabrics form along the detachment shear zone and at depth to accommodate extension at the ridge. When the complex was exhumed, enhanced cooling occurred from the introduction of sea water and the structure started to undergo brittle deformation as the main deformation mechanism, which overprinted the ductile deformation in the upper ~100 meters of the detachment shear zone (Schroeder and John, 2004; Miranda and John, 2010; Hansen et al., 2013).

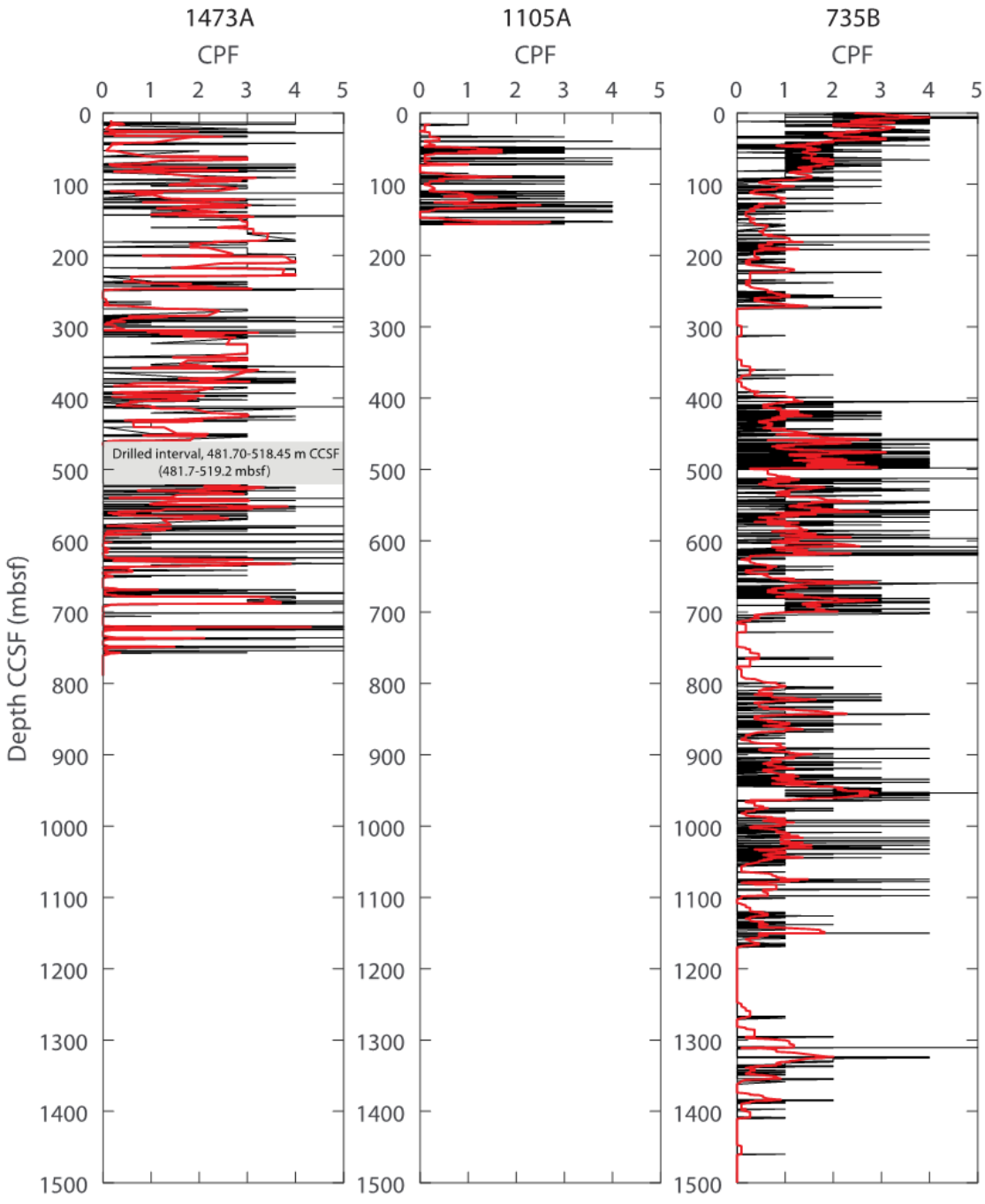

Figure 3.1 Crystal plastic intensity by depth within each hole at Atlantis Bank

Down-hole bore plot of crystal-plastic deformation intensity in all three bore holes at Atlantis Bank. The fabric intensity scale was developed by the Shipboard Scientific Party (1999) with the rank of 0 equaling no crystal-plastic deformation and a rank of 5 equaling to an ultramylonite. (CCSF = Core composite depth below seafloor; CPF = Crystal plastic fabric intensity) The red curve is a thickness corrected running average; the black curve is the raw intensity values.

3.2 ODP Holes 735B, 1105A and IODP Hole U1473A

All three holes were drilled on Atlantis Bank's plateau at various depths. ODP Hole 735B was drilled by Leg 118 and Leg 176 to a depth of ~1.5 km (Figure 1.1 c). Leg 118 was conducted in 1987 and drilled the first 500 m of the hole, then Leg 176 drilled the last 1000 m in 1997 (Shipboard Scientific Party, 1991; Dick et al., 1991; 2000). ODP Hole 1105A was drilled by Leg 179 to a depth of ~160 m (Figure 1c) (Pettigrew et al., 1999). IODP Hole U1473A was drilled by Expedition 360 to a total depth of ~800 m (Figure 1.1 c) (MacLeod et al., 2017). The rocks of Atlantis Bank can be divided into four major groups including olivine-bearing gabbro, micro gabbros, Fe-Ti oxide-bearing gabbros and gabbronorites, and minor felsic veins; with the principle lithology being olivine gabbro (Figure 3.2) (Scientific Party 1991; Pettigrew et al., 1999; Dick et al., 1991; 2000; 2016; MacLeod et al., 2017). The gabbroic lithology of Atlantis Bank contains silicate mineral phases such as plagioclase feldspar, pyroxene, amphibole, and olivine. The Fe-Ti oxide mineral phases present within these gabbros are rutile, magnetite, and titanite. Atlantis Bank is in an area that has multiple igneous intrusions of various sizes, as well as numerous fault/shear zones (Dick et al., 2000).

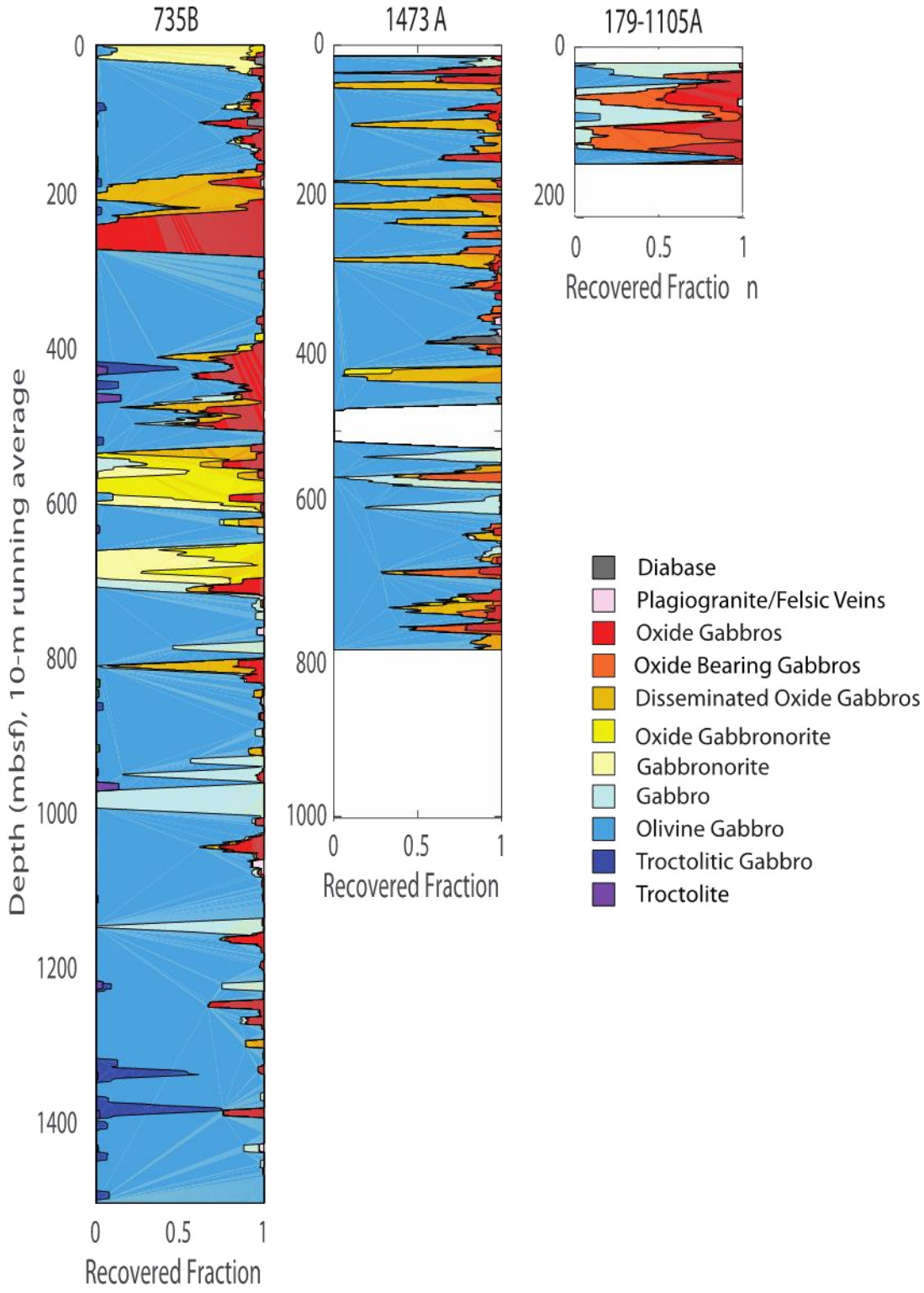

Figure 3.2 Plot of Principle Lithologies within each hole at Atlantis Bank

Plot of lithology for each hole with depth. The lithology is plotted as a running average. Modified after MacLeod et al. (2017).

3.3 Fe-Ti Oxide Localization

Silicate mineral phases are generally more structurally rigid when compared to Fe-Ti oxide mineral phases under identical temperature and pressure conditions **(**Atkinson, 1977; Siemes and Hennig-Michaeli, 1985; Till and Moskowitz, 2013). Therefore, a rock unit with no or low Fe-Ti oxide content should be more resistant to deformation than a rock unit of higher Fe-Ti oxide content, with all other variables and conditions remaining unaltered. Within Atlantis Bank, there are several discrete shear zones and faults throughout the core as well as multiple veins that cross cut throughout the holes (Shipboard Scientific Party, 1991; Shipboard Scientific Party, 1999; Dick et al., 2000; MacLeod et a., 2017). These fault planes and shear zones along with potential fracture fields create areas of weakness or void space for enriched melts and/or hydrothermal fluids to be injected into, which occurs throughout the formation of OCCs. Both areas are potential sites of Fe-Ti oxide localization and further deformation and/or faulting.

Fe-Ti oxides commonly make up a reasonably small percentage of gabbroic rocks, typically less than 5% (Dick et al., 2000). Additionally, Fe-Ti oxides in mafic systems are some of the last phases to crystalize (Bateman, 1951). However, at Atlantis Bank and by default other OCCs, Fe-Ti oxides can potentially make up as much as 30% of a sample (Agar and Lloyd, 1997; Dick et al., 2000; MacLeod et al., 2017). This dramatic difference in Fe-Ti oxide percent is attributed to Fe-Ti oxide concentration that can occur during the final cooling stages of magma crystallization. There are two main ideas on how Fe-Ti oxides concentrate before a magma or rock is completely solidified: 1) late gravitative liquid accumulation and 2) filter pressing/residual liquid injection

(Bateman, 1951; Charlier et al., 2015). Late gravitative liquid accumulation is the process that is at work within a body of melt that has begun cooling, but has yet to completely solidify. As more and more minerals crystallize out of the melt body, the fluid becomes more and more enriched in more evolved phases such as Fe (3+) and Ti. This Fe-Ti oxide enriched melt will have a higher density (Natland, 2002) and will settle towards the base of the melt body. Any melt not as enriched in Fe and Ti would also be less dense, thus forcing the lighter more buoyant silica rich melt and phases like plagioclase towards the top. This type of concentration, should the system completely cool without deformation, would show bands of Fe-Ti oxide mineral phases with the less dense and/or more evolved mineral phases within or above it. There may also be evidence in the silica phases of the gravity driven movement in the form of bent or potentially fractured mineral crystals if the melt is overpressure, or cause minerals such as Fe-Ti oxides to form bands.

Filter pressing/residual liquid injection works within units of rock that are nearly completely solidified with dispersed Fe-Ti oxide-enriched fluids throughout its pore space. If a rock with Fe-Ti oxide-enriched fluid within its pore spaces were to experience a change in pressure/stress this would force, or press, the Fe-Ti oxide-enriched portion into an area of lower pressure (Bateman, 1951). The most common avenues of escape for these Fe-Ti oxide enriched fluids would be along fractures or fault planes created by stress. In some cases, they are associated with dikes or veins of felsic material (Natland, 2002). Both methods of Fe-Ti oxide localization could be at work within a region such as Atlantis Bank.

Other forms of Fe-Ti oxide localization are caused by the influences of external forces on a magma body or rock body. Bodies of magma that are exposed to changes in

pressure can become differentiated, causing the magma to become enriched in heavy elements such as Fe (3+) and Ti which increases potential for Fe-Ti oxide development (Dick et al., 2000). A rock body can have the Fe-Ti oxide content that is present become localized by the effects of deformational forces. These deformational forces can force the weaker Fe-Ti oxides, that are more easily mobilized, into zones of lower pressure around more resistant silicate phases creating pressure shadows (Charlier et al., 2015). Both these localization methods create zones of increased Fe-Ti oxide content which could preferentially partition strain in the future.

3.4 Preferential Deformation of Fe-Ti Oxides

There has been a strong association reported between deformation intensity and Fe-Ti oxide concentration (Shipboard Scientific Party, 1999; Dick et al., 2000; Natland, 2002); however, some workers have suggested there is no link or the link is no different from non-Fe-Ti oxide bearing rocks (e.g., Miranda and John, 2010). The concentration of Fe-Ti oxide phases within shear zones has been interpreted to indicate a potential link between late-stage melt migration and deformation (Agar and Lloyd, 1997; Dick et al., 2000). There have been studies on Fe-Ti oxides to infer how they respond to stress. Fe-Ti oxides while under constant temperatures of ~200-400°C will deform via diffusion (Coble) creep, or dislocation creep depending on the strain rate that corroborates with a crystallographic preferred orientation (Atkinson, 1977; Hennig-Michaeli and Siemes, 1983). While both methods of creep facilitate movement at relatively low temperatures in Fe-Ti oxides there are distinct differences between them that need to be pointed out. Diffusion (Coble) creep facilitates the movement of vacancies along grain boundaries, which produces a net flow of material and sliding of grain boundaries (Passchier and

Trouw, 2005; Twiss and Moores, 2007). However, dislocation creep is the movement of dislocations (planar defects) within a mineral through the crystal lattice rather than around it (Twiss and Moores, 2007). This knowledge can be used to confirm that deformation is a facilitator of Fe-Ti oxide concentration by forcing the more susceptible Fe-Ti oxides to move around the more rigid silicates (e.g., Duchesne, 1996; Charlier et al., 2015). Studies have stated that there is no connection between Fe-Ti oxide concentration and preferential deformation. Miranda and John (2010) noted that based on their samples collected along the seafloor of Atlantis Bank, the oxide-bearing samples were not preferentially deformed, with deformation being equally exhibited in Fe-Ti oxide bearing and non-Fe-TI oxide bearing compositions (Miranda and John, 2010).

3.5 Sample Distribution

One of the major concerns for this type of study is sample distribution. In order for this study to be effective, adequate sample distribution within each hole need to provide a comprehensive representation of the relationships present within them. Overall, this entire study analyzed 589 thin section samples, which on average is one sample every 4.1 meters. Below, the sample distribution is described for each hole. These sample locations will provide a wide distribution of core samples across the Atlantis Bank platform ranging from near the seafloor to the base of each hole, up to 1.5 km below the seafloor.

3.5.1 IODP Hole U1473A

Figure 3.3 shows the sample distribution of the thin sections used from IODP Hole U1473A. This plot shows that the thin sections are a good representation of the recovered core at IODP Hole U1473A; there are however gaps in this coverage from

~469-520 mbsf and at ~760-790 mbsf. The sample gap from ~469-520 mbsf was caused by drilling without coring due to technical problems caused by the rock being heavily fractured and clay-rich representing a fault zone. The gap at the base of IODP U1473A is due to a lack of sampling within this sample suite. The ~10 meter gap at the top of IODP Hole U1473A was caused by spudding the hole so there is no recovery.

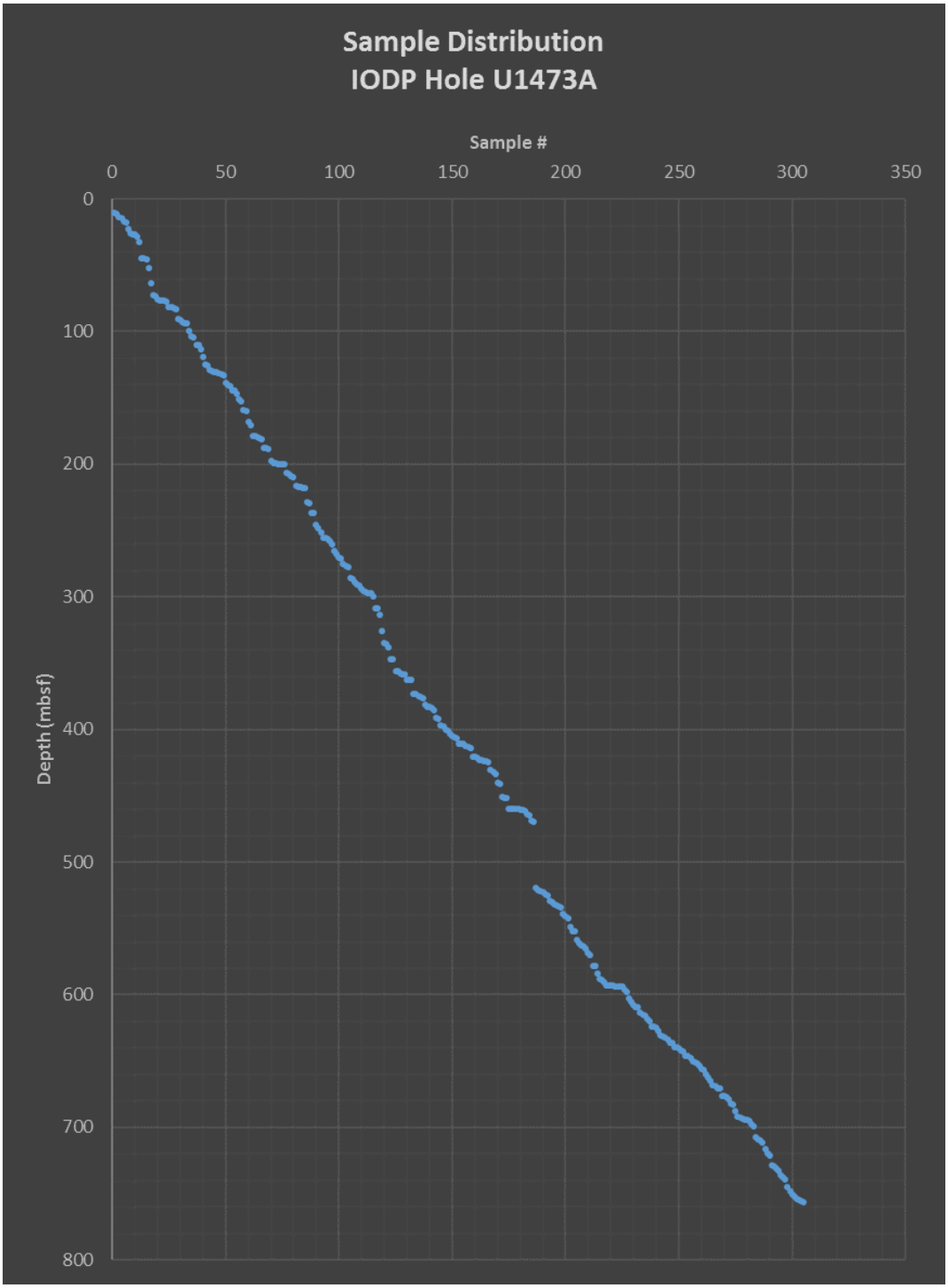

Figure 3.3 Plot of sample distribution within IODP Hole U1473A

This plot illustrates the sample distribution of the thin sections analyzed by this study within IODP Hole U1473A. Based on the plot it can be observed that there is a well-distributed sampling of the core with the gaps in coverage being from 469-520 mbsf and ~760-790 mbsf within IODP Hole U1473A.

3.5.2 ODP Hole 1105A

The samples used from ODP Hole 1105A range from 16 to 157 mbsf without any large gaps. There are however, a few smaller gaps throughout the recovered core's sample distribution (Figure 3.4). The sample gaps within ODP Hole 1105A are explained by two different causes: 1) spudding of the hole accounts for lack of recovery from 0-16 mbsf; and 2) highly fractured and faulted zones. The other sample coverage gaps are explained by faults running through the core area; there were five fracture zones, two of which were identified as faults. They were noted at 112 mbsf and 127 mbsf, both of which had an area around them of about 5 meters where no core was recoverable, which is expressed in the sample distribution.

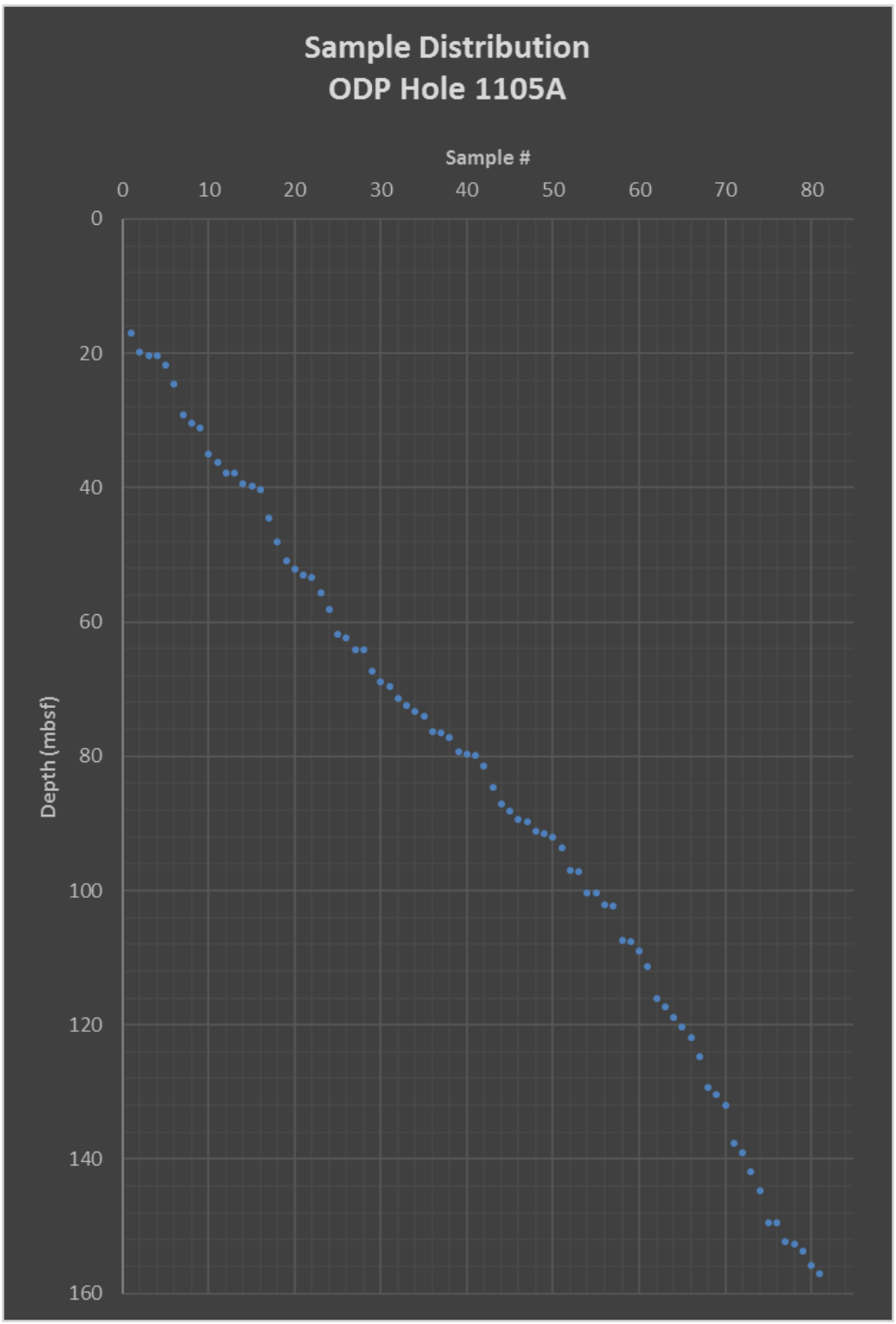

Figure 3.4 Plot of sample distribution within ODP Hole 1105A

This plot illustrates the sample distribution of the thin sections analyzed by this study within ODP Hole 1105A. Based on the plot it can observed that there is a good distribution of samples gathered for the analysis of this hole.

3.5.3 ODP Hole 735B

The samples used from ODP Hole 735B range from 0.02-1500.96 mbsf (Figure 3.5). There are however, three gaps: one is from ~90-120 m, the second is from ~400-450 m, and the third gap is from ~1200-1285 m. All three of these gaps are not due to a lack of recovery, but were caused by a lack of obtainable samples at the time of this study. This problem is more prevalent in the upper 500 m of the hole collected during Leg 118 since only 50 shipboard sections can be loaned from IDOP at a time.

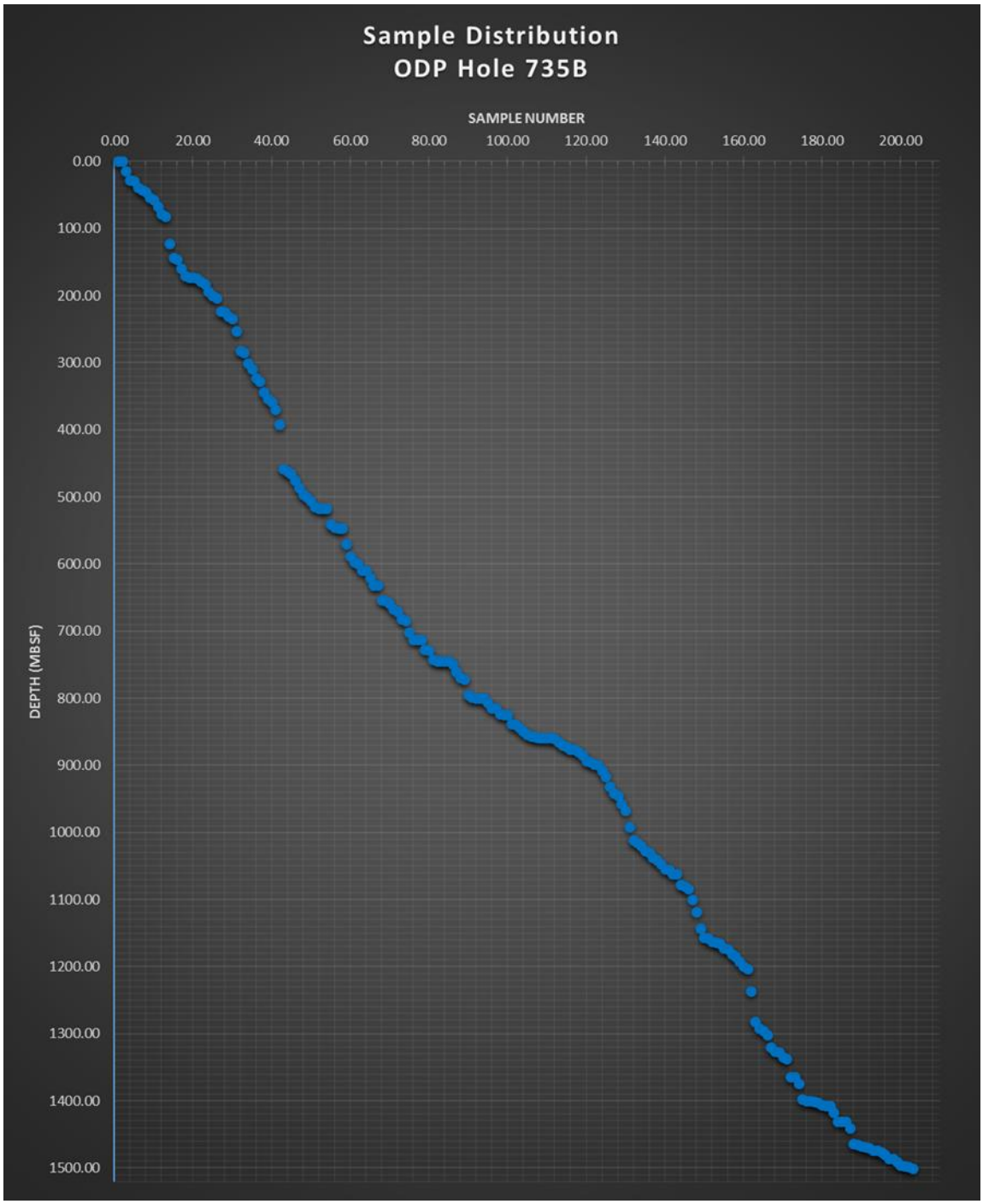

Figure 3.5 Plot of sample distribution within ODP Hole 735B

This plot illustrates the sample distribution of the thin sections analyzed by this study within ODP Hole 735B. This plot shows that there are samples distributed throughout the entire hole aside from three locations: ~80-120 mbsf, ~400-450 mbsf, and ~1200-1300 mbsf.

CHAPTER IV – METHODS

4.1 General Methods

An analysis of the Fe-Ti oxides for each thin section was conducted to produce an estimation of the percentage of Fe-Ti oxides present. This percentage was calculated using the image processing software package *Fiji* (Schindelin et al., 2012), a form of the ImageJ software, which is used for image based analysis (Schneider et al., 2012). *Fiji* was used because it allows for the analysis of images based on individual pixel values using a pixel value threshold. Given that the Fe-Ti oxides are opaque, the *Fiji* software can be used to readily isolate them from other mineral phases, specifically non-opaque minerals, by using a pixel value threshold. The calculated percent Fe-Ti oxide phases was then compared to the degree of deformation in the sample by comparing it with published deformation logs from the appropriate ship records for each hole. This study conducted this image analysis on 589 thin section images from IODP Hole U1473A, ODP Hole 735B, and ODP Hole 1105A.

4.1.1 Image Analysis

To use the *Fiji* software package to delineate samples and isolate the Fe-Ti oxides, each sample had to go through a process that made them usable within the software. The process was as follows: first the images were converted from a color image to a greyscale image (Figure 4.1). Once the image was converted into an 8-bit greyscale image, the next step was to delineate the sample from the background thin section glass, so only the sample was analyzed. This delineation was accomplished by using the Polygon and Crop tools built into the *Fiji* software (Figure 4.2). The Polygon tool is the best choice for delineating the sample because it offered the most control when creating

the region of interest. Once the image was cropped a more accurate outline was created compared to simply using the Rectangle tool. This step was crucial since most of the samples used were not perfectly rectangular. Next, the brightness and contrast settings of the image were adjusted; this was accomplished by using the Brightness/Contrast tool within *Fiji* (Figure 4.3). The adjustment of the image's brightness/contrast was necessary because it facilitated a sharper contrast between the Fe-Ti oxide and the non-Fe-Ti oxide phases present (ilmenite, magnetite from olivine, pyroxene, plagioclase, and alteration minerals) within the thin sections. Once the brightness and contrast settings were reached to optimize the identification of Fe-Ti oxides, the next step was to isolate the Fe-Ti oxide phases from the rest of the thin section to determine the relative percentage of Fe-Ti oxides in each sample. This was achieved by utilizing the Threshold tool built into the *Fiji* software (Figure 4.4). The Threshold tool allowed for the Fe-Ti oxide phases to be isolated from the non-Fe-Ti oxide phases by adjusting the threshold values until only the Fe-Ti oxides were highlighted (Figure 4.5). This step needed to be executed as precisely as possible because the Threshold tool was specifically isolating individual pixels that match the threshold criteria being set. This was a critical step, since *Fiji's* Threshold tool does not differentiate between what is Fe-Ti oxide and what is a dark patch of alteration. This lack of differentiation was why it was important to check the 8-bit grayscale image to the original color image to make sure that only the Fe-Ti oxides were highlighted. Given the highlighted area, *Fiji* then calculated various outputs, including area, length, mean, mode, and other parameters. *Fiji's* Measure tool bases those measurements on the highlighted pixels that were isolated by the given Threshold values (Figure 4.6). For this study, the Measure tool was utilized to find the area of the Fe-Ti oxides within the sample

as compared to the area of the entire sample (Figure 4.7). It is important to note that before using the Measure tool, the settings for the measurements needed to be adjusted so that *Fiji* only included the threshold pixels for the Fe-Ti oxide area calculation. This was accomplished by using the steps and tools shown in Figure 4.8.

The values calculated during the image processing were recorded in a Microsoft Excel spreadsheet to facilitate ease of data organization and interpretation. The values that are reported in this study include the brightness/contrast values, threshold values used, and percent concentration of Fe-Ti oxides in each sample. Table 1 has examples of the types of values that were collected using *Fiji*.

Table 4.1 *Fiji* Image Analysis Output Example

	Brightness/Contrast Values		Threshold Values		Measured area (pixels)		
Label	Low	High	Low	High	total area	output	% oxide
360-U1473A-2R-1-W 120/121-TSB	0	160	0	45	7928245	986182	12.43884
360-U1473A-2R-2-W 25/30-TSB	0	150	0	100	12251769	21040	0.17173
360-U1473A-3R-1-W 79/85-TSB	0	150	0	12	10392169	575986	5.5425
360-U1473A-3R-2-W 89/98-TSB	0	130	0	66	11867805	11066	0.093244
360-U1473A-3R-4-W 40/42-TSB	0	170	0	100	8644120	24561	0.284135
360-U1473A-3R-4-W 64/67-TSB	0	140	0	82	8413599	2413	0.02868
360-U1473A-4R-1-W 68/73-TSB	0	100	0	38	11304587	3442	0.030448
360-U1473A-4R-3-W 40/44-TSB	0	55	0	150	9849885	150845	1.531439

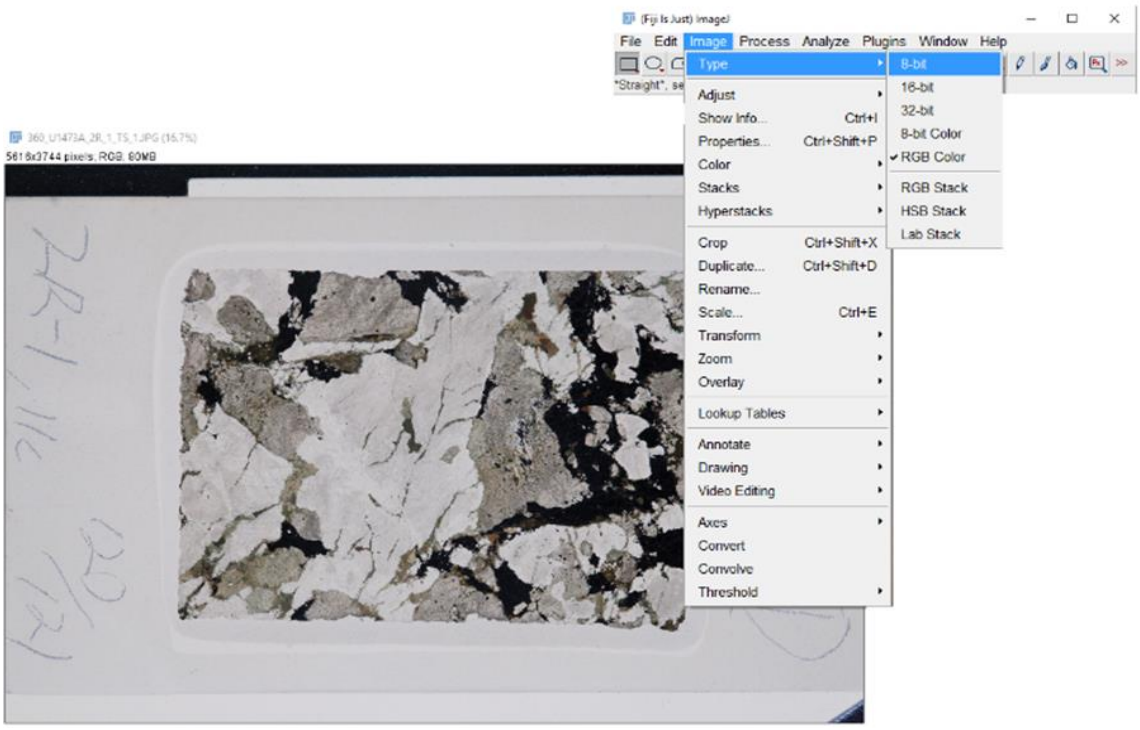

Figure 4.1 Image Color Conversion

The image after importing into *Fiji*. The image was converted into a greyscale image by utilizing the image converter to change it into an 8-bit greyscale image. The red words represent the tabs/tools used in *Fiji* to complete the task described. *Fiji* steps: Image → Type → 8-bit

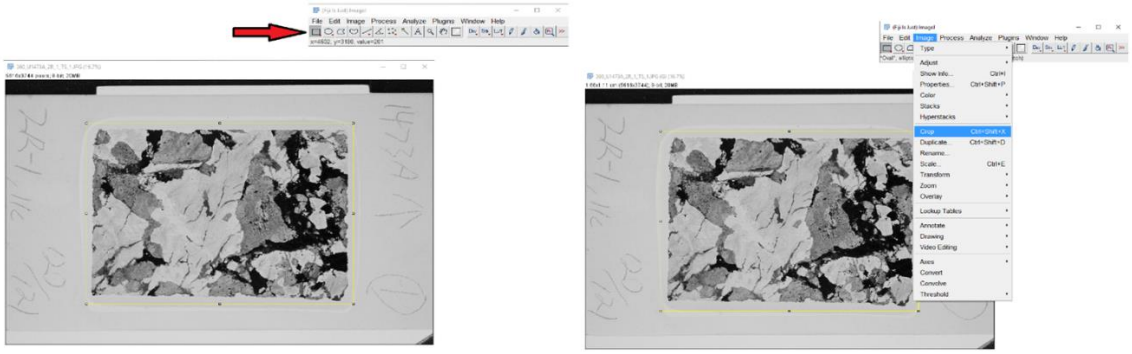

Figure 4.2 Region of Interest Delineation

Once the image was converted to an 8-bit image, the next function preformed was to create an area of interest using two tools. First, the Polygon tool was used to outline the area of interest (the sample) and second, the Crop tool was used to isolate the created region. *Fiji* steps: 1st – polygon tool 2nd -Image → Crop

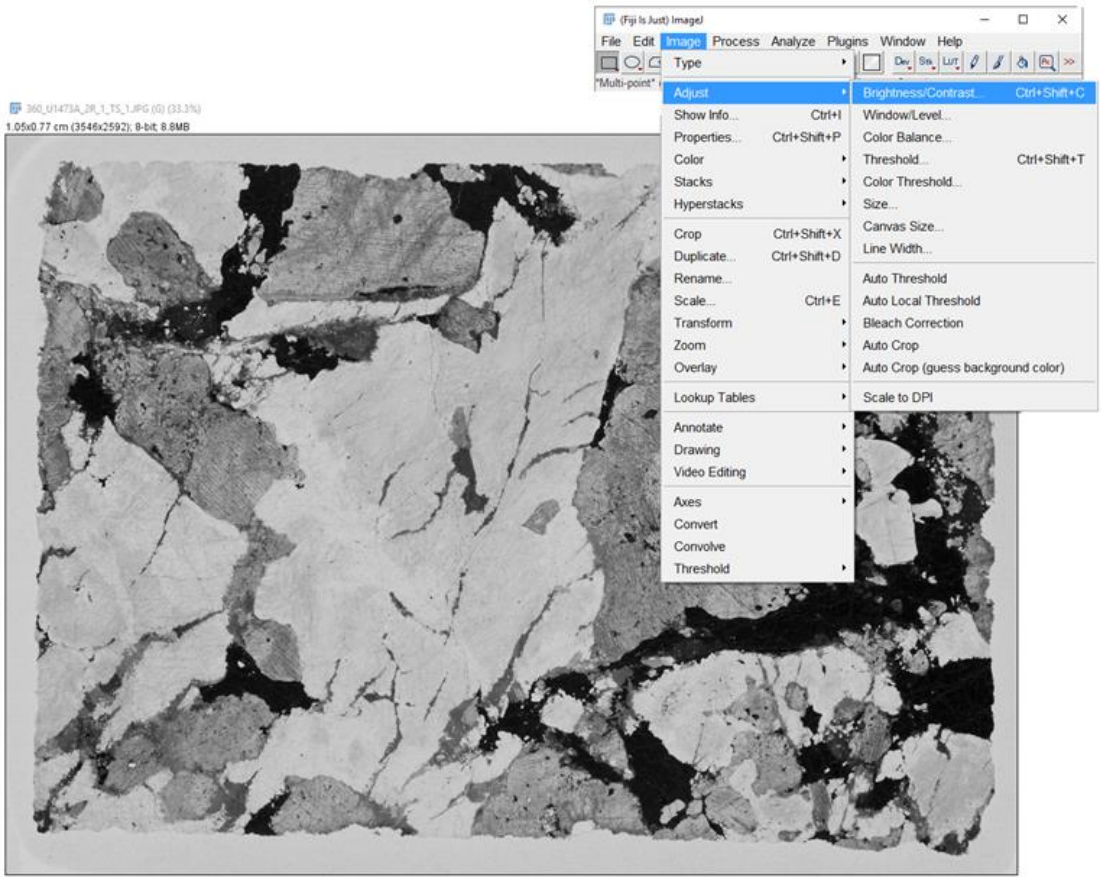

Figure 4.3 Brightness/Contrast Adjustment

To see the oxides more clearly, the image brightness and contrast values were adjusted using the Brightness/Contrast tool. *Fiji* steps:

Image → Adjust → Brightness/Contrast

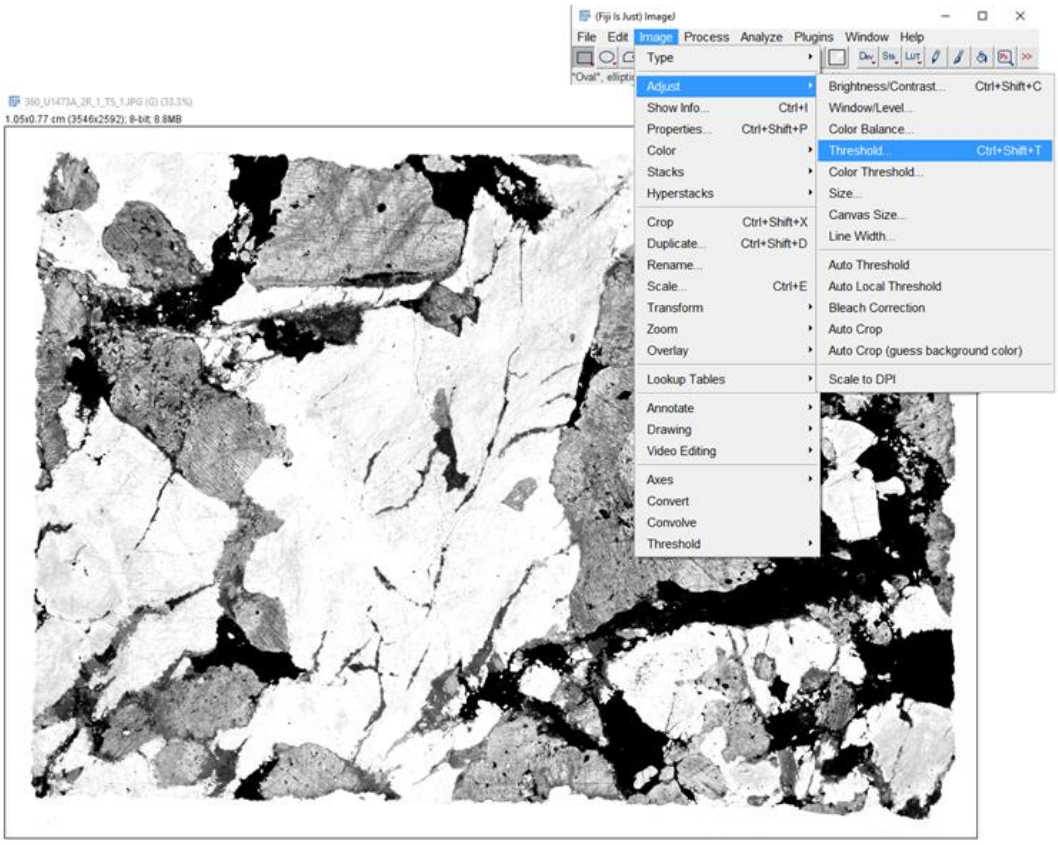

Figure 4.4 Threshold Tool

The *Fiji* software allows for the isolation of darker pixels, the Fe-Ti oxide phases, from lighter pixels, the non-Fe-Ti oxide phases, by using the Threshold tool. *Fiji* steps: Image → Adjust → Threshold

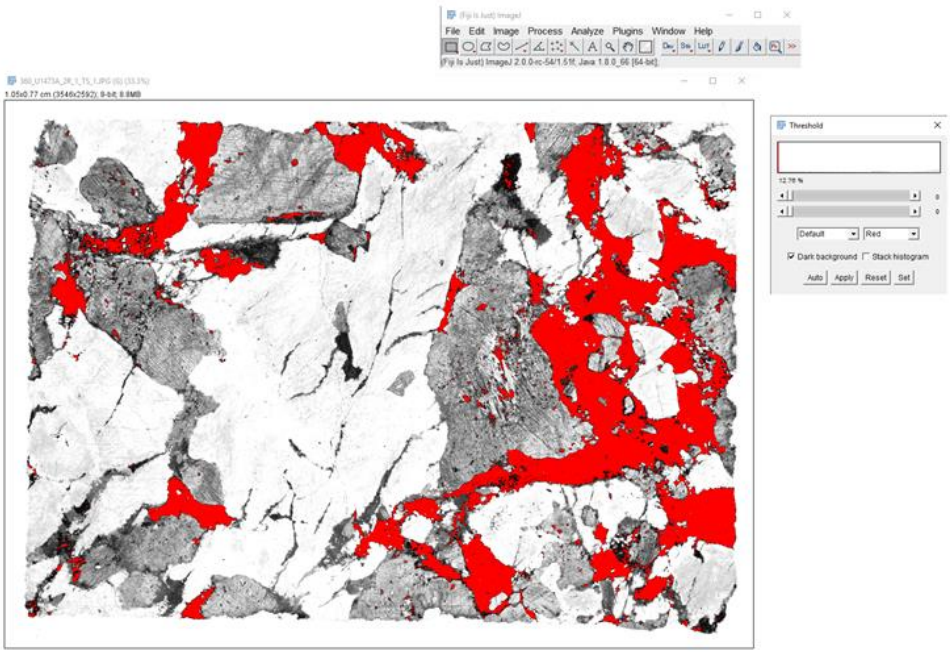

Figure 4.5 Threshold Adjustment

Threshold values can be manipulated within *Fiji* in such a way that only the desired pixels are highlighted; this allowed for the darker pixels, Fe-Ti oxides, to be measured and compared to the total thin section area.

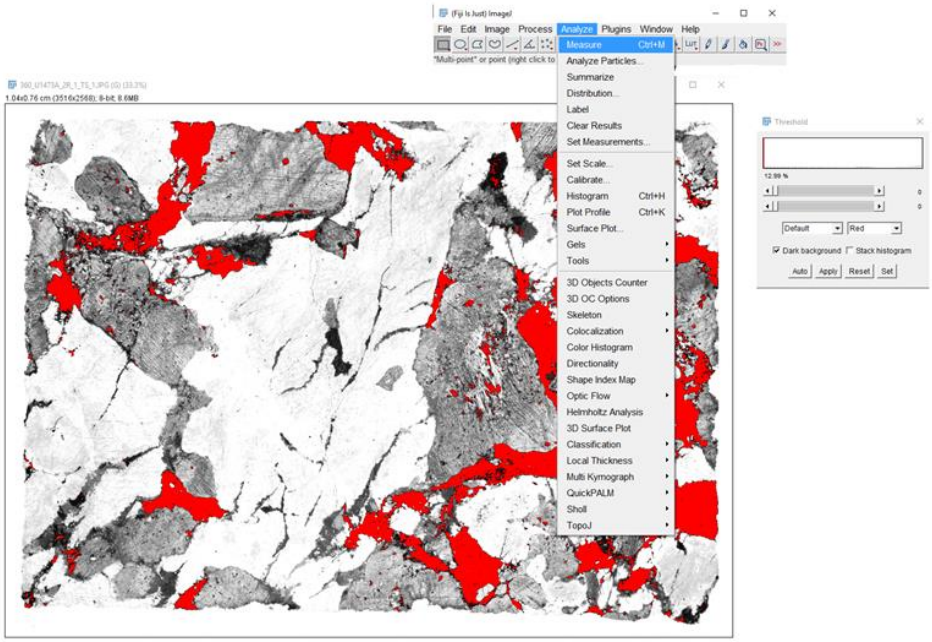

Figure 4.6 Measure Tool

Fiji's Measure tool was utilized to find the area taken up by the highlighted pixels (i.e., area of Fe-Ti oxides) and the area of Polygon tool (i.e., area of the thin section). *Fiji* steps: Analyze → Measure

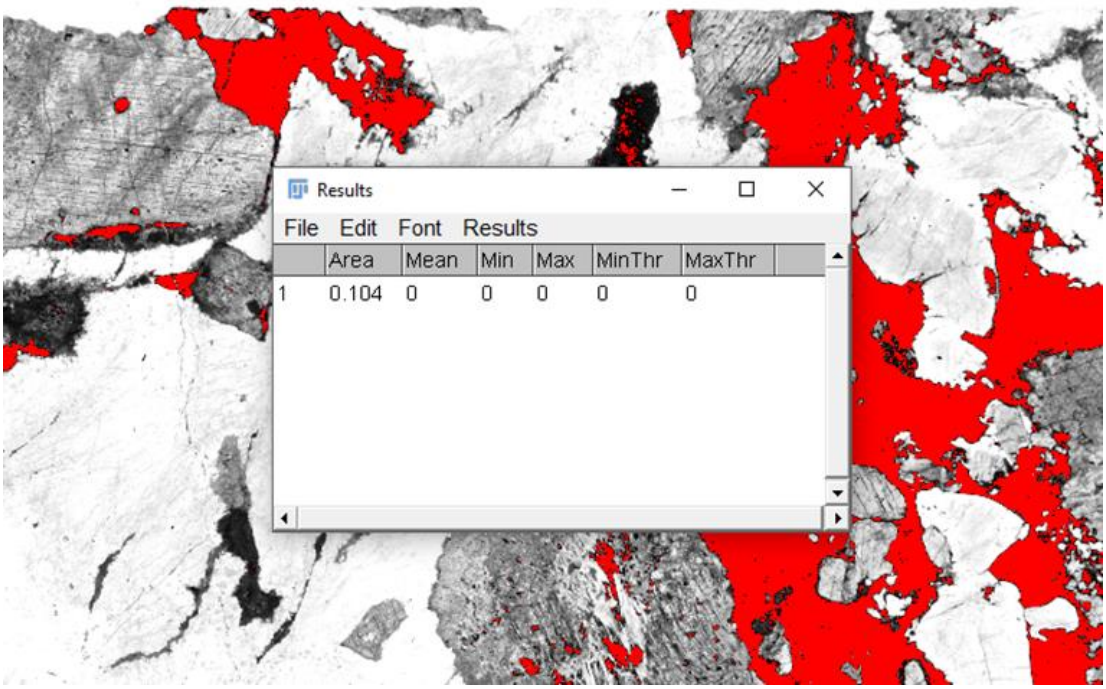

Figure 4.7 Measure Tool Output

Fijis measure tools output was used to find the area of the highlighted sections and this value was compared to the overall area to calculate Fe-Ti oxide phase percentage.

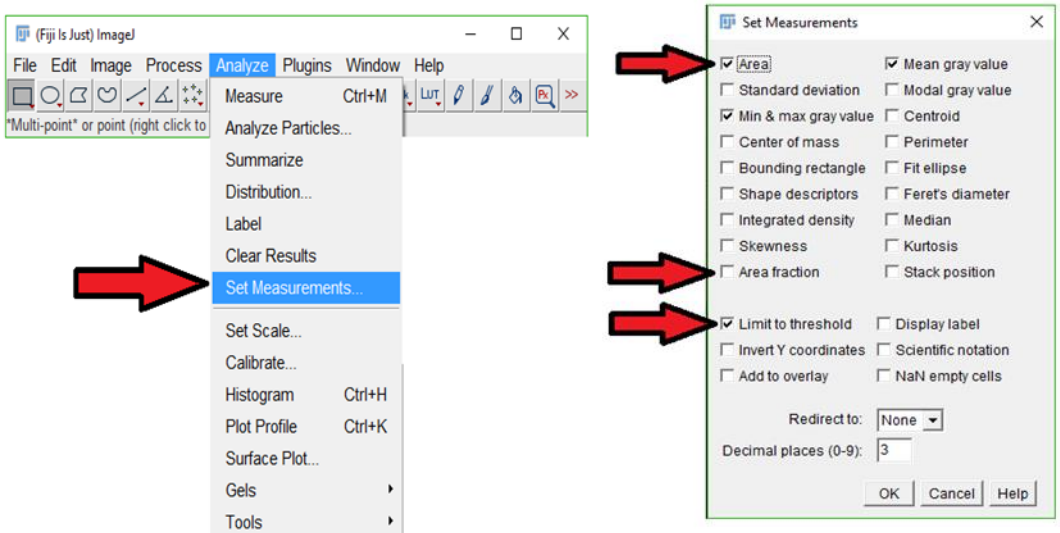

Figure 4.8 Measurement Settings

To receive the desired outputs from *Fiji's* Measure tool, the correct filters and application within the Measure tools menu needed to be selected (or deselected). *Fiji* steps: Analyze → Set Measurements This study used Area, Area Fraction, and Limit to Threshold

4.1.2 Error Analysis

The calculated percent Fe-Ti oxides in a sample was dependent on several factors that can lead to over- or under-estimation. These factors may include: 1) quality of the thin section image, 2) overall size of the Fe-Ti oxide minerals/mineral clusters, 3) delineation method, and finally 4) human error (e.g., brightness/contrast values and threshold values used). The issue of thin section image quality is rooted in the fact that *Fiji* is only as accurate as the user's inputs, which are based on the perception of the image; an image of poor quality can cause accuracy issues. Figure 4.9 is an example of poor image quality. While both images in Figure 4.9 were being processed, the software could not distinguish between the glass fractures on the thin section slides and the opaque Fe-Ti oxides. This was especially prevalent in 360-U1473A-11R-3 63-65cm where there were Fe-Ti oxide clusters along the slide fractures. There was a total of 3 thin section from ODP Hole 735B that had carbon films applied to them in order to run them through a scanning electron microscope. There was, however, a side effect of this carbon film that caused the thin sections to be artificially darker than the others, pushing the operating limits of the *Fiji* software. For *Fiji* to produce the most accurate results, the user needs to input the best quality and resolution images possible. This is important to increase the ability to determine where a dark non-Fe-Ti oxide mineral ends and an Fe-Ti oxide mineral begins. If the image is of low quality, this boundary can become blurred, which can influence the accuracy of the area calculation. Additionally, alteration phases are often dark or opaque, and can lead to false inclusion. By having better quality images, the alteration can be more readily identified and eliminated from the analysis by carefully comparing the original image and thresholded image during the thresholding process.

In some of the thin section images, the Fe-Ti oxide clusters are large interconnected pods/bands, making them easy to identify. Figure 4.10 illustrates an example of this. However, in other examples this is not the case and the oxides are in small clusters scattered throughout the sample, and in some cases, they are juxtaposed to dark non-Fe-Ti oxide phases such as amphibole (Figures 4.10 and 4.11). When this is the case, it can become difficult to distinguish the Fe-Ti oxide clusters from the amphiboles during the threshold phase of the analysis, which can then affect the percent area accuracy.

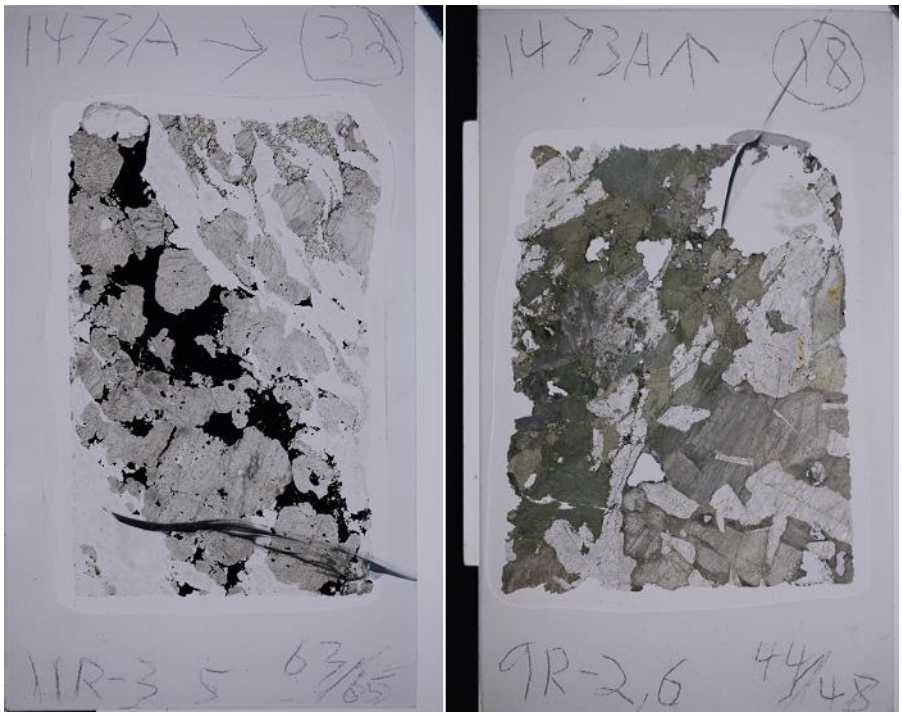

Figure 4.9 Examples of Poor Quality

Images of two separate thin section samples (360-U1473A-11R-3 63-65cm on the left, and 360-U1473A-9R-2 44-48cm on the right) that have been damaged thus affecting their image quality; this is an example of why image quality is important.

The 'human' factor is based on perception of the thin section samples while adjusting parameters such as the brightness and contrast or threshold values. The final adjustment for any of these three control values is based on an individual's perception of

the sample being analyzed. Another individual may utilize a different set of control values that look better to that individual, which would in theory affect the calculated percent area of the Fe-Ti oxide phases. This type of error, however, can be reduced by careful comparison of the threshold image to the thin section image, so only the Fe-Ti oxide phases are analyzed.

4.1.3 Alternative Method Testing

To demonstrate why the threshold method is the preferred method for delineating a sample for this type of analysis, there were several other methods tested to estimate the Fe-Ti oxide percent. The methods tested were the Binary tool method and the Wand tool method; the results of these tests can be found in the sections to follow.

4.1.3.1 Binary Method Test

The first alternative method tested was the Binary method. This method has some similarities to the threshold method but with critical differences. While both the Binary and Threshold methods convert the thin section image into a greyscale, there is a crucial difference between the two. Unlike the Threshold method described above, which takes different shades of white, grey and black and makes a certain grey value black, the Binary method produces a black and white image with no gray values. There is no distinction between the dark mineral phases, such as amphibole or pyroxene, and the opaque Fe-Ti oxide mineral clusters, since any relatively dark phase or opaque phase is converted into a black pixel. To illustrate this, the Threshold and Binary methods were completed on a thin section (Figure 4.10). To exhibit how this can create issues the image analysis of thin section sample 360-U1473A-3R-1-TS-3 had both the Binary method and the Threshold method conducted on it. The Binary method calculated Fe-Ti oxide

concentrate is 15.4%, which is more than double the Threshold methods calculation of 6.6%. This is clearly because there is no distinction between the dark non-Fe-Ti oxide phases and the opaque Fe-Ti oxide phases.

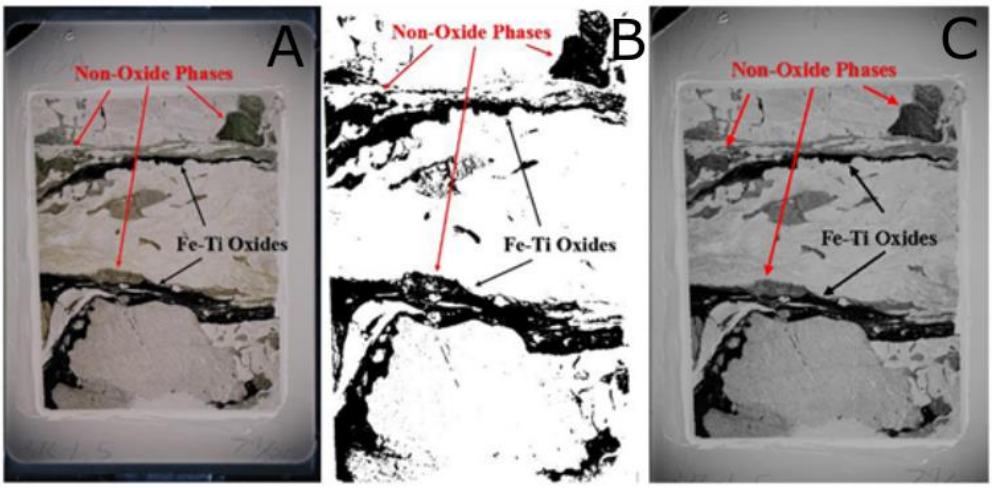

Figure 4.10 Binary Method Comparison

A) The above image is of thin section 360-U1473A-3R-1-TS-3. Original image in *Fiji* where there is clearly a distinction between the non-Fe-Ti oxide phases such as amphibole and the Fe-Ti oxides (labeled with red and black labels respectively). B) Same thin section image that has had the Binary filter from *Fiji* used on it. While using the Binary method, there would no longer be this distinction between the mineral phases. C. Threshold method, mineral phase differentiation is still possible.

4.1.3.2 Wand Method Test

The second alternative method tested was the Wand/individual cluster selection method. This method utilizes *Fiji's* Wand tool to selectively highlight individual Fe-Ti oxide mineral clusters, one-by-one to measure the area, then each cluster would have to be added together to calculate an overall percent area. There are drawbacks to using this method which mainly stem from how the Wand tool works within the *Fiji* software's framework. The Wand tool works by selecting clusters of pixels with the same pixel color value. It is important to note, however, that it will only select interconnected pixel clusters, not any and every cluster of identical pixel value across an area. For this reason,

the Wand method could work rather effectively on thin section images such as the one in Figure 4.10, since the Fe-Ti oxides are large interconnected clusters. However, not all thin sections have large interconnected Fe-Ti oxide mineral clusters. For example, Figure 4.11 illustrates where the major drawbacks for this method come to fruition. After reviewing Figure 4.11, two major issues became apparent: the first being the possibility for cluster repeats, and the second being time of analysis. The potential for repeating Fe-Ti oxide cluster measurements is a very real possibility since each individual cluster within the sample would have to be done one at a time with no effective method of keeping track of which clusters have been completed. The areas for each cluster would then be added together for the total percent Fe-Ti oxide of the sample. The second issue of time is more of a compound problem. The Wand method requires that each Fe-Ti oxide cluster to be selected and measured independently. In many of the thin section samples the Fe-Ti oxides are scattered in hundreds to thousands of isolated clusters. Not only would this cause an appreciable increase in thin section sample analysis completion time (which translates to taking an inordinate amount of time to complete a sample), but there is also the possibility of user strain, leading to mistakes. The added time of the Wand method does not result in better quality data; the Threshold method provides the best quality data without sacrificing efficiency.

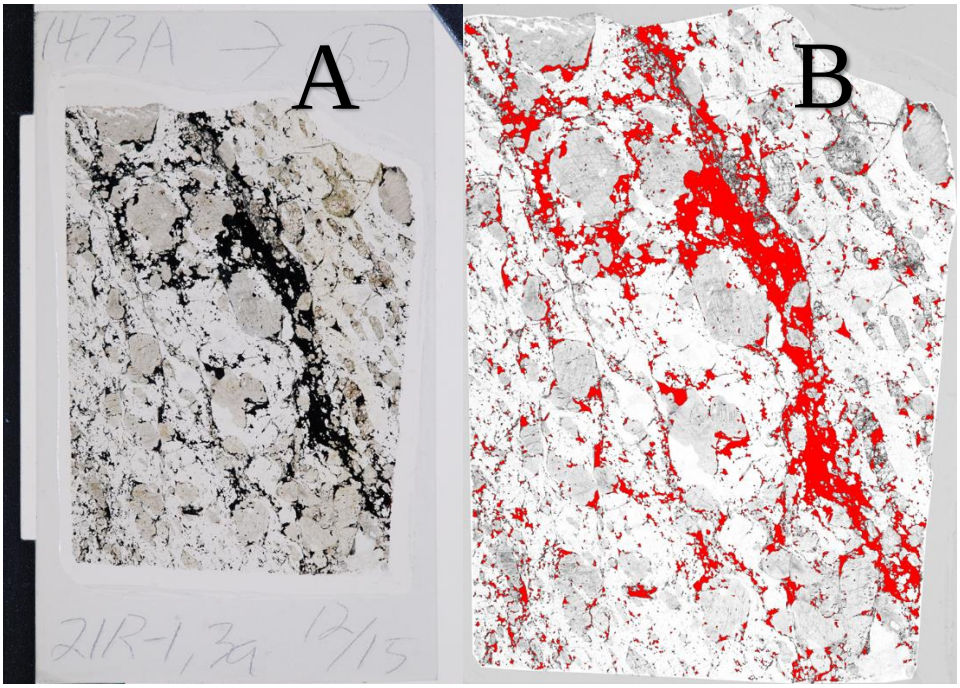

Figure 4.11 Wand Method Comparison

A) The left image is of thin section 360-U1473A-21R-1-TS-65. B) The right image is of the sample image in *Fiji* after the Threshold method had been completed. Unlike Figure 4.10 there is an obvious lack of Fe-Ti oxide cluster continuity which would require each Fe-Ti oxide cluster to be selected and measured individually. However, image B has had the Threshold method applied in *Fiji* which allows for a more efficient measure of the thin sections Fe-Ti oxide concentration.

4.1.3.3 Method Summary

Based on the findings from the two alternate methods tested here, the Threshold method provides the best balance of quality and efficiency. The two alternate methods either introduced avoidable error or took far too much time when compared to another fast, but similarly accurate, and precise method. The Threshold method outlined in detail above has a low error risk, high repeatability, and was the most efficient, while maintaining accuracy. It was for these reasons that the Threshold method was selected over the alternative methods. The Threshold method was preformed multiple times on a test sample (i.e. thin section sample 360-U1473A-3R-1-TS-3) to illustrate the method's repeatability and reasonable level of precision; Table 4.2 includes results from the same

thin section sample for multiple iterations. As can be seen from the results shown in Table 4.2, the ultimate calculated percent Fe-Ti oxides were within a reasonably small margin of one another with the largest difference being 0.013%.

Table 4.2 Repeatability of results using the Threshold method within *Fiji*.

Trials run on thin section sample 360-U1473A-3R-1-TS-3						
Trial Run	Brightness/contrast values		Threahold values		Measured area (pixels)	
	Brightness	Contrast	low	high	total area	output
1	0	155	0	12	10362133	576133
2	0	150	0	12	10392169	575986
3	0	80	0	24	10382765	576259

4.1.4 *R* Methods

The final portion of this study includes statistical analyses to find the relevance of various factors in contributing to the samples' degree of deformation. In order to find the relevance, the final datasheets were run through the *R* statistical analysis to find what factor has the most control on the samples degree of deformation, such as the Fe-Ti oxide concentration, depth, percent olivine, and grain size (R Core Team, 2015). The test used was a multiple regression model since this provided an understanding of how the various variables corresponded with one another and which variables had the most control over the crystal-plastic deformation within the sample dataset. When the data sets for each hole were analyzed through the *R* software, the values for grain size had to be changed to a numeric value type from text for the software to run the tests. There were four different grain sizes used in this study so for the statistics data set they were assigned a value of 1-4: fine grained was 1, medium grained was 2, coarse grained was 3, and pegmatitic was 4. The code this study used within the open sourced statistical software package *R* can be found in Appendix A.

CHAPTER V – Results

5.1 General Results

Several datasets were used in this study including: top depth of each thin section in meters below seafloor (mbsf), percent Fe-Ti oxide, percent olivine, crystal-plastic fabric (CPF) intensity ranking, and grain size (fine grained being less than 1 mm, medium grained as 1-5 mm, coarse grained being 5-10 mm and very coarse grained being over 10 mm). These datasets were collected for each hole and came from various sources; the data were both collected and obtained from previous expedition records. This study calculated the percent Fe-Ti oxide in 589 thin sections from IODP Hole U1473A and ODP Holes 1105A and 735B using the *Fiji* image analysis software, using methods outlined in the previous chapter. The concentration of the mineral phase olivine is reported as estimated modal percentages and was either estimated based on thin section images or taken from previous studies/expedition publicly accessible records (IODP: http://iodp.org; ODP: http://www-odp.tamu.edu/publications/index.html). The top depth is the measured depth below the sea floor at the 'top' of a given thin section and was also obtained from the public records of previous studies, as every sample collected from ODP and IODP Legs/Expeditions are cataloged with Leg/Expedition, hole, core, section, interval, and depth. The CPF intensity rank is a value assigned to a given thin section by the expeditionary team as a quick reference for crystal-plastic deformation intensity and these data were either estimated based on the thin section or were taken from ODP and IODP Expedition reports. The CPF intensity ranking ranges from 0-5 with 0 being no crystal-plastic deformation, and 5 represents an ultramylonite. This ranking system was developed during Leg 176 for ODP Hole 735B (Shipboard Scientific Party, 1999). All

the variables explained above were utilized in both graphical and statistical portions of this study. The last variable, grain size, was also either estimated based on thin section images or collected from the publicly accessible records based on average grain, and was utilized in only the statistical portion of this study. Table 5.1 is a summary of how the various datasets were used to create the data pools for the three holes used in this study and specifically which ones this study is adding to the data pool (Shipboard Scientific Party, 1991; Shipboard Scientific Party, 1999; Dick et al, 2016).

Table 5.1 Dataset Responsibilities

Disclosure of datasets calculated by this study and those acquired from another source. Also disclosed are the number of samples for each hole and how many from each collection should there be multiple. (Ship = came from previous study records, This Study = data found or compiled from non-public datasets by this study)

Hole	Sample Collection	# of thin sections	Depth	% Fe-Ti Oxides	% Olivine	CPF Intensity Rank	Grain Size
IODP U1473A	Shipboard	304	Ship	This Study	Ship	Ship	Ship
ODP 1105A	Miller	11	Ship	This Study	This Study	This Study	This Study
ODP 1105A	Shipboard	70	Ship	This Study	This Study	This Study	This Study
ODP 735B	Yoshinobu	69	Ship	This Study	This Study	This Study	This Study
ODP 735B	Miller	83	Ship	This Study	This Study	This Study	This Study
ODP 735B	Leg 118	52	Ship	This Study	Ship	This Study	This Study

There was a total of 589 thin sections used to calculate the percent Fe-Ti oxides within the three holes used for this study. There was a total of 304 thin sections used for IODP Hole U1473A, all of which came from the thin sections made during Expedition 360. There was a total of 80 thin sections used for ODP Hole 1105A, which were a

combination of 70 thin sections from Expedition Leg 179 and 11 thin sections from Dr. D. Jay Miller's personal collection (Dr. D. Jay Miller is the Manager of Technical and Analytical Services for the IODP at Texas A&M University). The last 218 thin sections came from a combination of sources including shipboard thin sections from Leg 118, and thin sections from Leg 176 of Dr. Aaron Yoshinobu's and Dr. D. Jay Miller's personal collections, 69 and 83 respectively (Dr. Aaron Yoshinobu is a Professor in the Department of Geosciences at Texas Tech University). All of the thin section datasets from both this study's findings and the expedition reports were used to ascertain what relationships between Fe-Ti oxide concentrations and CPF intensity may be present within Atlantis Bank. The major relationship this study was attempting to find is the potential relationship between the concentration of Fe-Ti oxides and the CPF intensity within Atlantis Bank. The unaltered raw data collected during this study and other datasets amassed through this study of IODP Hole U1473A, ODP Hole 1105A, and ODP Hole 735B are located within Appendix B.

The last portion of this study was done using the statistical software package *R* to analyze the data sets from each hole through a multiple regression test to find which factors, if any had the most control over the CPF intensity ranking values of the thin section samples (John Fox and Sanford Weisberg, 2011; R Core Team, 2015). The results of this test are shown in a correlation plot that allows the reader to see how the various variables correlate with each other. The correlations between the variables are based on a scale ranging from 1 to -1, this allows the user to see if the variables have a coincident or a reverse relationship. A positive correlation value means that the variables are good predictors of each other with a value of 1 being a coincident relationship, a negative

correlation value is exactly the opposite with a value of -1 being a reverse relationship. Thus, zero is the middle ground which signifies there is no influence between the variables. The last portion of statistical analysis on the data gathered for each hole was to run a subpopulation of each hole's dataset through the same multiple regression model as before to see if there was any change to the relationships found. The subpopulation created for this testing was made by isolating every thin section sample that had a calculated Fe-Ti oxide concentration of 5% or more.

5.1.2 IODP Hole U1473A

This section was completed using the 304 of the thin sections from the recovered core of IODP Hole U1473A gathered by the expeditionary team.

5.1.2.1 Fe-Ti oxides

Figure 5.1 is a plot of the Fe-Ti oxide concentration variations calculated by this study versus the top depth, of the respective thin section sample. In terms of variations with depth the majority of the hole is fairly constant throughout with spikes in Fe-Ti oxide concentrations focused in three locations: the top, middle, and base of the hole. The range of Fe-Ti oxide concentration calculated within IODP Hole U1473A is 0–22.1%. Generally, the Fe-Ti oxide concentrations are less than ~1.3%, which accounts for 66.5% of the thin sections. However, there are 11 thin section samples with Fe-Ti oxide concentrations over 5%, which accounts for 3.6% of the thin sections within IODP Hole U1473A. The other 29.9% of the thin section samples had Fe-Ti oxide concentrations in the range of ~1.3–5%. The maximum of 22.1% was in sample 360-U1473A-83R-1-W 10/14-TSB; this thin section can be seen in Figure 5.2A. The average Fe-Ti oxide concentration in this hole is ~1.14%. There are some general divisions that can be made

based on the average of Fe-Ti oxides present within intervals that can be defined by depth. In IODP Hole U1473A there is the general trend of the higher concentrations being at the top and the base of the Hole, with an interval of lower concentrations in the middle. The two intervals with a generally higher average of Fe-Ti oxide concentration are located at 10.7–99.8mbsf and 668.77–756.42mbsf. The interval with a lower average of Fe-Ti oxide concentration is located at 103.76–668.52mbsf. The two high concentration sections account for the upper and lower clusters of Fe-Ti oxide spikes over 5%, the middle section contains the majority of the low concentrations with a few spikes to over 5%.

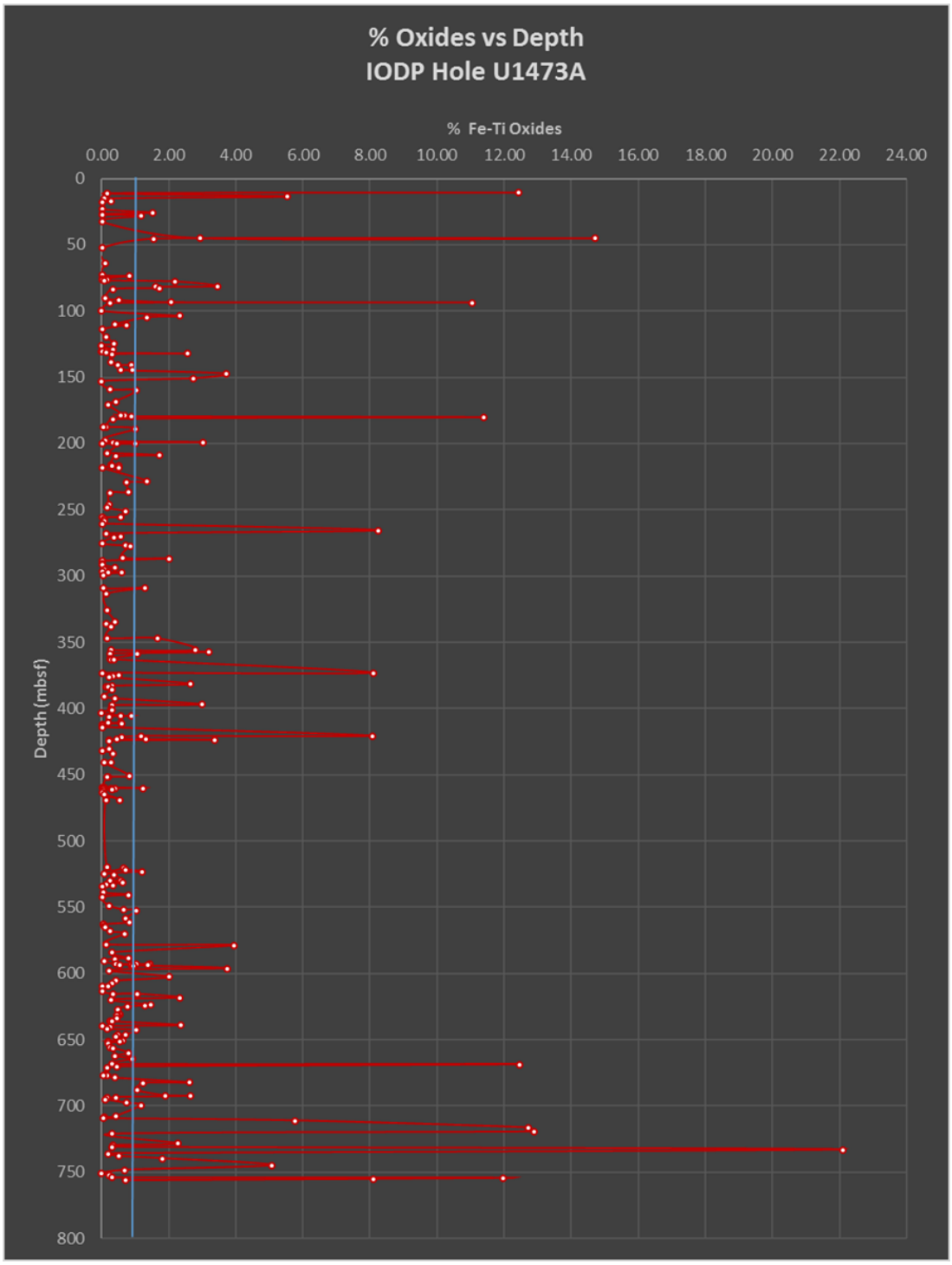

Figure 5.1 Fe-Ti oxides by Depth, IODP Hole U1473A

All calculated Fe-Ti oxide concentrations using the *Fiji* analysis software. It has been plotted based on the thin sections' top depth to represent the down hole concentration variations of Fe-Ti oxides within IODP Hole U1473A. The blue line represents the average Fe-Ti oxide value of 1.14%.

5.1.2.2 CPF

Figure 5.3 is the graphic representation of the CPF intensity within IODP Hole U1473A and was plotted based on depth. Some thin sections, however, did not have a reported CPF intensity ranking; so, to allow for the best graphical representation, those thin sections were omitted from the plot. There was a total of forty-two thin sections out of the 304 that did not have a CPF intensity ranking reported; however, this study calculated Fe-Ti oxide concentrations for all 304 thin sections. Any thin section with an Fe-Ti oxide concentration of 5% or higher also has a corresponding CPF intensity ranking of 2 or higher. There were eleven thin sections that had over 5% Fe-Ti oxides; nine of these thin sections (82%) show this relationship between CPF intensity and FE-Ti oxide concentration. The two thin sections with a Fe-Ti oxide concentration higher than 5% that do not show this relationship are located near the base of the hole (e.g., Figure 5.2C). Wherever there is a CPF intensity rank higher than 0, Fe-Ti oxides are present. The concentration of Fe-Ti oxides, however, is not always significant with some thin section concentrations being as low as 0.01%. This means that within IODP Hole U1473A Fe-Ti oxides are present wherever crystal-plastic deformation occurred. There is however, the reverse of this relationship present given how there is not always crystal-plastic deformation wherever there are Fe-Ti oxides present. There are thirty-two out of the 304 thin sections with Fe-Ti oxide concentrations that range from 0.01–5.76%, but have no crystal-plastic deformation present. This subpopulation of thin sections with some Fe-Ti oxide concentration and no crystal-plastic deformation accounts for 10.52% of the samples from IODP Hole U1473A.

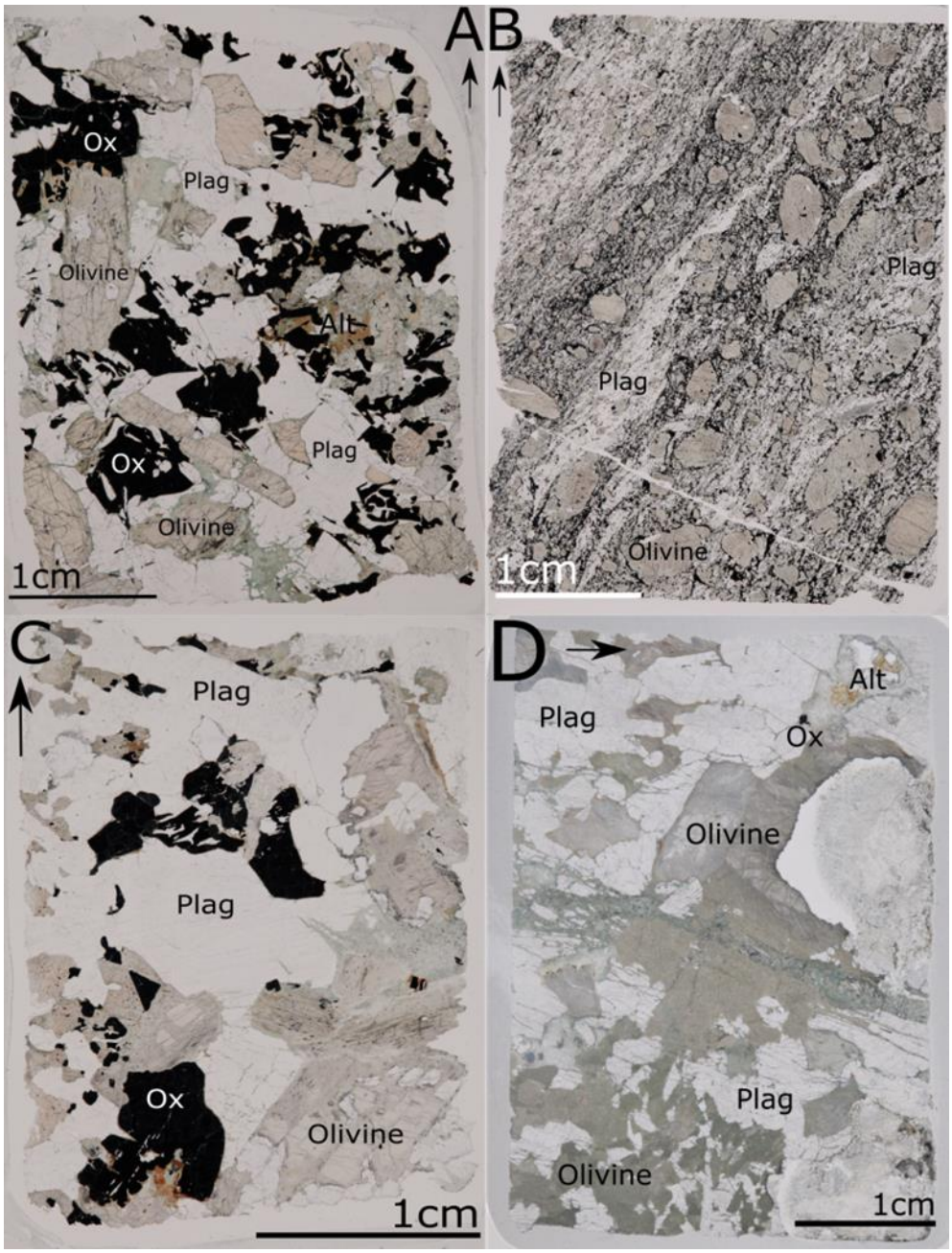

Figure 5.2 Thin Section Compilation from IODP Hole U1473A

Four thin section samples from IODP Hole U1473A representing several aspects within the hole. The black arrows indicate up core direction. A) Thin section 360-U1473A-83R-1-TS-297 at 733.03mbsf has highest Fe-Ti oxide concentration of all the samples for IODP Hole U1473A at 22.10%. B) Thin section 360-U1473A-75R-4-TS-263 at 668.77mbsf has over 5% Fe-Ti oxide concentration of 12.47% and a high CPF value of 4. C) Thin section 360-U1473A-80R-7-TS-285 at 716.51mbsf has an Fe-Ti oxide concentration over 5% of 12.72% but still a low CPF value of 1. D) Thin section 360-U1473A-3R-4-TS-6 at 17.67mbsf has a low Fe-Ti oxide concentration of 0.03% and a CPF value of 0.

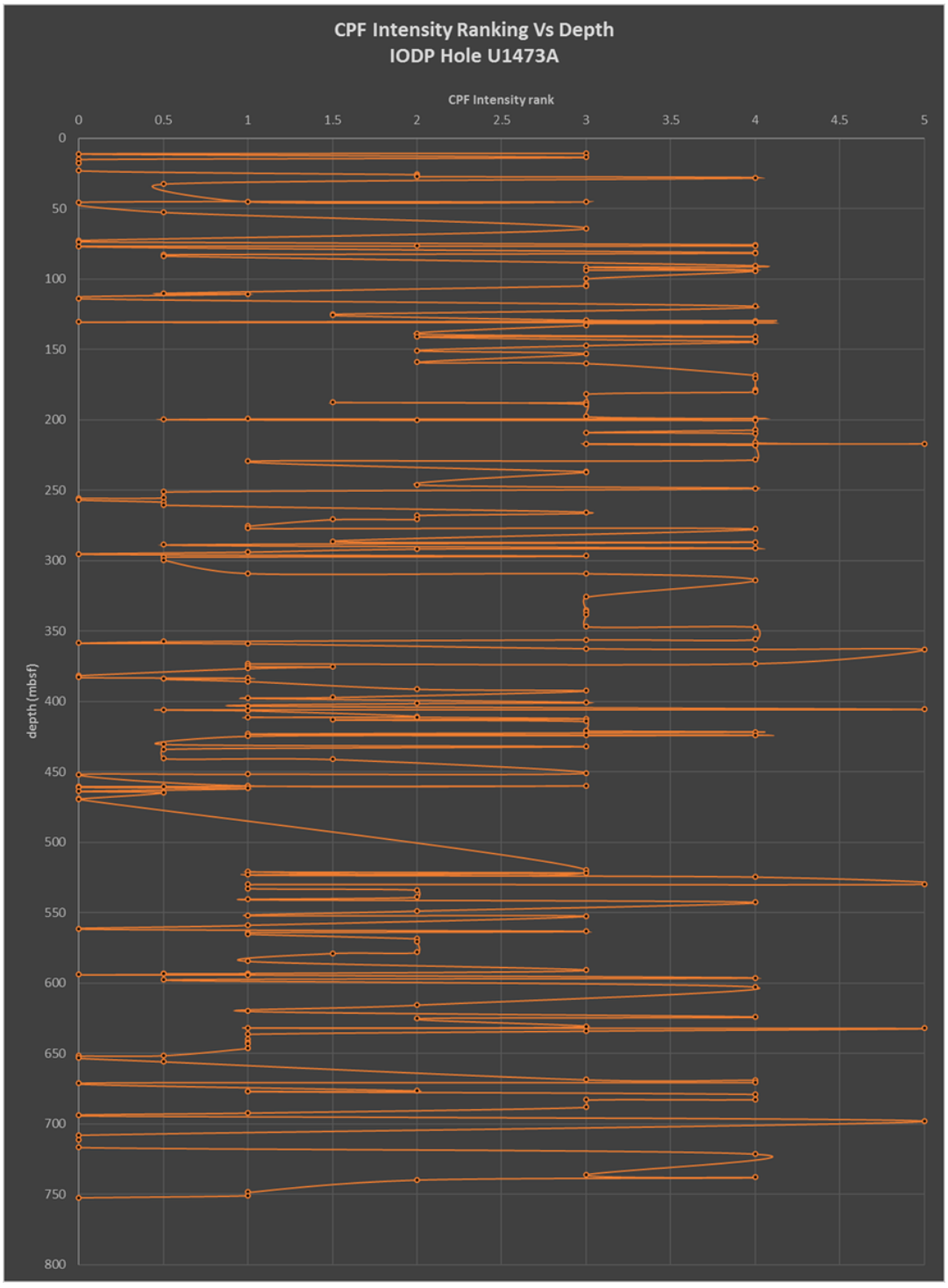

Figure 5.3 CPF versus Depth, IODP Hole U1473A

Thin sections from IODP Hole U1473A with a CPF intensity rank assigned to it. This plot was created to illustrate the relationship down hole using the thin sections top depth. As can be seen from this plot there is a high level of variability to the CPF intensity within IODP Hole U1473A.

5.1.2.3 Olivine

Using the data from the IODP Hole U1473A ship reports, the variations of the mineral phase olivine were plotted by depth below the sea floor in Figure 5.4. The olivine content within IODP Hole U1473A was consistent, with the only section showing very high values being in the middle to base of the section, from ~270–618mbsf. Based on the data gathered for the olivine content, the minimum value was reported as 0%, the maximum value reported was 32%, and the average reported value for olivine was ~6.6%. The relationship between Fe-Ti oxide and olivine percent by depth, Figure 5.5, indicates that when there is a higher percentage of olivine, the Fe-Ti oxide concentration is either reduced or absent all together and vice versa.

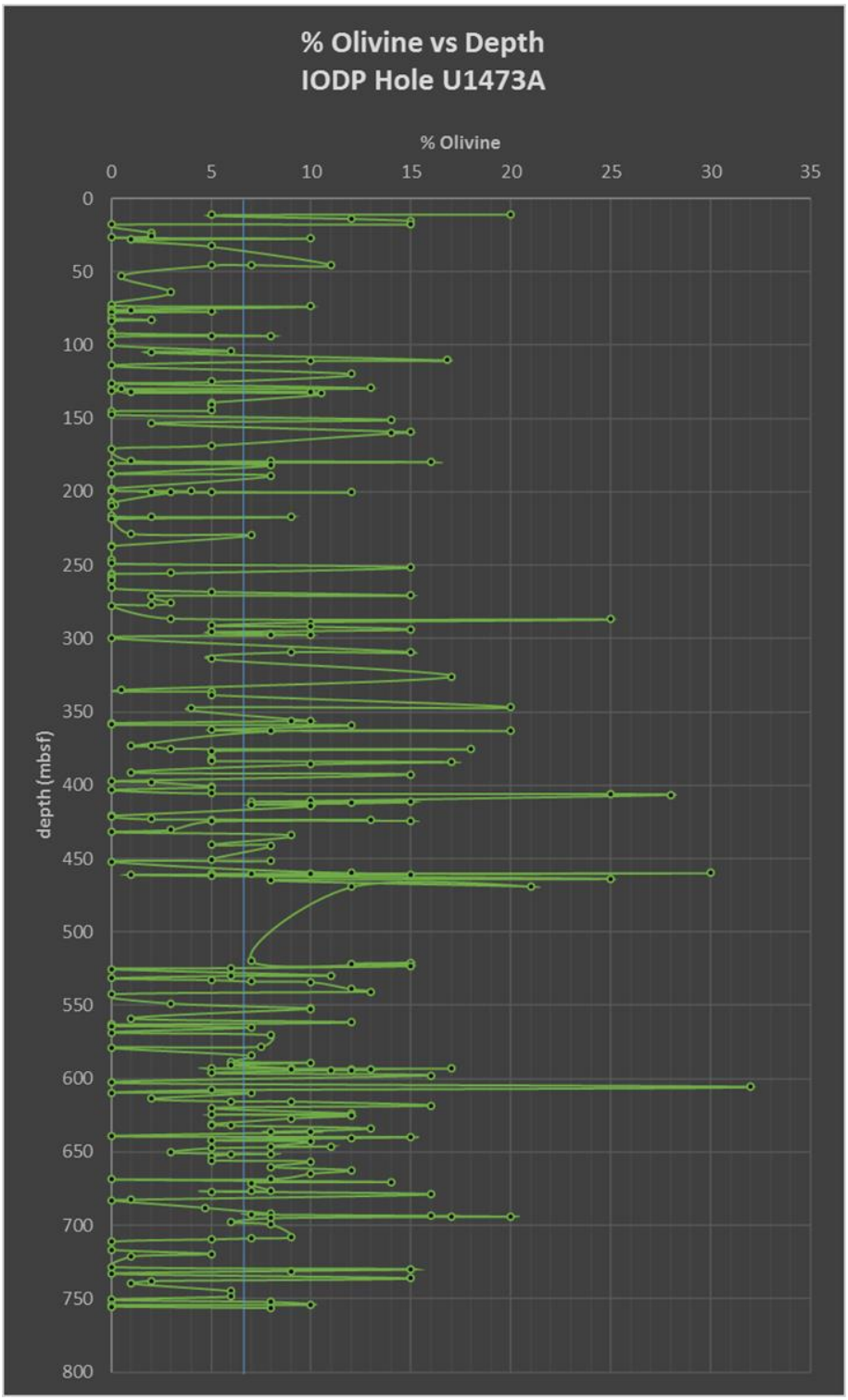

Figure 5.4 Olivine by Depth, IODP Hole U1473A

Variability of the percent of olivine concentrations throughout IODP Hole U1473A with depth. The blue line is the average percent of olivine within IODP Hole U1473A of 6.6%.

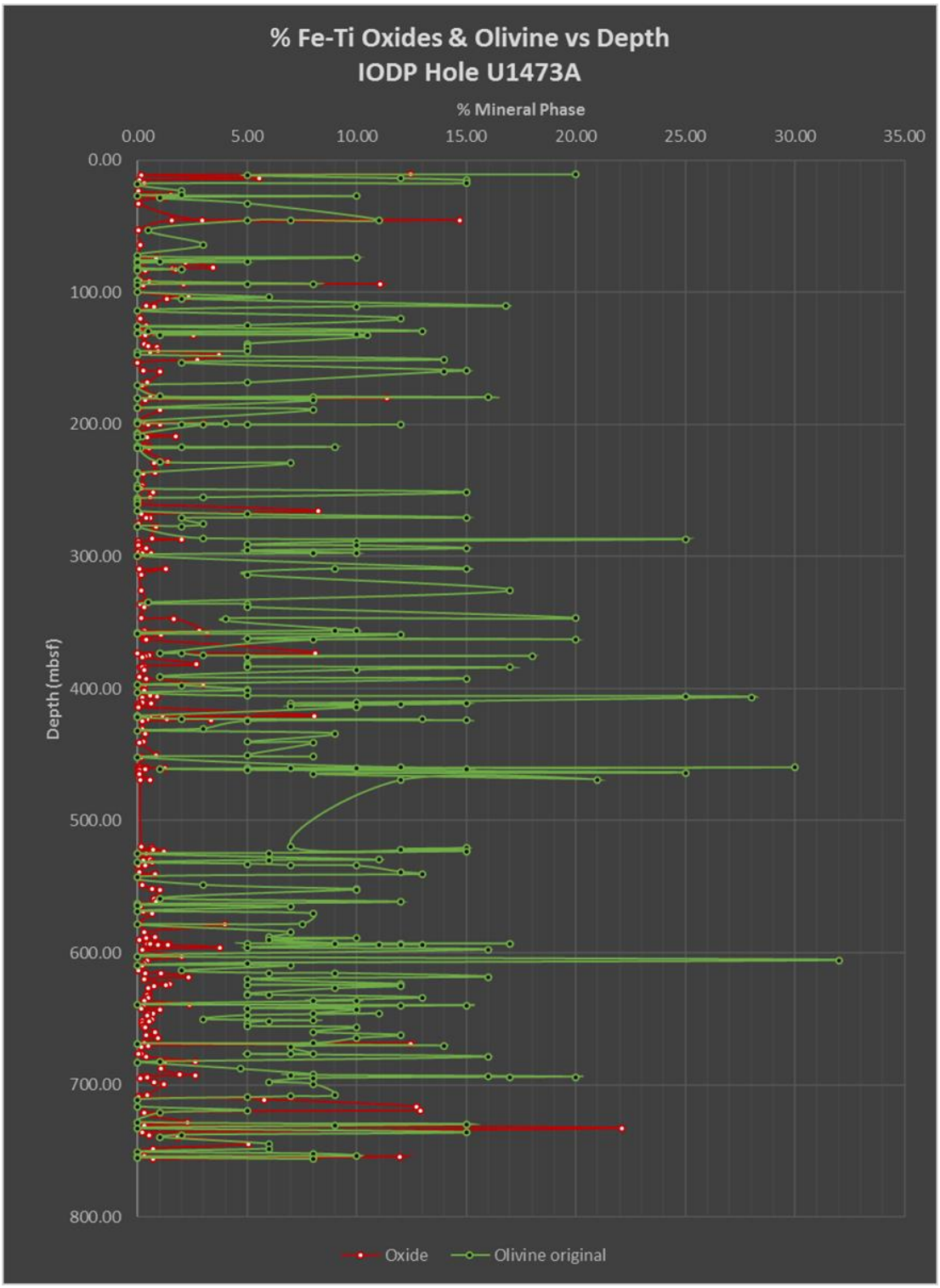

Figure 5.5 Fe-Ti Oxides and Olivine by Depth, IODP Hole U1473A

General relationship between the mineral phases of olivine and Fe-Ti oxides present within IODP Hole U1473A. In this case, high presence of olivine correlates to lower/absent Fe-Ti oxide presence.

5.1.2.4 *R*

The open source statistical software package *R* was used to develop and execute the multiple regression models used to constrain factors (e.g., Fe-Ti oxide concentration) that might correlate with the presence of CPF and their intensity within IODP Hole U1473A (John Fox and Sanford Weisberg, 2011; *R* Core Team, 2015). The results of these multiple regression models are depicted in Figure 5.6. There is a correlation between the CPF intensity ranking and the concentration of Fe-Ti oxides based on what can be seen within the holes dataset. The *R* software calculated this correlation between the Fe-Ti oxide content and CPF intensity to be a 0.12, indicating that the concentration of Fe-Ti oxides is a good predictor of the CPF intensity rank within IODP Hole U1473A. An interesting correlation that was found in the test was that grainsize had a -0.29 correlation value with CPF intensity, meaning that it was a reverse predictor of CPF intensity within IODP Hole U1473A. Olivine concentration (-0.17) and depth (-0.15) were also reverse predictors of the CPF intensity within IODP Hole U1473A. Fe-Ti oxide concentration is the only variable used in this study to positively correlate with the CPF intensity ranking. To illustrate this correlation the Fe-Ti oxide concentration values and the CPF intensity ranking values were plotted together in Figure 5.7. The trend line, with a slope of 0.1168 and an R^2 value of 0.0285, depicts this relationship. While this may not be a strong positive trend line, it does show that with an increase in CPF intensity values there is a corresponding increase in Fe-Ti oxide concentration values.

The subpopulation multiple regression model results for IODP Hole U1473A are depicted in Figure 5.8; the results of this model found some minor changes. The subpopulation used in this round of statistics was a subgrouping of all thin sections that

had a Fe-Ti oxide concentration of 5% or more. All variables stayed the same with regards to positive and negative predictors; the only changes were the actual correlation values fluctuating with the largest change being grain size from -0.29 to -0.82. While the correlation between the Fe-Ti oxide concentration and the CPF intensity ranking remained positive, there was a drop in the correlation value of the subpopulation from a 0.12 to a 0.01.

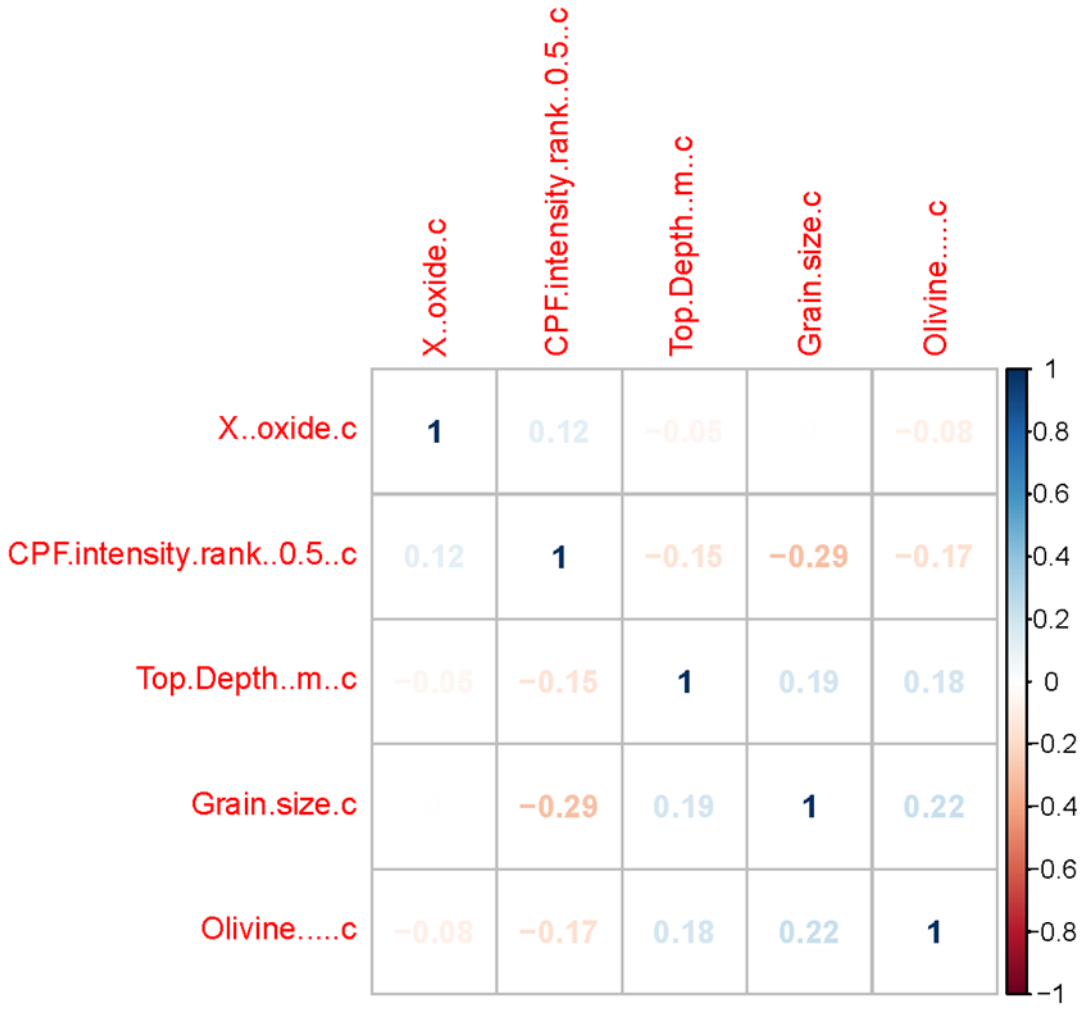

Figure 5.6 Correlation Plot for the *R* results of IODP Hole U1473A

The output of the multiple regression done in the statistical software package *R*; using the data gathered for IODP Hole U1473A.

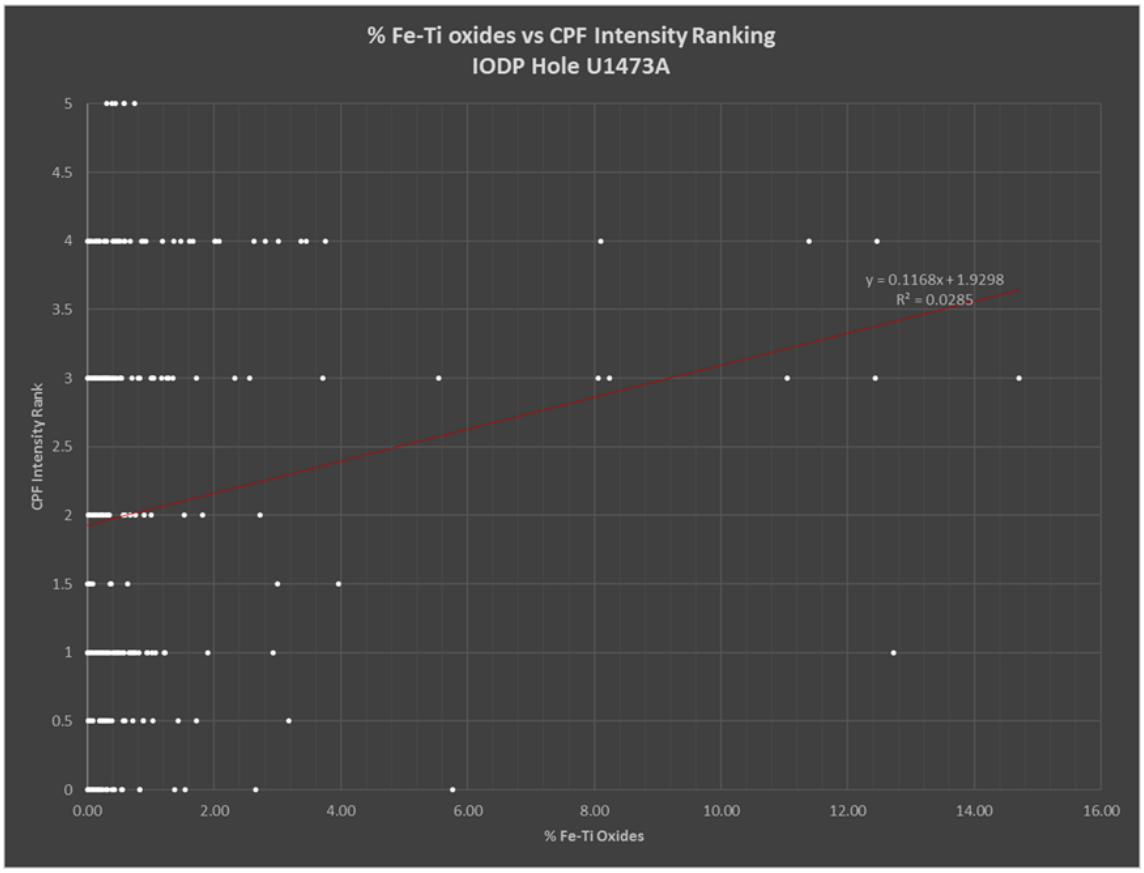

Figure 5.7 Fe-Ti Oxides by CPF IODP Hole U1473A

The correlation between Fe-Ti oxide concentration and CPF intensity within IODP Hole U1473A. The general trend between them is shown using the red trend line which is indicating that with increasing Fe-Ti oxide concentration within a thin section sample there is a corresponding increase in CPF intensity of the thin section sample.

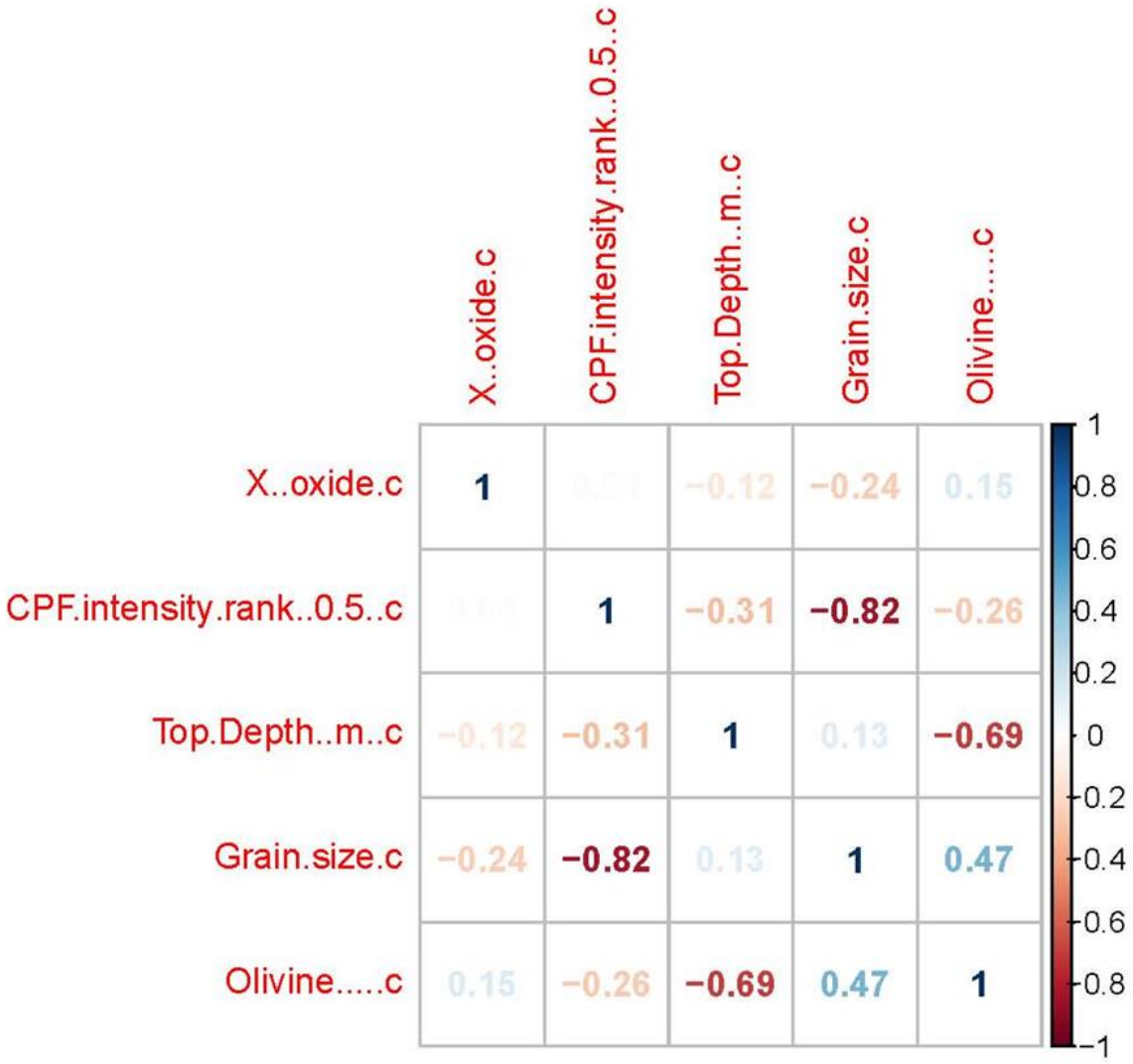

Figure 5.8 *R* results correlation plot for the subpopulation of IODP Hole U1473A

The correlation values between the five variables used in this study for the subpopulation of thin sections with Fe-Ti oxide concentrations over 5% within IODP Hole U1473A. The correlation value for FE-Ti oxides and CPF intensity is 0.01.

5.1.3 ODP Hole 1105A

Eighty thin sections from ODP Hole 1105A were examined and include the shipboard thin sections (Shipboard Scientific Party, 1999; MacLeod et al, 2017) and Dr. Jay Millers' personal samples.

5.1.3.1 Fe-Ti Oxides

The variation within the Fe-Ti oxide concentration, plotted in Figure 5.9, is low at the top of the hole then increasing and remains relatively constant throughout the rest of the Hole. Generally, the Fe-Ti oxide concentrations are less than ~3%, which accounts for 66.25% of the thin sections. However, there are 20 spikes of Fe-Ti oxide concentrations over 5%, which accounts for 25% of the thin sections; the other 8.75% of the thin sections fall in between ~3 and 5% Fe-Ti oxide concentrations. The range of Fe-Ti oxide concentration calculated within ODP Hole 1105A is from 0.007-15.5%, with the average Fe-Ti oxide concentration of this hole being ~2.97% and a maximum of 15.5% in sample 179-1105A-7R-3-W 33/36-TSB-TSS (Figure 5.10A).

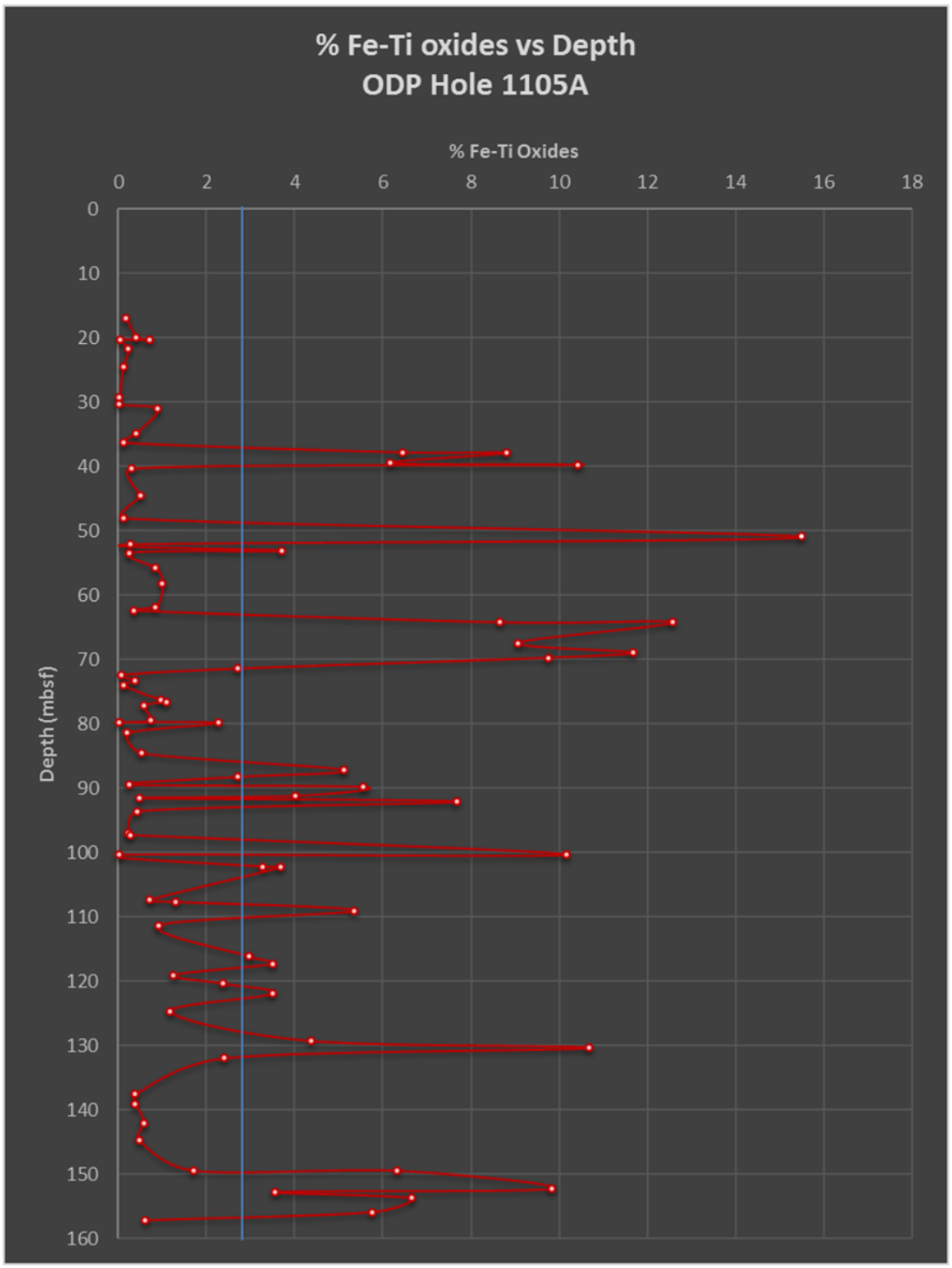

Figure 5.9 Fe-Ti oxides by Depth, ODP Hole 1105A

The calculated Fe-Ti oxide concentrations found using the Fiji analysis software and have been plotted by the thin sections top depth to represent the down hole concentration variations of Fe-Ti oxides within ODP Hole 1105A. The blue line denotes the average Fe-Ti oxide concentration within this Hole of 2.97%.

5.1.3.2 CPF

Figure 5.11 plots the variated CPF intensity within ODP Hole 1105A and was plotted based on depth; there is a general trend of CPF intensity increasing with depth. Aside from 6 of the 80 thin sections in this study, any thin section with an Fe-Ti oxide concentration of 5% or higher also has a CPF intensity ranking of 2 or higher, Figure 5.10B illustrates this relationship. There are 20 thin sections that have over 5% Fe-Ti oxides; 14 of these thin sections, 70%, show this relationship of elevated CPF intensity. The 6 thin sections with a Fe-Ti oxide concentration higher than 5% that do not show this relationship are located within the first 70 meters of the hole, and can be confined even further into a ~32 meter interval (37.79–69.69mbsf); an example of this is in Figure 5.10C. The other observations come from simply comparing the presence of Fe-Ti oxides and the presence of crystal-plastic deformation within the thin sections. The second observation is the fact that wherever there is a CPF intensity rank higher than 0, there is always Fe-Ti oxides present; this concentration however, is not always a significant amount with some Fe-Ti oxide concentrations being as low as 0.007%. This means that within ODP Hole 1105A Fe-Ti oxides are present wherever crystal-plastic deformation has occurred. There is, however, a reverse of this relationship is present as well, since there is not always crystal-plastic deformation wherever there are Fe-Ti oxides present. There are eleven of the eighty thin sections with Fe-Ti oxide concentrations ranging from ~0.5-2% that have no crystal-plastic deformation present, which accounts for 13.75% of the thin sections, Figure 5.10D is an example of this.

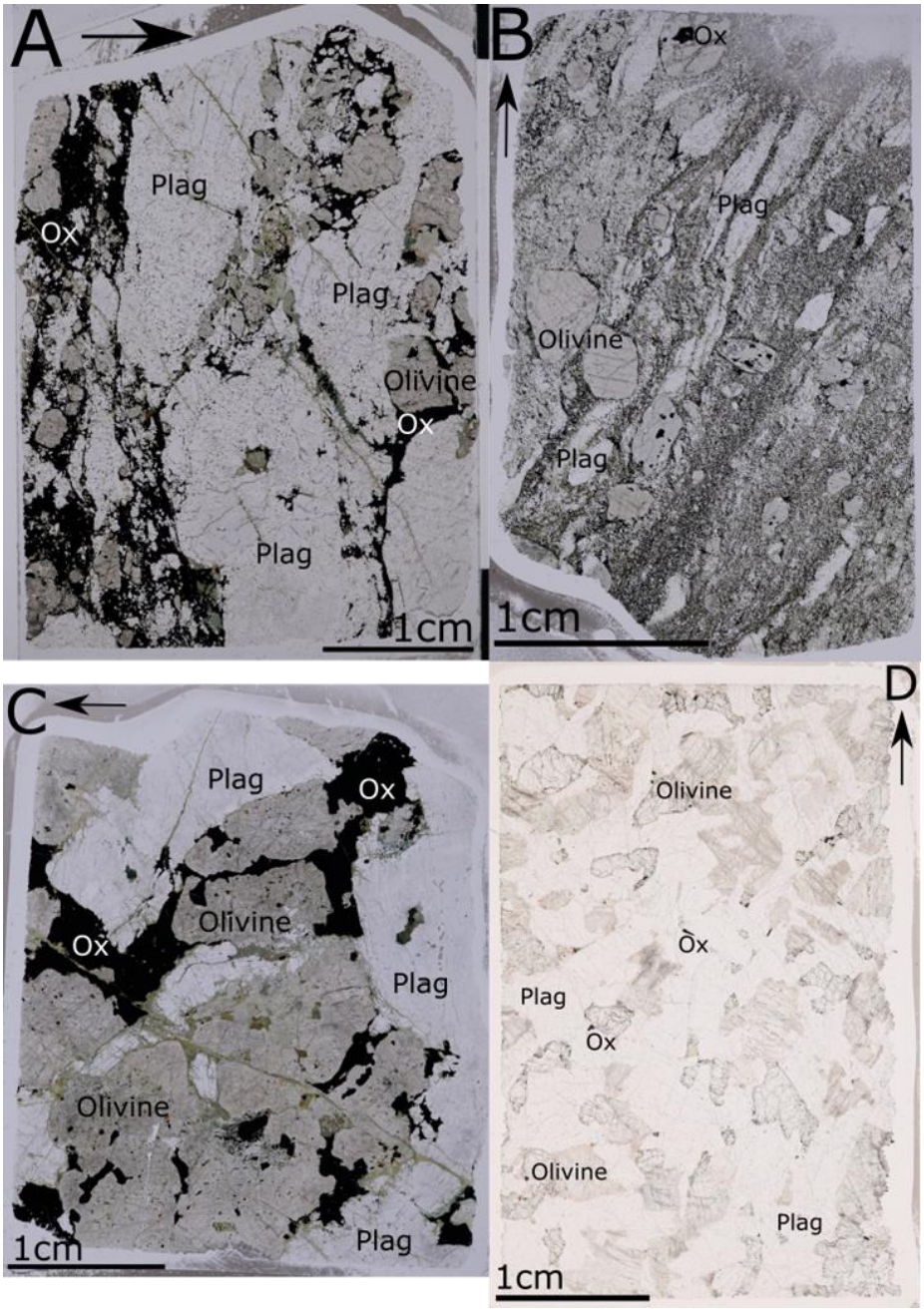

Figure 5.10 Thin section compilation from ODP Hole 1105A

Four thin section samples from ODP Hole 1105A representing several aspects within the hole, the black arrows indicate up core direction. A) Thin section 179-1105A-7R-3-TSS at 50.96mbsf has the highest Fe-Ti oxide concentration of all the samples for ODP Hole 1105A at 15.512%. B) Thin section 179-1105A-5R-1-TSS at 39.74mbsf has over 5% Fe-Ti oxide concentration of 10.433% and a high CPF value of 4. C) Thin section 179-1105A-10R-2-TSS at 64.2mbsf has a Fe-Ti oxide concentration over 5% of 12.568% but still a low CPF value of 1. D) Thin section 179-1105A-4R-3-TSS at 36.28mbsf has a low Fe-Ti oxide concentration of 0.12% and a CPF value of 0.

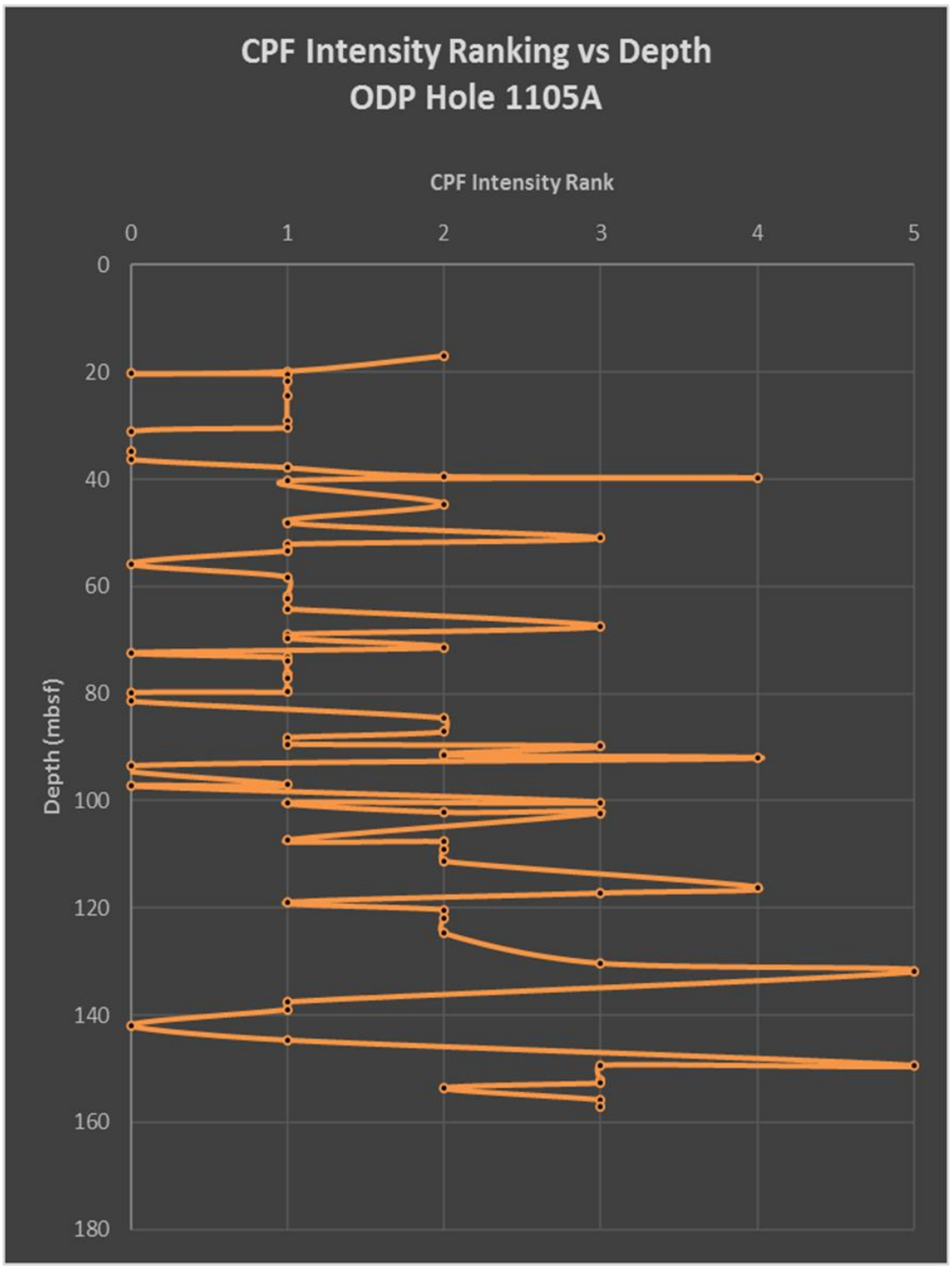

Figure 5.11 CPF by Depth, ODP Hole 1105A

This plot of the down hole fluctuations of the CPF intensity rank using the thin sections top depth. As can be seen from this plot there is a possible trend with the CPF intensity getting higher down hole, with a few exceptions, within ODP Hole 1105A. However, this hole is only ~160m deep, so it does not represent as much as the other Holes.

5.1.3.3 Olivine

The olivine content within ODP Hole 1105A varies with depth, as seen in Figure 5.12, but generally the olivine starts low peaks in the middle (107.35 mbsf) and tapers off towards the base of the Hole. Based on the data gathered for the olivine content the minimum value was reported as 0%, the maximum value reported was 26% at the 107.35 mbsf peak, and the average reported value for olivine was ~6.89%. The relationship between Fe-Ti oxide and olivine percent versus depth, illustrated in Figure 5.13, indicates that when there is a higher percentage of olivine, the Fe-Ti oxide concentration is either reduced or absent all together. Conversely, in sections where there is a moderate to high Fe-Ti oxide concentration there is little to no olivine present within those thin sections.

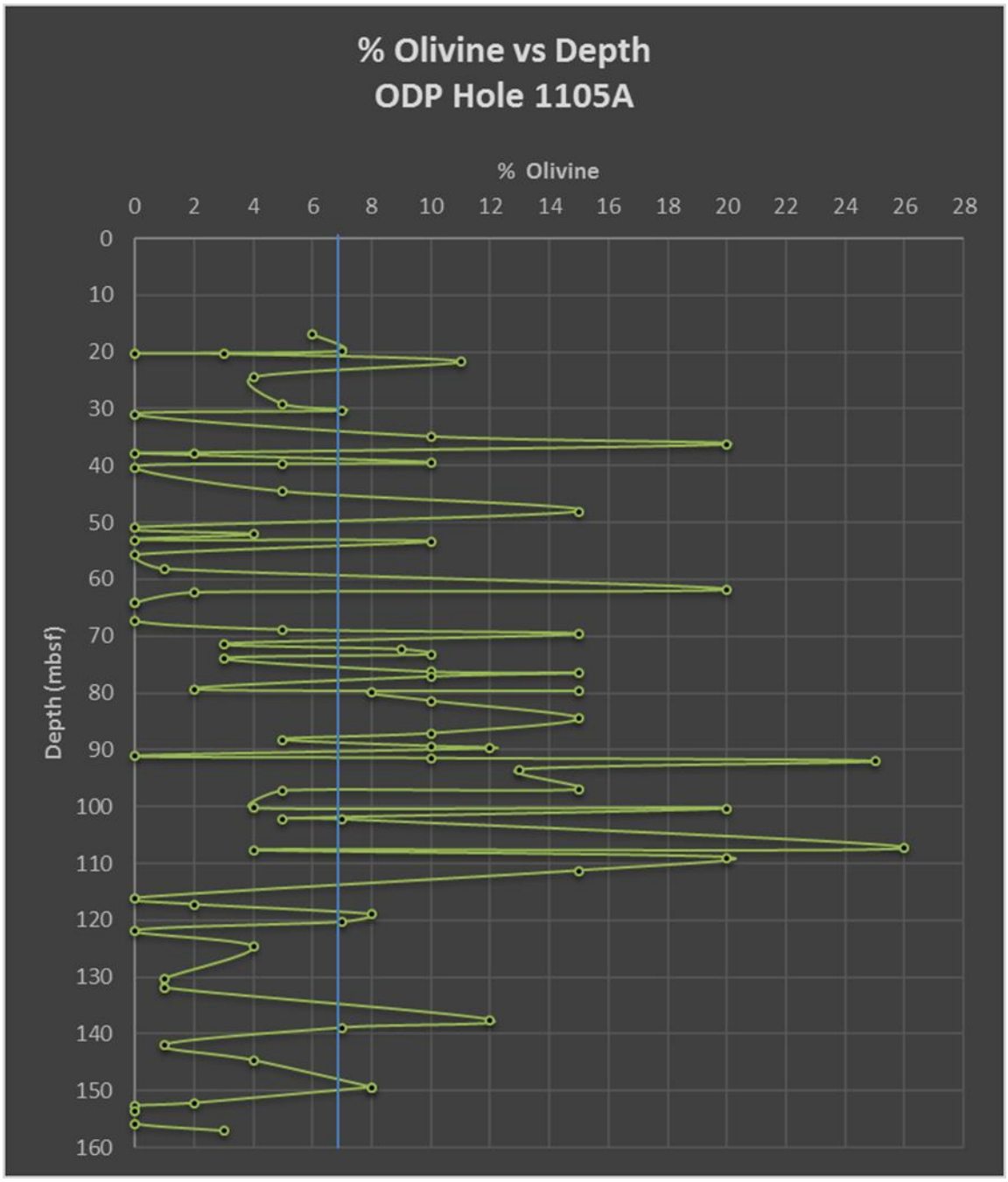

Figure 5.12 Olivine by Depth, ODP Hole 1105A

Variability of the percent of olivine within the thin section samples throughout ODP Hole 1105A with depth. The blue line is the average concentration of olivine within ODP Hole 1105A of 6.88%.

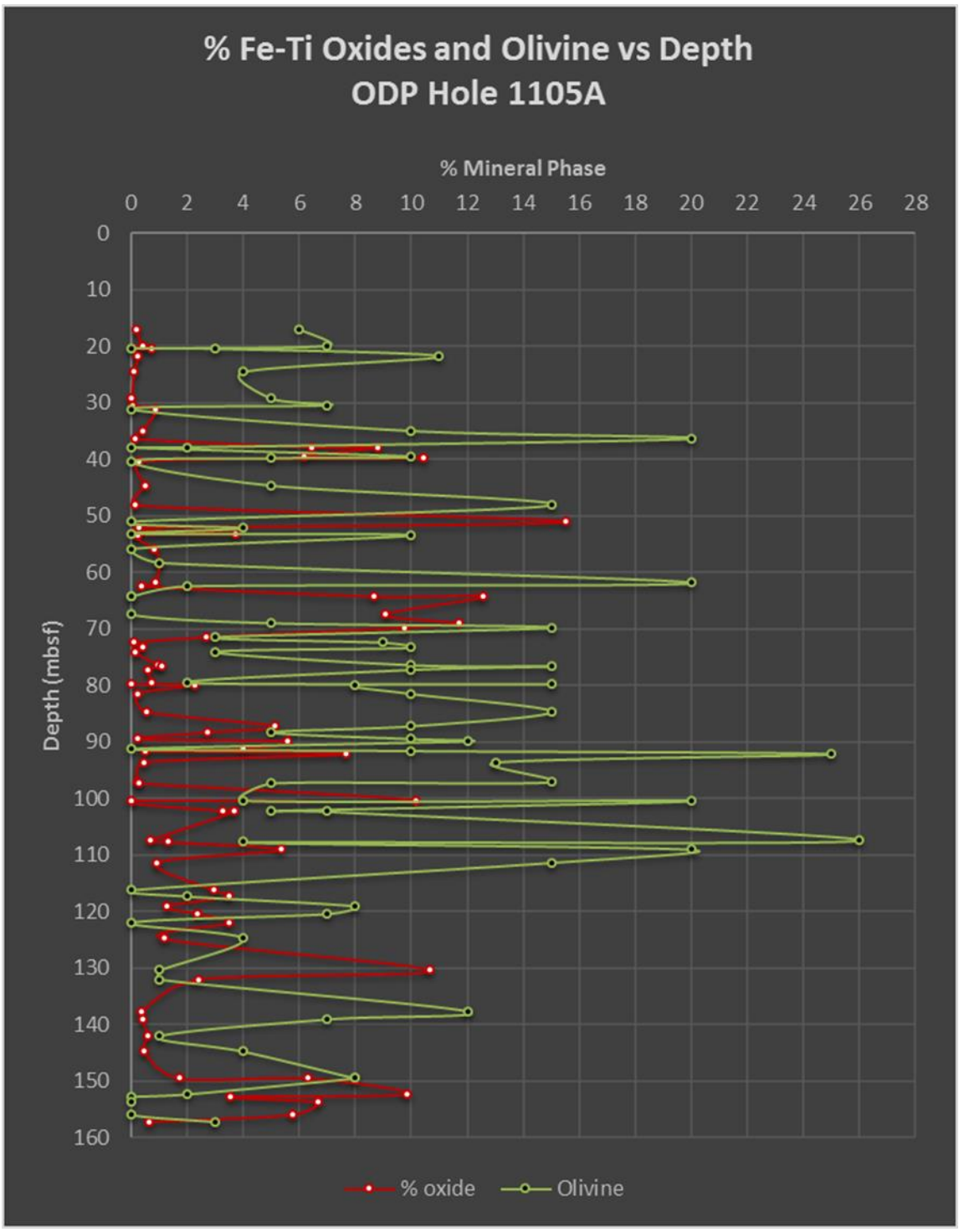

Figure 5.13 Fe-Ti oxides and Olivine by Depth, ODP Hole 1105A

General relationship between the mineral phases of olivine and oxides present within IODP Hole 1105A. High presence of olivine correlates to lower/absent oxide presence.

5.1.3.4 *R*

The open source statistical software package *R* was used to perform multiple regression models to constrain which factors (e.g., Fe-Ti oxide concentration) may correlate with the presence of CPF and their intensity within ODP Hole 1105A (John Fox and Sanford Weisberg, 2011; *R* Core Team, 2015). The results of the multiple regression model run on the data in *R* is presented in Figure 5.14. The *R* software calculated the correlation between Fe-Ti oxide content and CPF intensity to be a value of 0.1, indicating that the concentration of Fe-Ti oxides is a good predictor of the CPF intensity rank within ODP Hole 1105A. The *R* model also found that depth was positively correlated with CPF intensity within ODP Hole 1105A with a correlation value of 0.45. Interestingly olivine concentration had a -0.32 in correlation to CPF intensity, meaning that it was the highest reverse predictor of CPF intensity within ODP Hole 1105A. Grain size has a -0.02 correlation factor with CPF intensity rank, indicating grain size was also a reverse predictor of the CPF intensity. To illustrate the correlation the Fe-Ti oxide concentration values and the CPF intensity ranking values were plotted against each other in Figure 5.15. The trend line, with a slope of 0.1384 and an R^2 value of 0.1927, shows how with increasing Fe-Ti oxide values there is an increase in CPF values.

The subpopulation multiple regression model results for ODP Hole 1105A can be seen in Figure 5.16. The subpopulation used in this round of statistics was a subgrouping of all thin sections that had a Fe-Ti oxide concentration of 5% or more. There was little change in the correlation values for both depth and Fe-Ti oxide concentration, but their respective correlation values dropped slightly. The most interesting changes were in regard to the grain size, Fe-Ti oxide concentration and olivine concentration variables.

The grain size correlation value spiked drastically, changing from -0.02 to a higher value of -0.49. Most interestingly is that Fe-Ti oxide and olivine concentration values became opposite of what they were in the complete dataset test; with Fe-Ti oxides value changing to a -0.009 and olivine's value changing to a 0.2.

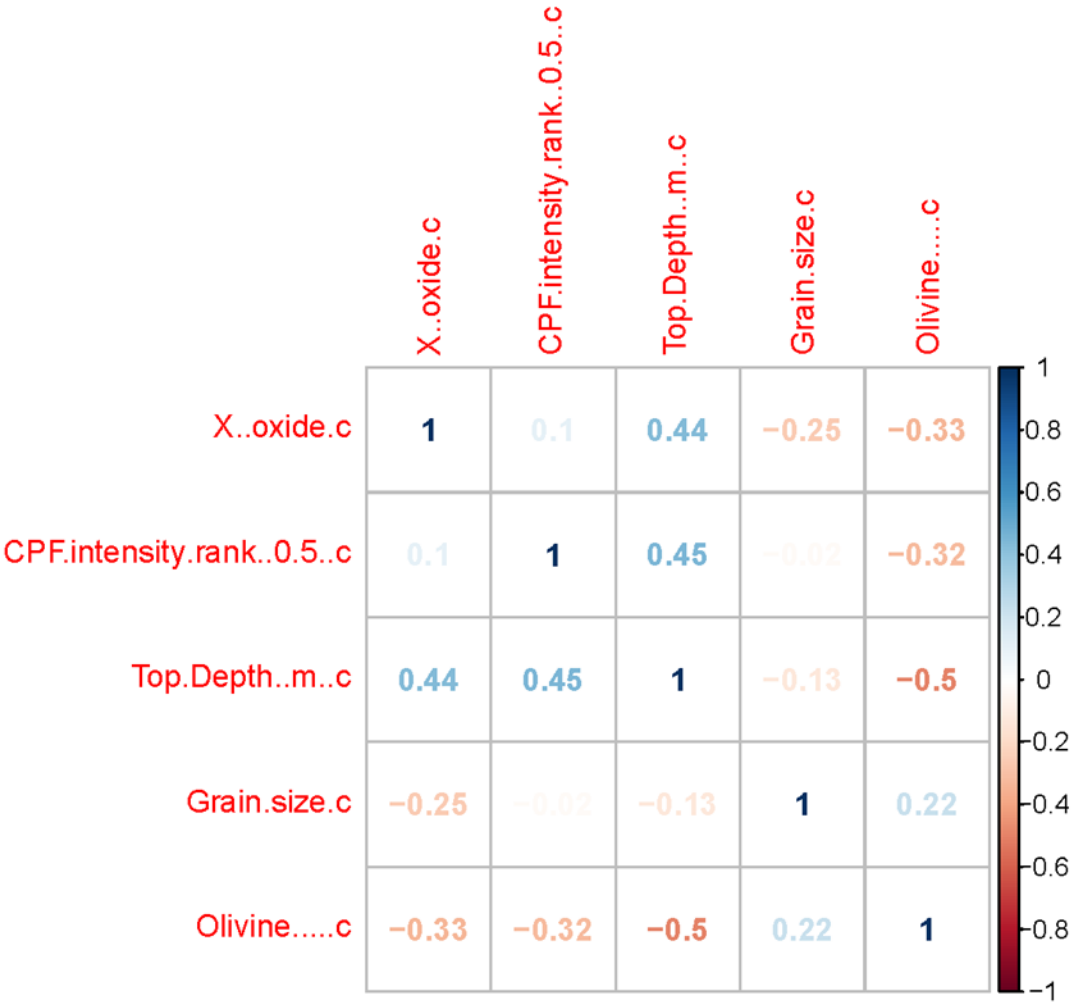

Figure 5.14 *R* results correlation plot for ODP Hole 1105A

The output of the multiple regression done in the statistical software package R; using the data gathered for ODP Hole 1105A.

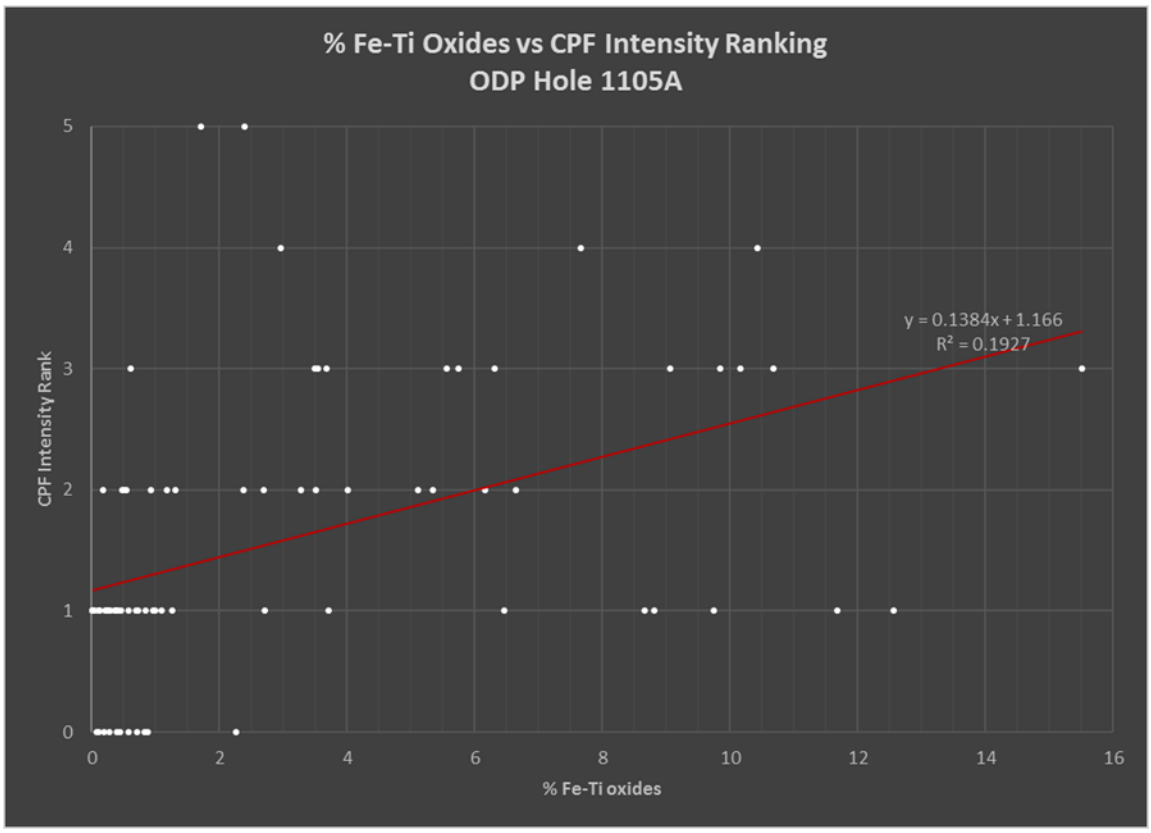

Figure 5.15 Fe-Ti oxides by CPF, ODP Hole 1105A

The correlation between Fe-Ti oxide concentration and CPF intensity within ODP Hole 1105A. The general trend between them is shown using the red trend line which is indicating that with increasing Fe-Ti oxide concentration within a thin section sample there is a corresponding increase in CPF intensity of the thin section sample.

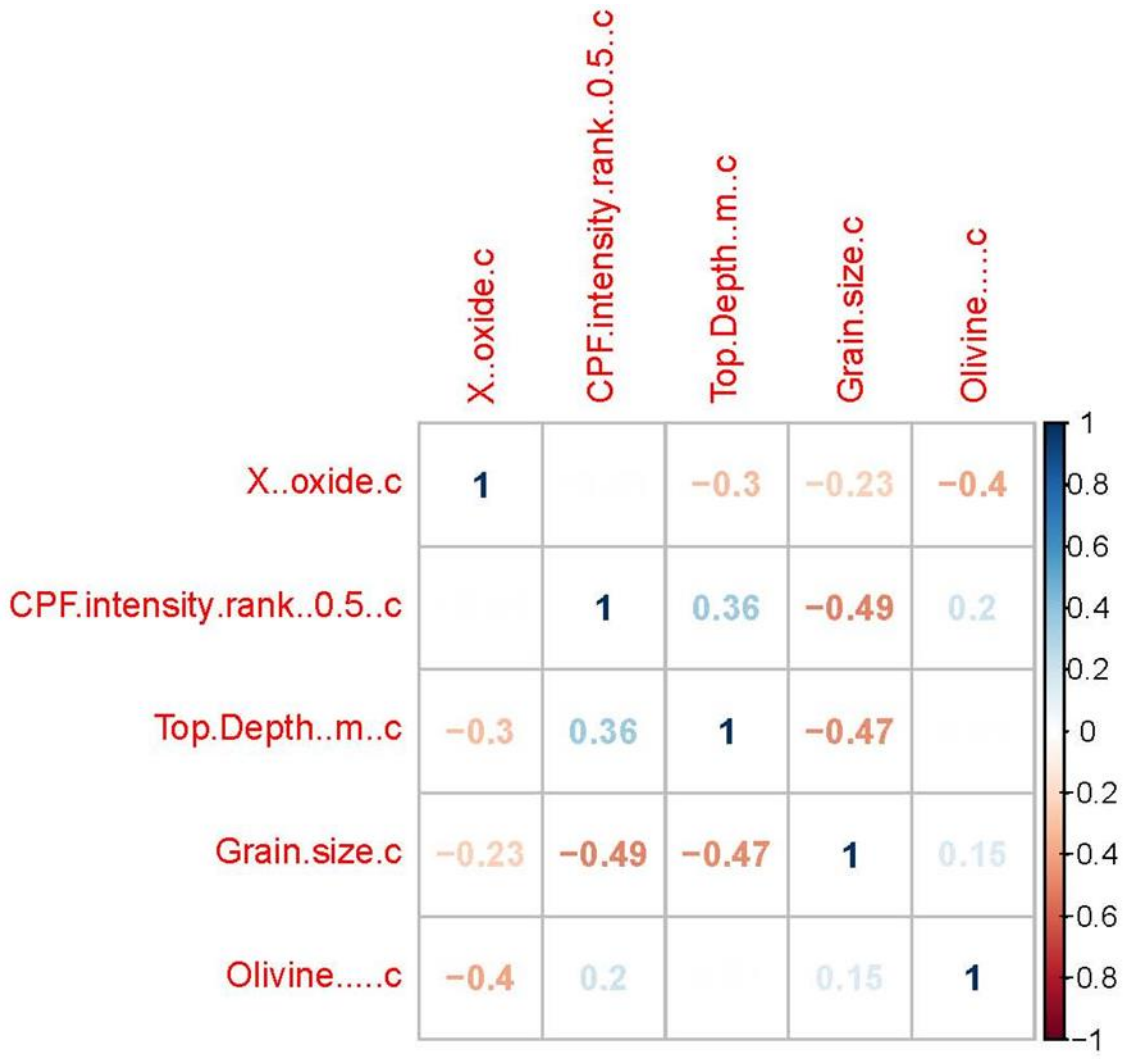

Figure 5.16 *R* results correlation plot for the subpopulation of ODP Hole 1105A

The correlation values between the five variables used in this study for the subpopulation of thin sections with Fe-Ti oxide concentrations over 5% within ODP Hole 1105A. Fe-Ti oxide concentration correlation value with CPF intensity is -0.009.

5.1.4 ODP Hole 735B

Two hundred four thin sections were used to examine ODP Hole 735B from various sources including 52 shipboard samples from Leg 118 (Shipboard Scientific Party, 1991), 69 samples from Leg 176 from Dr. Aaron Yoshinobu's personal collection and 83 samples from Leg 176 from Dr. Jay Miller's personal collection.

5.1.4.1 Fe-Ti oxides

Generally, the Fe-Ti oxide concentrations are less than ~2.3%, which accounts for 89.45% of the thin sections, Figure 5.17. There are 13 spikes of Fe-Ti oxide concentrations over 5%; this accounts for 6.37% of the thin sections within ODP Hole 735B, with the remaining 4.18% of the Fe-Ti oxide concentrations falling between ~2.3 and 5%. The range of Fe-Ti oxide concentration calculated within ODP Hole 735B was from 0.000723–29.82%, with the average being ~1.39%. The maximum of 29.82% was in sample 118-735B-46R-2W-7B 128/130. This thin section did however have a carbon film on it for SEM work, Figure 5.18A. Most of the Hole 735B is consistent with the spikes in Fe-Ti oxide concentrations focused in two locations: the top from 14.57–253.47mbsf and middle from 496.54-859.60mbsf in the Hole; with the rest averaging ~1%. The two high concentration sections account for the upper and middle clusters of Fe-Ti oxide spikes over 5%. The other intervals contain the majority of the low concentrations with no spikes over 5%.

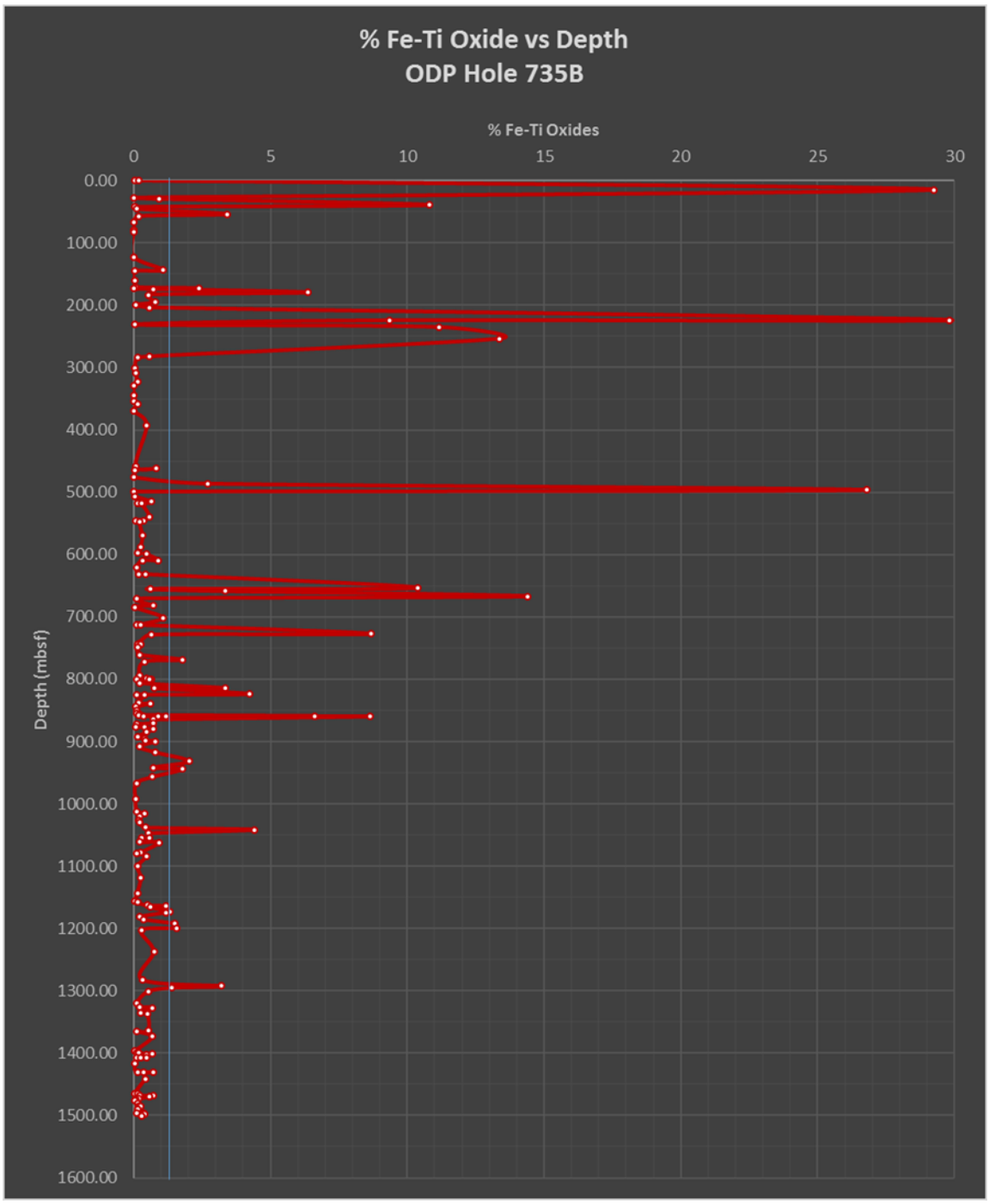

Figure 5.17 Fe-Ti oxides by Depth, ODP Hole 735B

The down hole concentration variations of Fe-Ti oxides within ODP Hole 735B. The blue line is the average Fe-Ti oxide concentration of 1.38%.

5.1.4.2 CPF

Figure 5.19 shows the variated CPF intensity within ODP Hole 735B versus depth. There are several relationships between CPF intensity and Fe-Ti oxide concentration that can be ascertained from this data. Aside from 3 of the 218 thin sections in this study, any thin section with an Fe-Ti oxide concentration of 5% or higher also has a CPF intensity ranking of 2 or higher, Figure 5.18B is an example of this. There are 13 thin sections that have over 5% Fe-Ti oxides; 10 of these thin sections or 76.9% of the 13, show this relationship. The three thin sections with a Fe-Ti oxide concentration higher than 5% that do not show this relationship are located within the middle section of ODP Hole 735B; an example of this is Figure 5.18C. The other two observations come from simply comparing the presence of Fe-Ti oxides and crystal-plastic deformation presence in the thin sections without considering the amount of oxide concentration or the CPF intensity rank. In addition, wherever there is a CPF intensity rank higher than 0, there are always Fe-Ti oxides present. This concentration, however, is not always significant, as some Fe-Ti oxide concentrations are as low as 0.002%; Figure 5.18D is one such example. This means that within ODP Hole 735B Fe-Ti oxides are present wherever crystal-plastic deformation occurred. The reverse of this relationship is also observed, since there is not always crystal-plastic deformation wherever there are Fe-Ti oxides present. Five of the 218 thin sections have Fe-Ti oxide concentrations ranging from ~0.204–8.689%, but have no CPF rank which accounts for 2.29% of the thin sections.

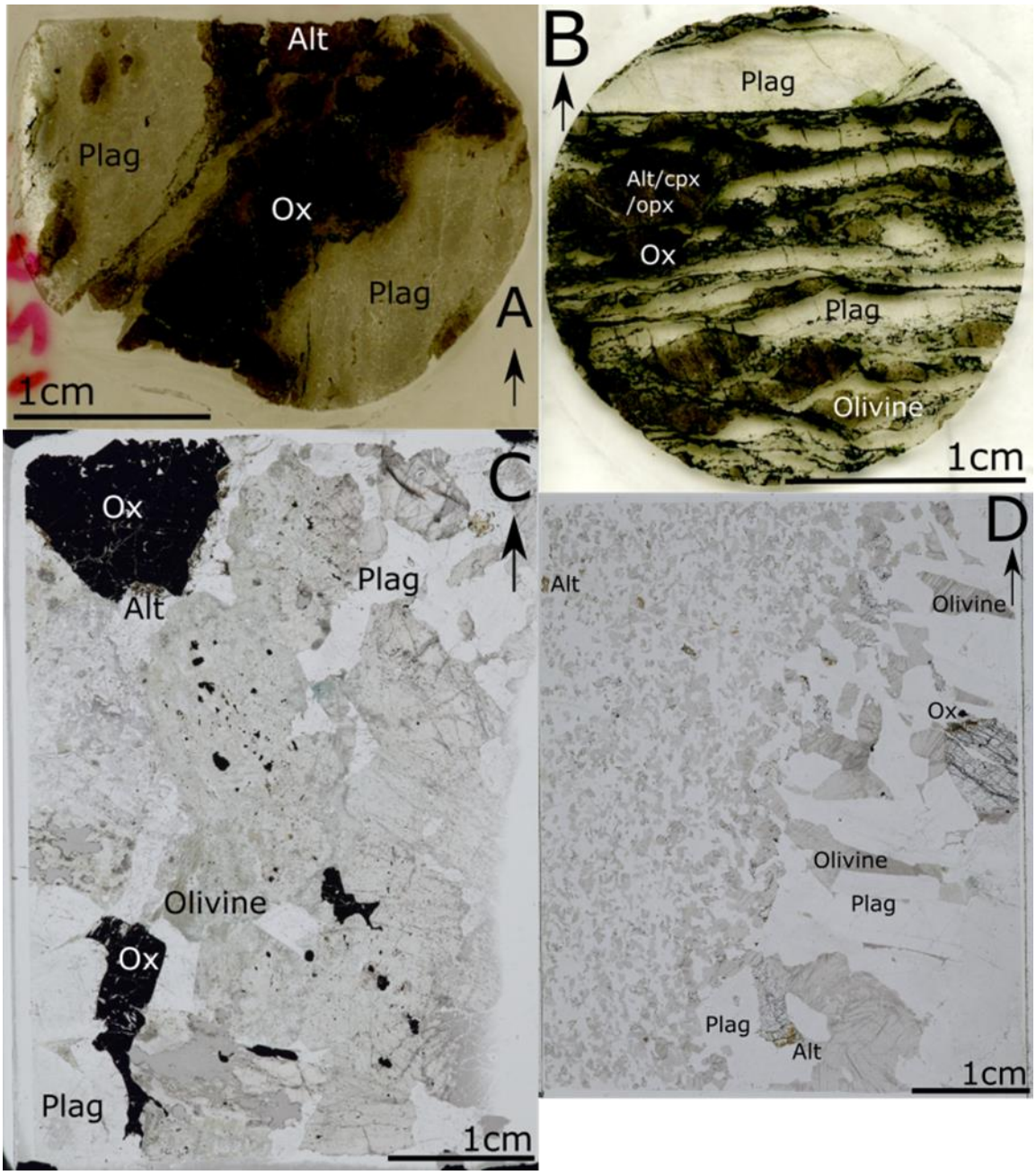

Figure 5.18 Thin section compilation from ODP Hole 735B

The black arrows show up core direction. A) Thin section 118-735B-46R2W-7B at a depth of 223.71mbsf has the highest Fe-Ti oxide concentration at 29.828%; however, it is one of the thin sections with the carbon film on it which strains the Fiji software. B) Thin section 176-735B-87R-5W-3 at 496.54mbsf has one of the highest Fe-Ti oxide concentrations at 26.781% and has a high CPF value of 4. C) Thin section 176-735B-121-6-1C at 727.08mbsf has an Fe-Ti oxide concentration over 5% of 8.689% but still has a low CPF value 0. D) Thin section 176-735B-207R-4-1B at 1473.83mbsf has a low Fe-Ti oxide concentration of 0.06 and a CPF value of 1.

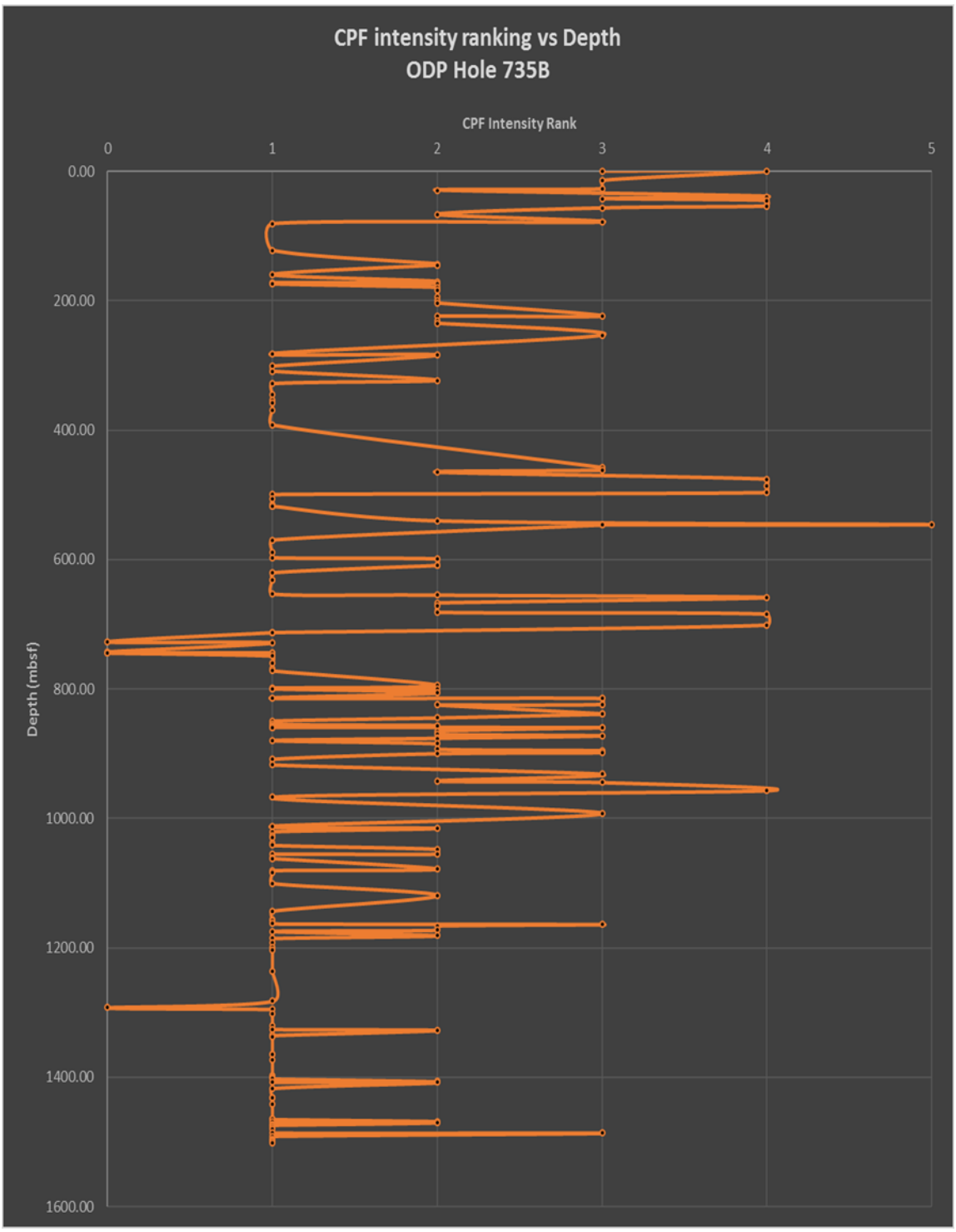

Figure 5.19 CPF by Depth, ODP Hole 735B

The down hole fluctuations of the CPF intensity rank using the thin sections top depth within ODP Hole 735B.

5.1.4.3 Olivine

The presence of olivine versus the presence of Fe-Ti oxides was another aspect that this study examined. The olivine content within ODP Hole 735 is highly variated with numerous high peaks throughout the hole (Figure 5.20). The olivine content the minimum value was reported as 0%, the maximum value reported was 60%, which occurs at the 462.02 mbsf peak, and the average reported value for olivine was ~9.71%. The relationship between Fe-Ti oxide and olivine percent versus depth, Figure 5.21, indicates that when there is a higher percentage of olivine, the Fe-Ti oxide concentration is either reduced or absent and vice versa.

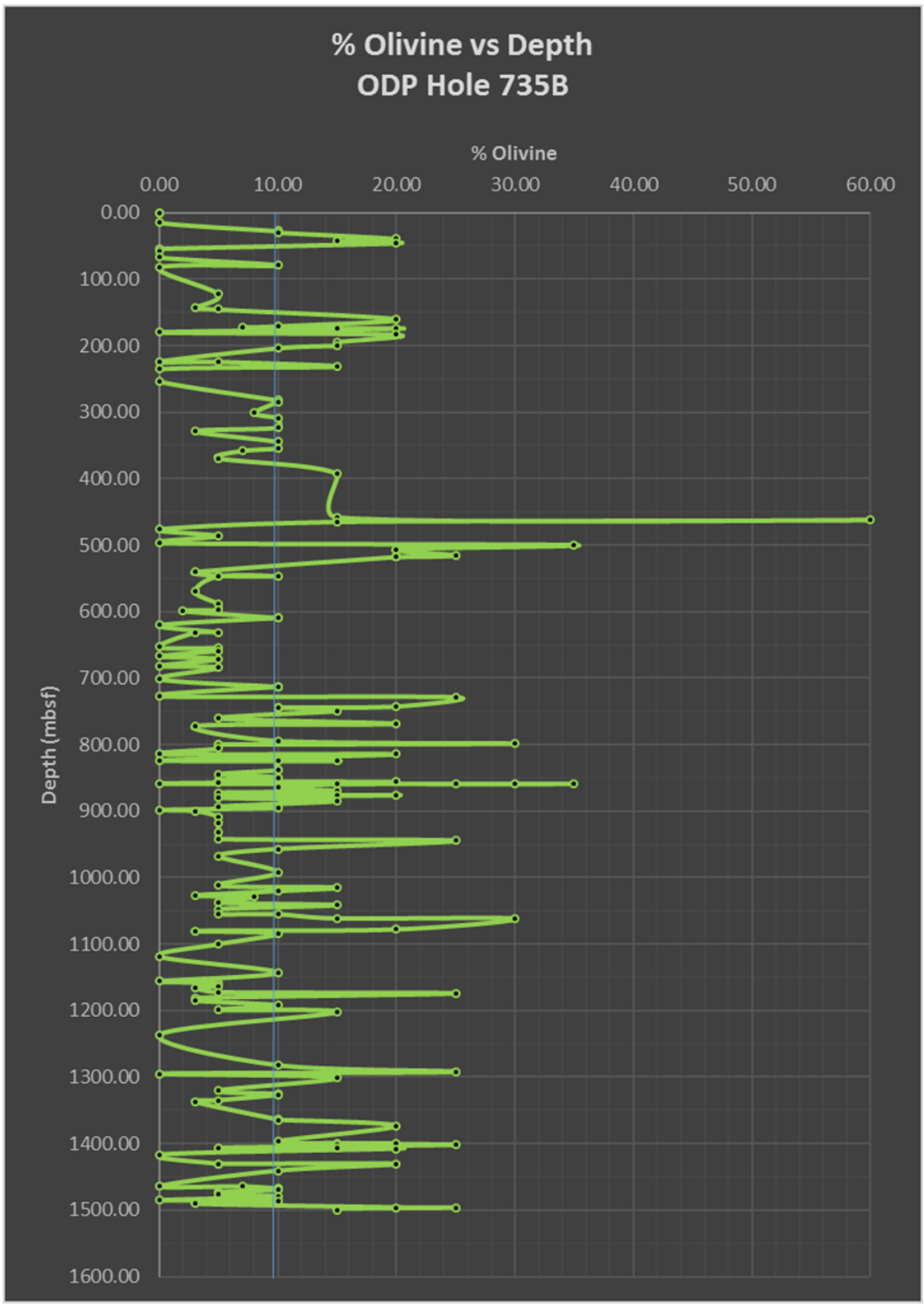

Figure 5.20 Olivine by Depth, ODP Hole 735B

The variability of the percent of olivine concentrations within the thin section samples throughout ODP Hole 735B with depth. The blue line is the average olivine concentration of 9.7%.

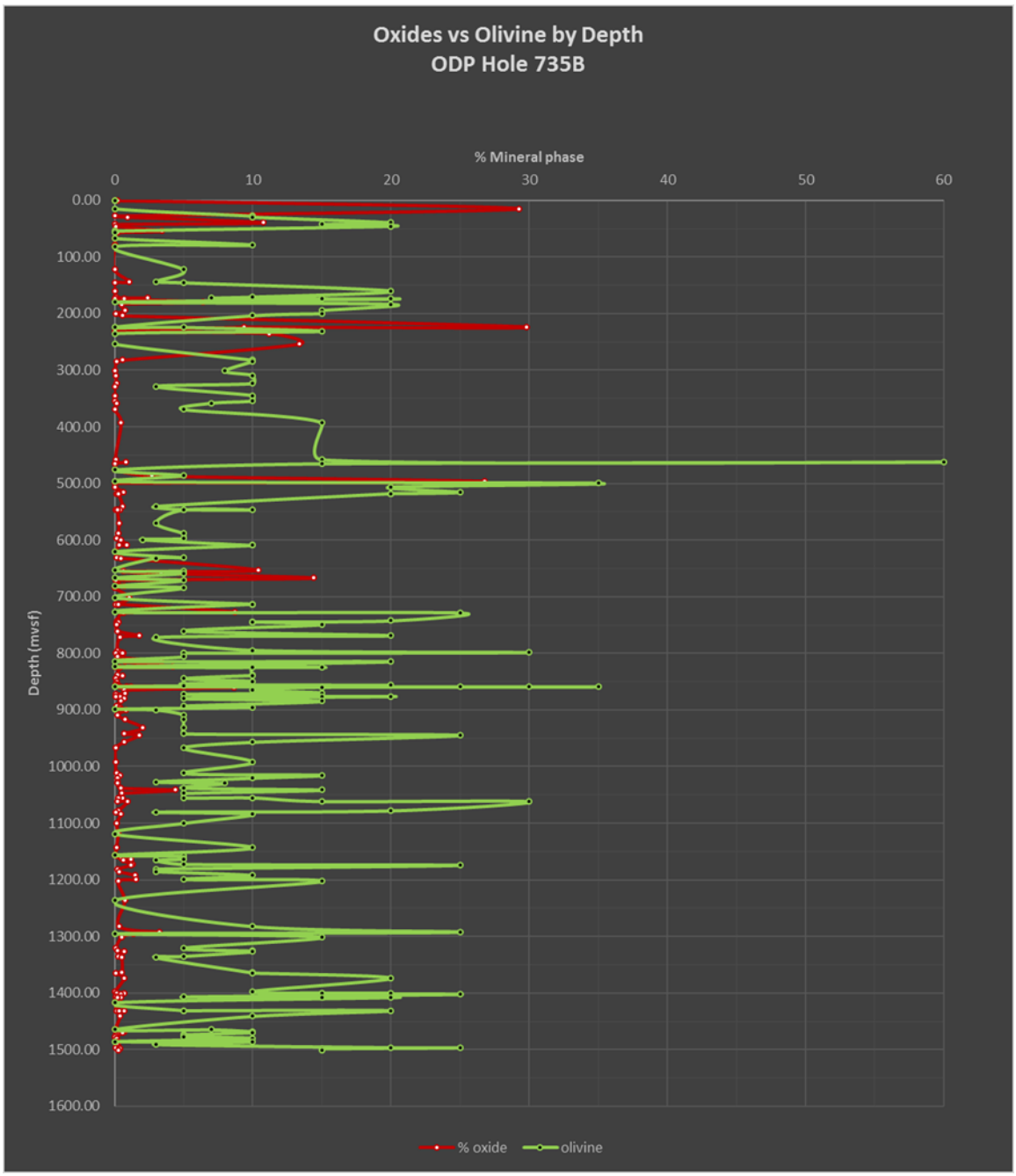

Figure 5.21 Fe-Ti oxides and Olivine by Depth, ODP Hole 735B

The general relationship between the mineral phases of olivine and Fe-Ti oxides present within ODP Hole 753B.

5.1.4.4 *R*

The open source statistical software package *R* was used to perform multiple regression models to constrain which factors (e.g., Fe-Ti oxide concentration) may

correlate with the presence of CPF and their intensity, Figure 5.22 shows these results (John Fox and Sanford Weisberg, 2011; R Core Team, 2015). The *R* software calculated the correlation between Fe-Ti oxide content and CPF intensity to be 0.24, indicating that the concentration of Fe-Ti oxides is a good predictor of the CPF intensity rank. An interesting correlation that was found in the multiple regression model was that olivine concentration had a -0.55 in correlation to CPF intensity, meaning that it was the highest reverse predictor of CPF intensity. Grain size -0.08 and depth -0.43 were also reverse predictors of the CPF intensity. These results leave Fe-Ti oxide concentration as the only positively correlating variable. To illustrate this correlation, the Fe-Ti oxide concentration values and the CPF intensity ranking values were plotted against each other in Figure 5.23. The trend line, with a slope of 0.0602 and an R^2 value of 0.644, shows how with increasing Fe-Ti oxide values there is an increase in CPF values.

The subpopulation multiple regression model calculated correlations for all thin sections that had a Fe-Ti oxide concentration of 5% or more within ODP Hole 735B; the outcome of this model had some interesting results (Figure 5.24). The first was a drastic change in the correlation values for all the variables used in testing; both depth and grain size remained negatively correlating variables but showing an even stronger negative correlation with their values spiking to -0.65 and -0.87 respectively. The most interesting things that happened were in regards to the Fe-Ti oxide and olivine concentration variables. The Fe-Ti oxides correlation value doubled to 0.55 showing even more negative correlation than before; but most interesting is that olivine became a positive correlating variable with a value of 0.36.

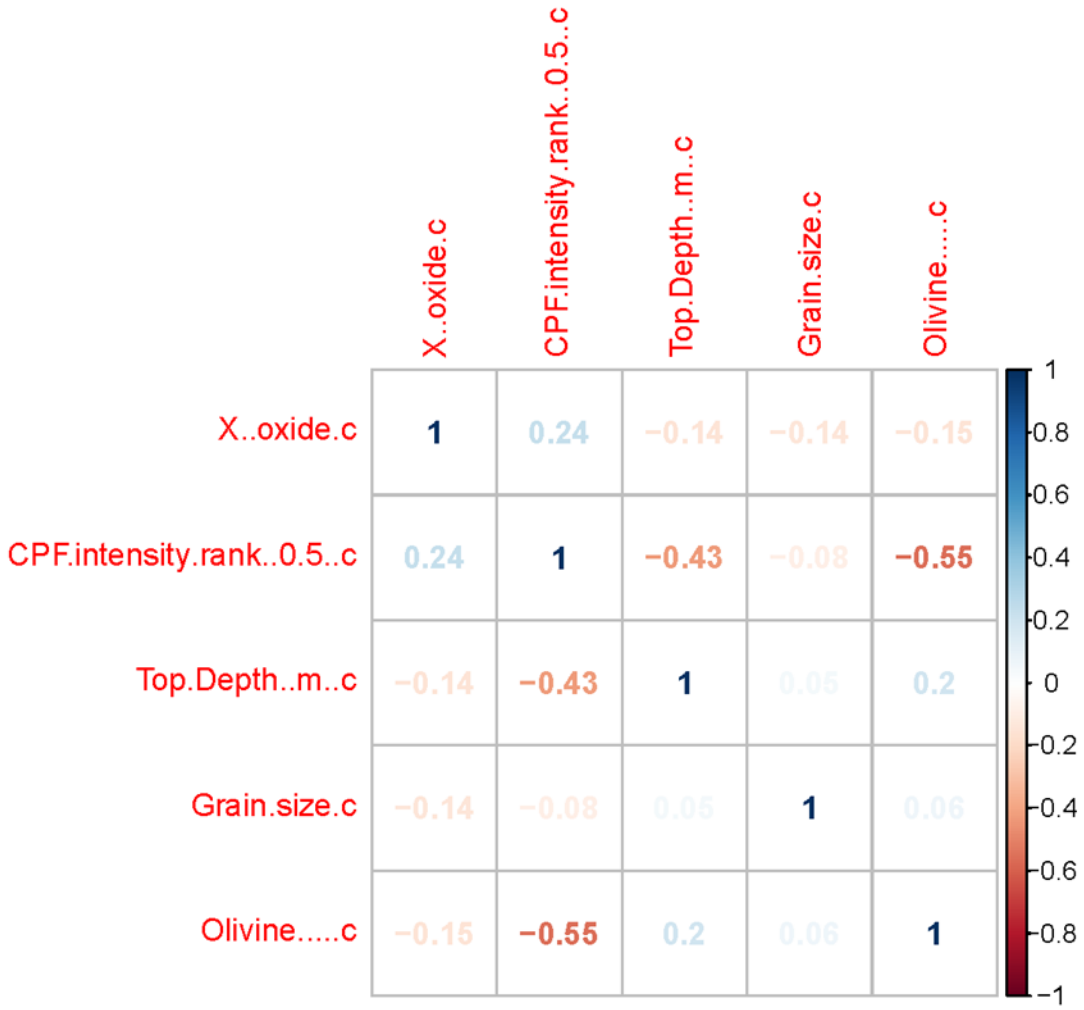

Figure 5.22 *R* results correlation plot for ODP Hole 735B

The output of the multiple regression done in the statistical software package R; using the data gathered for ODP Hole 735B.

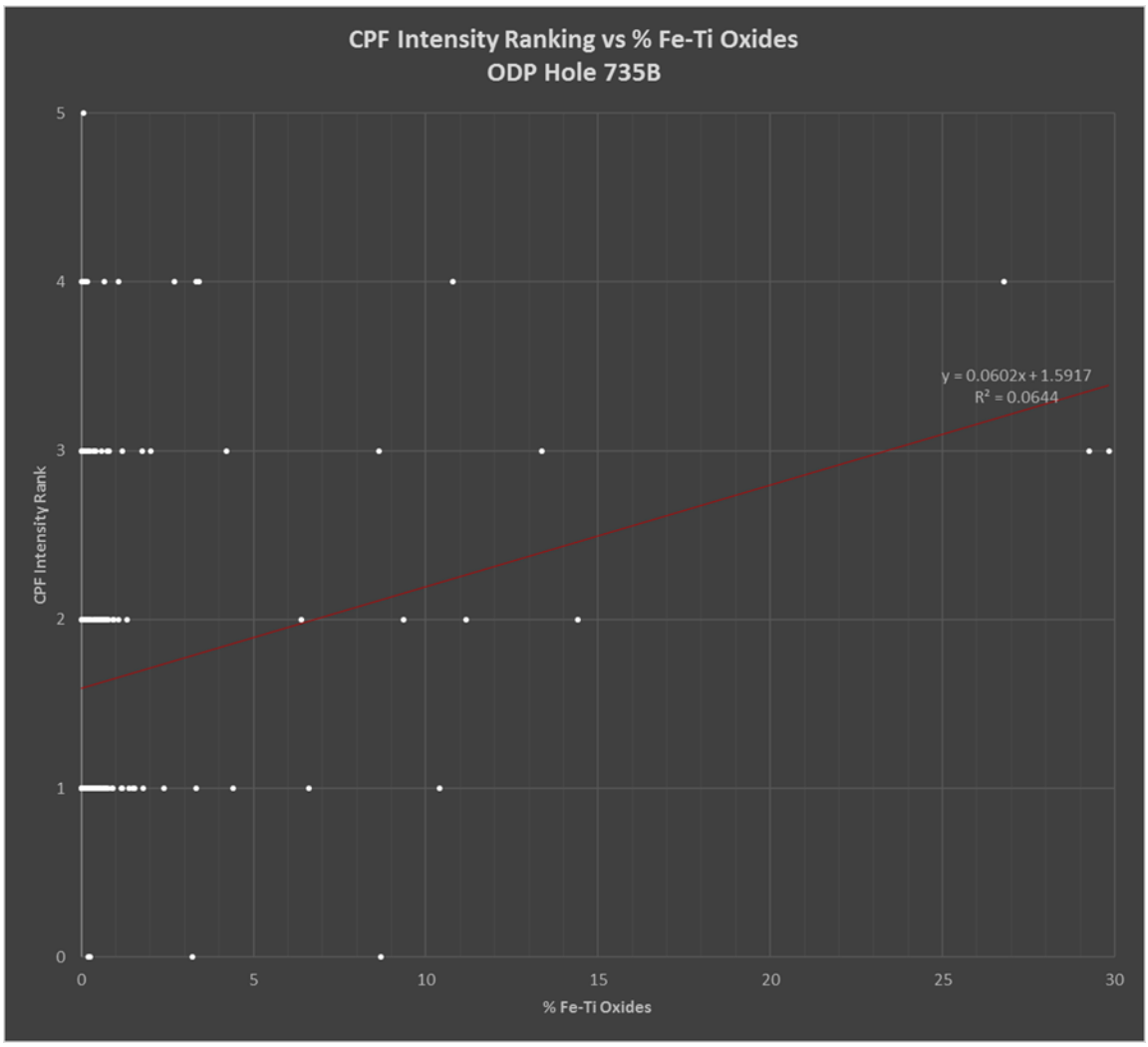

Figure 5.23 Fe-Ti oxides by CPF, ODP Hole 735B

The general trend is shown using the red trend line which is indicating that with increasing Fe-Ti oxide concentration within a thin section sample there is a corresponding increase in CPF intensity.

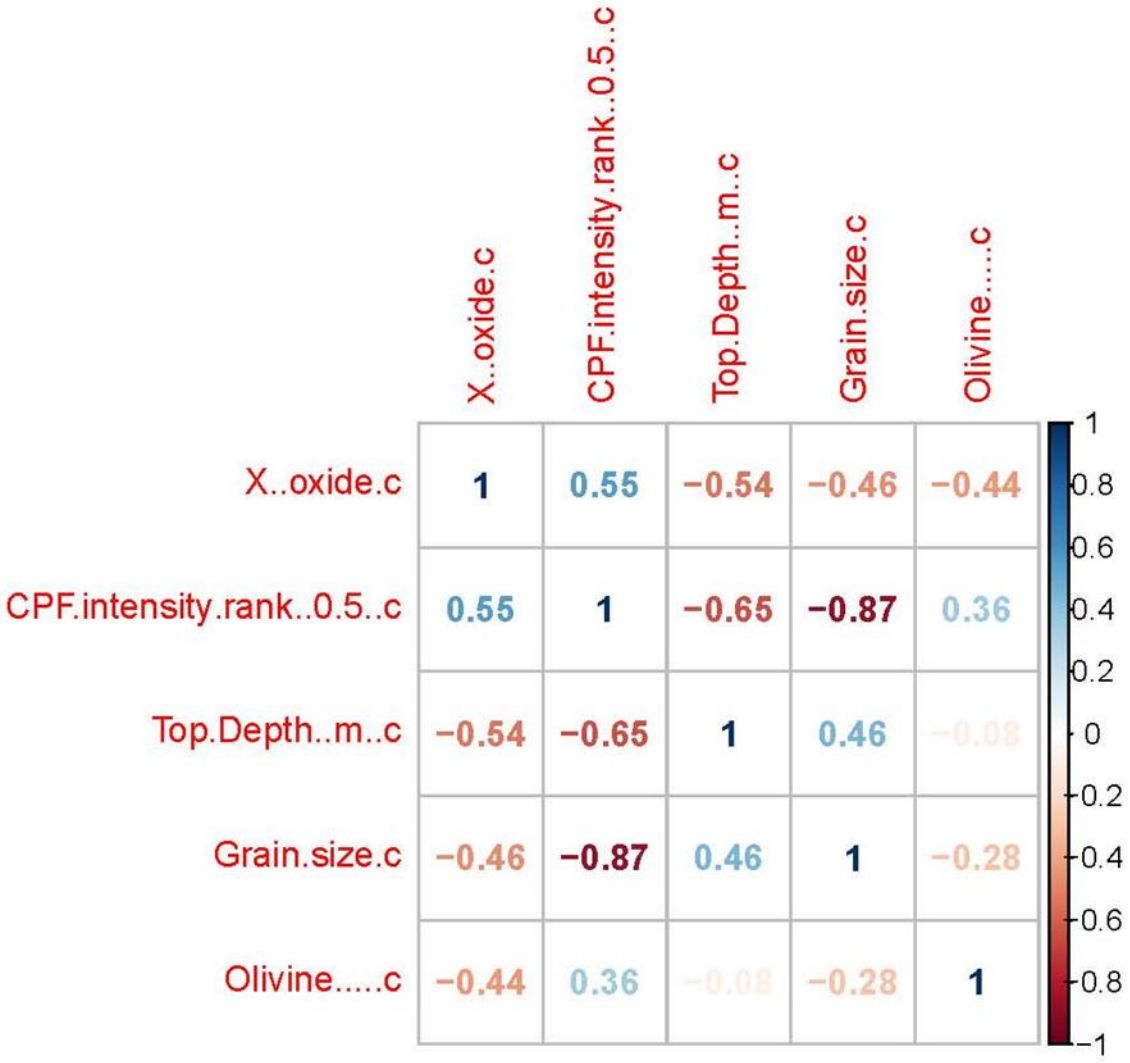

Figure 5.24 *R* results correlation plot for the subpopulation of ODP Hole 735B

Correlation values between the five variables used in this study for the subpopulation of thin sections with Fe-Ti oxide concentrations over 5% within ODP Hole 735B.

5.1.5 All Holes

5.1.5.1 Fe-Ti oxides

There was a total of 552 thin section samples across the three holes used in this study of Atlantis Bank that have a Fe-Ti oxide concentration calculated and a CPF intensity value reported. Of the 552 there were a total of eight thin sections that had no Fe-Ti oxides present, as seen in Figure 5.25, and only one of the eight had no crystal-

plastic deformation present. These eight thin sections only account for 1.27% of the 552 samples used in this study that had CPF values reported. There was a total of seven Fe-Ti oxide deficient samples in IODP Hole U1473A, zero Fe-Ti oxide deficient samples from ODP Hole 1105A, and one Fe-Ti oxide deficient sample in ODP Hole 735B.

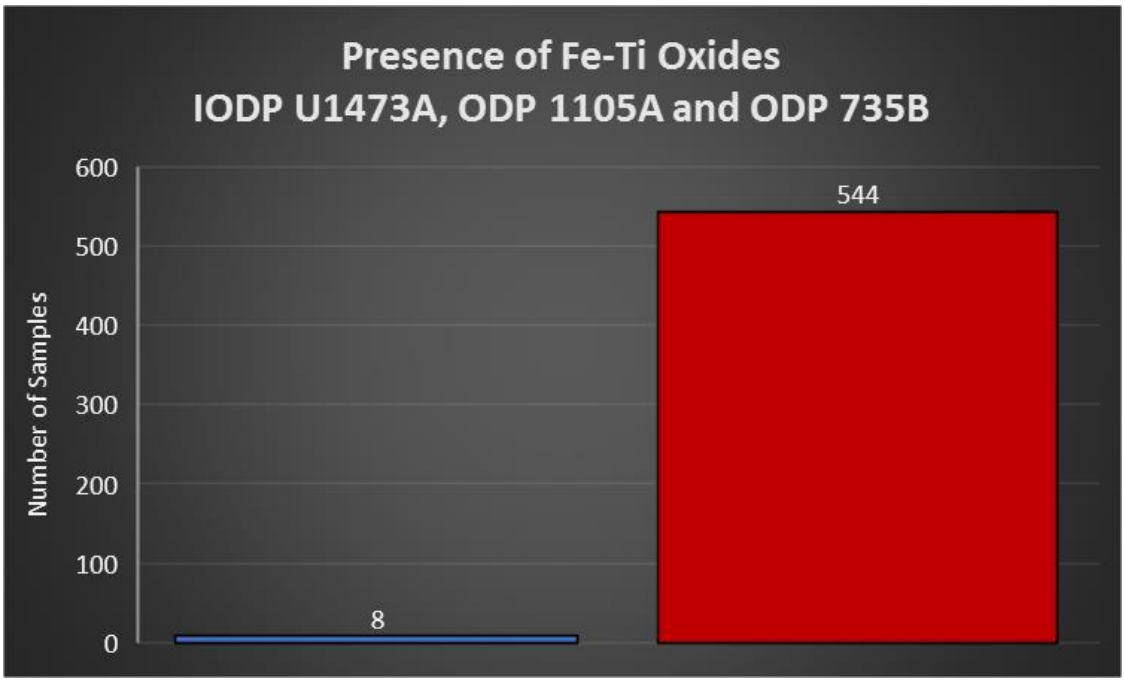

Figure 5.25 Number of samples with Fe-Ti oxides present versus not present

The number of thin section samples that have Fe-Ti oxides present versus the number that do not; this plot was created based on the 552 thin section samples that also had CPF intensities reported from IODP Hole U1473A and ODP Holes 1105A and 735B.

The majority of the Fe-Ti oxides, including nearly all of the thin sections with concentrations over 5%, are between the top and middle of each hole, aside from the peaks towards the base of IODP Hole U1473A (Figure 5.26). ODP Hole 735B had the highest concentrations of Fe-Ti oxides calculated of the three holes. Two of these thin sections were the ones with carbon films on them, which could be in error, but one sample with ~26% Fe-Ti oxides does not have carbon film. ODP Hole 1105A has the highest number of thin sections with Fe-Ti oxide concentrations with a total of twenty,

which is 24.7% of the samples in the hole. This is nearly double the numbers seen in IODP Hole U1473A with 11 samples (3.6% of the hole), and ODP Hole 735B with thirteen samples (6.37% of the hole). ODP Hole 1105A had the highest average Fe-Ti oxide concentration of 2.97%, which is more than double that of the other two holes. Holes ODP 735B and IODP U1473A had close to the same average for Fe-Ti oxide concentration 1.39% and 1.14% respectively.

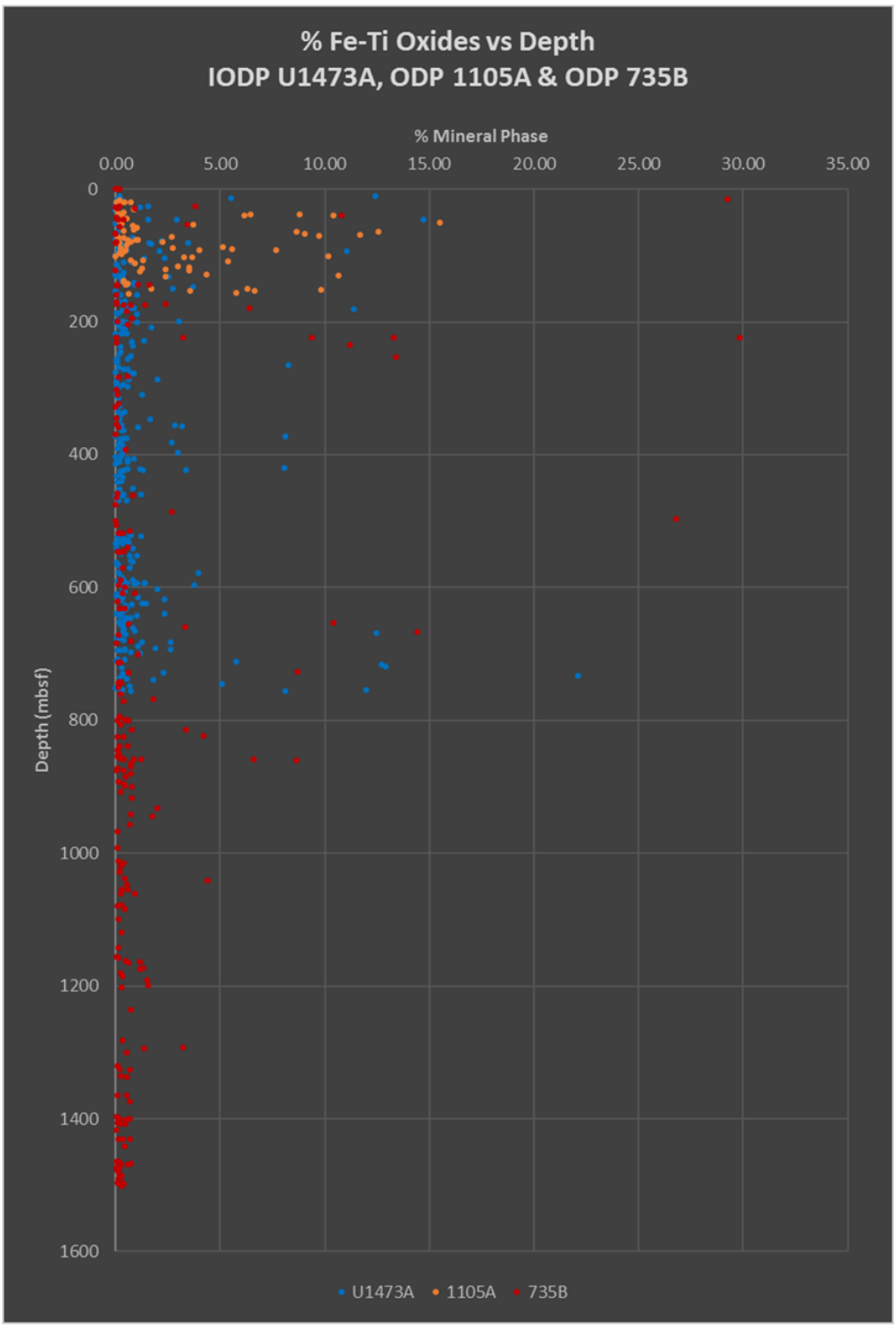

Figure 5.26 Fe-Ti oxide concentration by Depth, All three Holes

Interestingly the spikes of Fe-TI oxide concentrations over 5% seem to stop at ~850mbsf. The two thin sections with ~30% Fe-Ti oxide content within ODP Hole 735B have carbon films on them, the one ~26% does not.

5.1.5.2 CPF

There was a total of 552 thin section samples used in this study of Atlantis Bank that have a CPF intensity value reported. Of the 552 there were fifty thin sections that had no crystal-plastic deformation, as seen in Figure 5.27, and only one of which had no Fe-Ti oxides present. The fifty thin sections that have no crystal-plastic deformation account for 9.05% of the 552 samples used in this study. There was a total of 34 undeformed samples in IODP Hole U1473A (12.88%), eleven undeformed samples from ODP Hole 1105A (13.75%), and five undeformed samples in ODP Hole 735B (2.4%). There were no trends for CPF intensity vs depth other than in ODP Hole 1105A where there was a general trend of increasing CPF intensity rank with increasing depth, hence the positive correlation calculated with *R* (Figure 5.14).

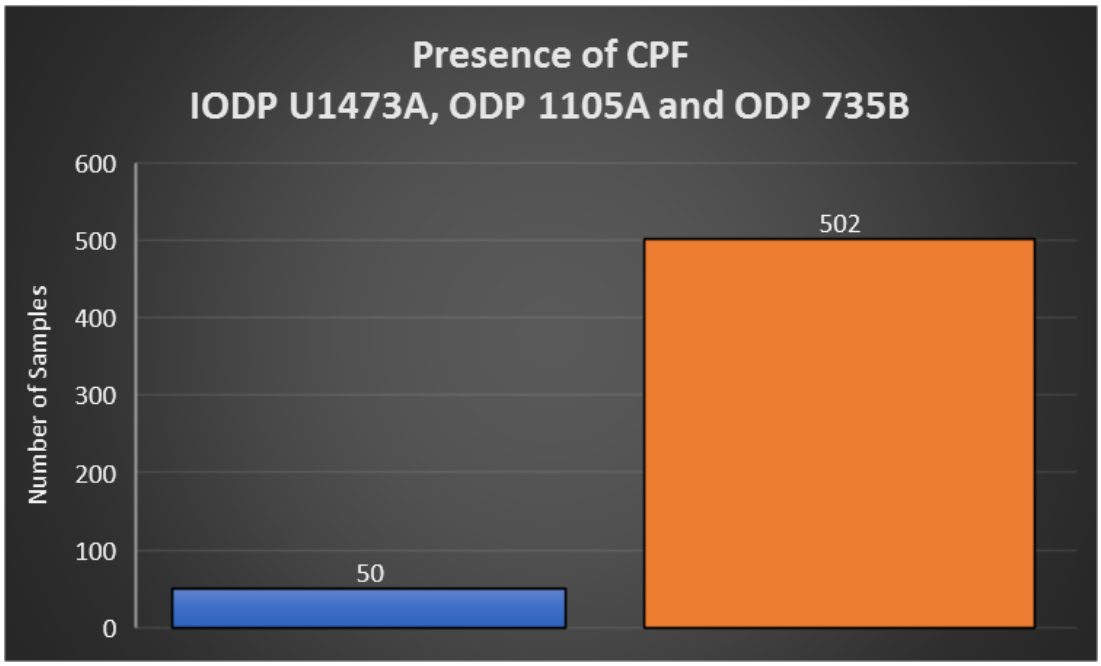

Figure 5.27 Number of samples with CPF present versus not present

The number of thin section samples that have crystal-plastic deformation present versus the number that do not; this plot was created based on the 552 thin section samples that had CPF intensities reported from IODP Hole U1473A and ODP Holes 1105A and 735B.

5.1.5.3 CPF and Fe-Ti oxides

Out of the 552 thin section samples that had both Fe-Ti oxides calculated and CPF values reported there were only fifty-seven samples that did not have both, i.e., a sample had just Fe-Ti oxides and no CPF or vice versa. These 57 samples account for 10.3% of all 552 samples used in this study; forty samples in IODP Hole U1473A, eleven samples in ODP Hole 1105A, and six samples in ODP Hole 735B. In terms of percentages this means these examples accounted for 15.2% within IODP Hole U1473A, 13.75% within ODP Hole 1105A, and 2.88% within ODP Hole 735B.

A relationship between the concentration of Fe-Ti oxides and CPF intensity ranking is present within all three holes (Figure 5.28). Within all three holes there is a trend showing that with increasing Fe-Ti oxide concentration there was a corresponding increase in CPF intensity rank. Holes IODP U1473A and ODP 1105A both had very similar trend lines for this relationship with very similar slopes of 0.1168 and 0.1387, respectively. ODP Hole 735B had a shallower slope of 0.0726; however, it still shows the same positive relationship between Fe-Ti oxide concentration and CPF intensity. The R^2 values for the trend lines from all three Holes are low when including all of the thin sections.

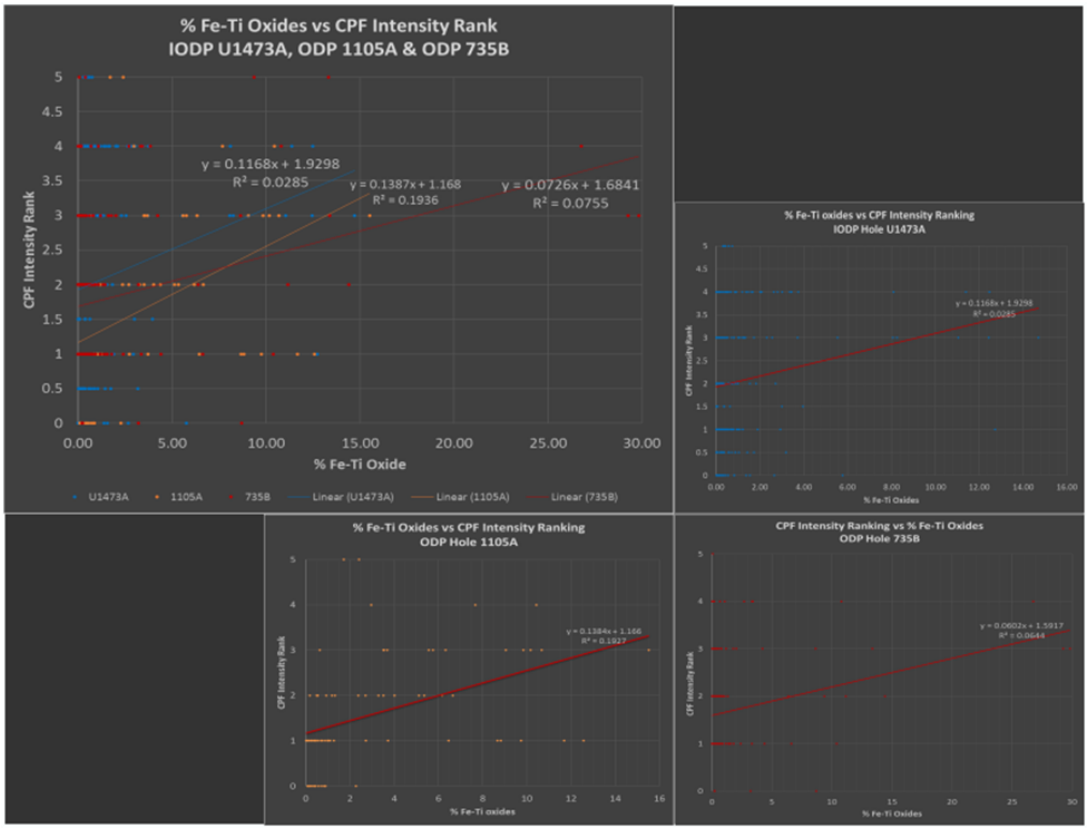

Figure 5.28 Plots of Fe-Ti oxide concentrations by CPF intensity

All three holes have separate trend lines showing the same general relationship.

5.1.5.4 Olivine and Fe-Ti oxides

The olivine concentrations of all three holes were similar as can be seen in Figure 5.29. Aside from one extremely high olivine concentration in ODP Hole 735B at ~60%, the majority of the olivine concentrations within all three holes was between 0% and ~30%. All three holes showed the same general relationship between Fe-Ti oxide and olivine concentrations. Olivine and Fe-Ti oxides have a reverse dependence relationship (Figure 5.30). In all three holes as the Fe-Ti oxide concentrations increased the olivine concentration fell to low levels or was absent all together. The reverse of this was true as well with Fe-Ti oxide concentration being low or nonexistent as the olivine concentration increases.

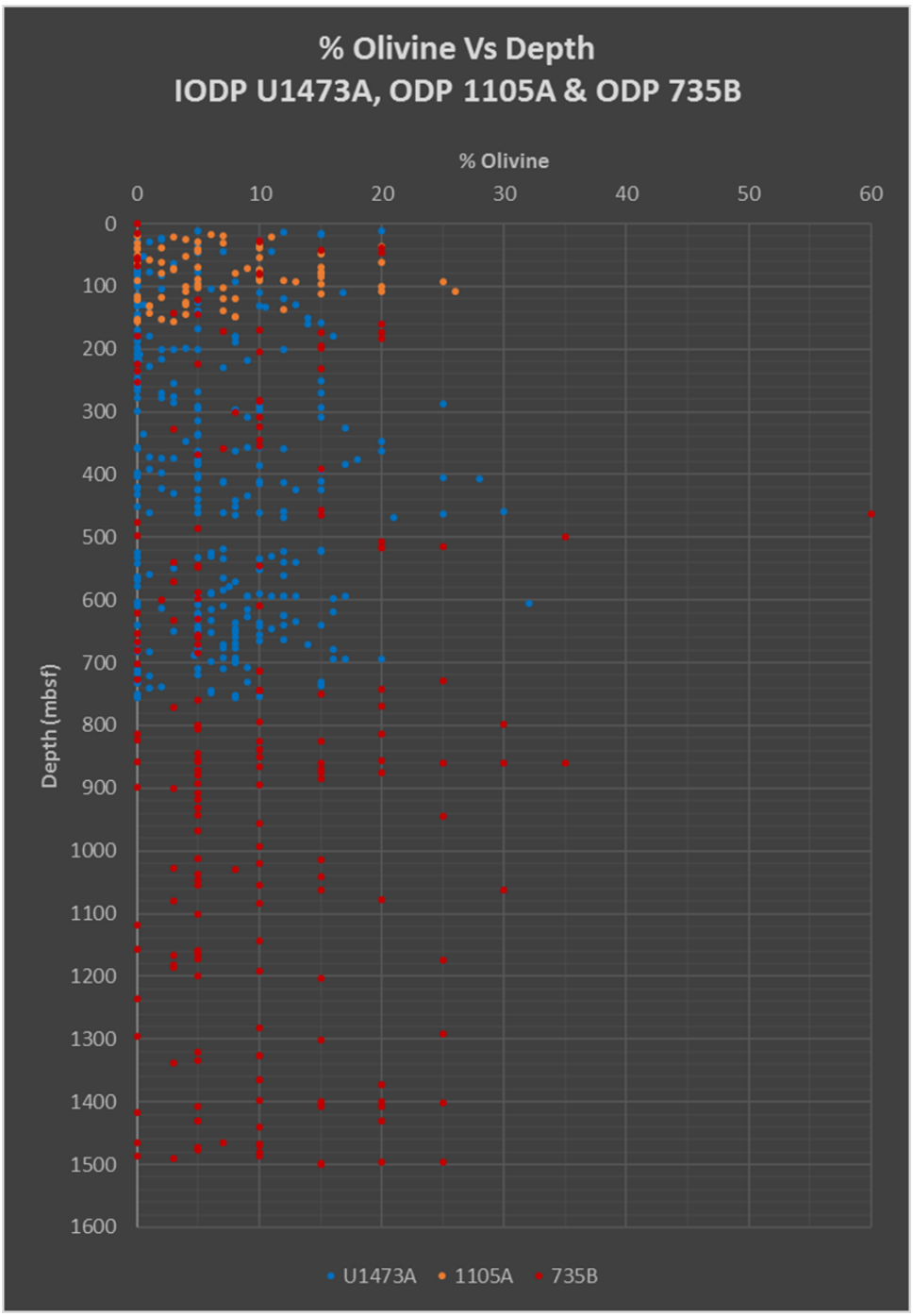

Figure 5.29 Olivine concentration by Depth, All three holes

The olivine content throughout all three holes used in this study of Atlantis Bank, SWIR.

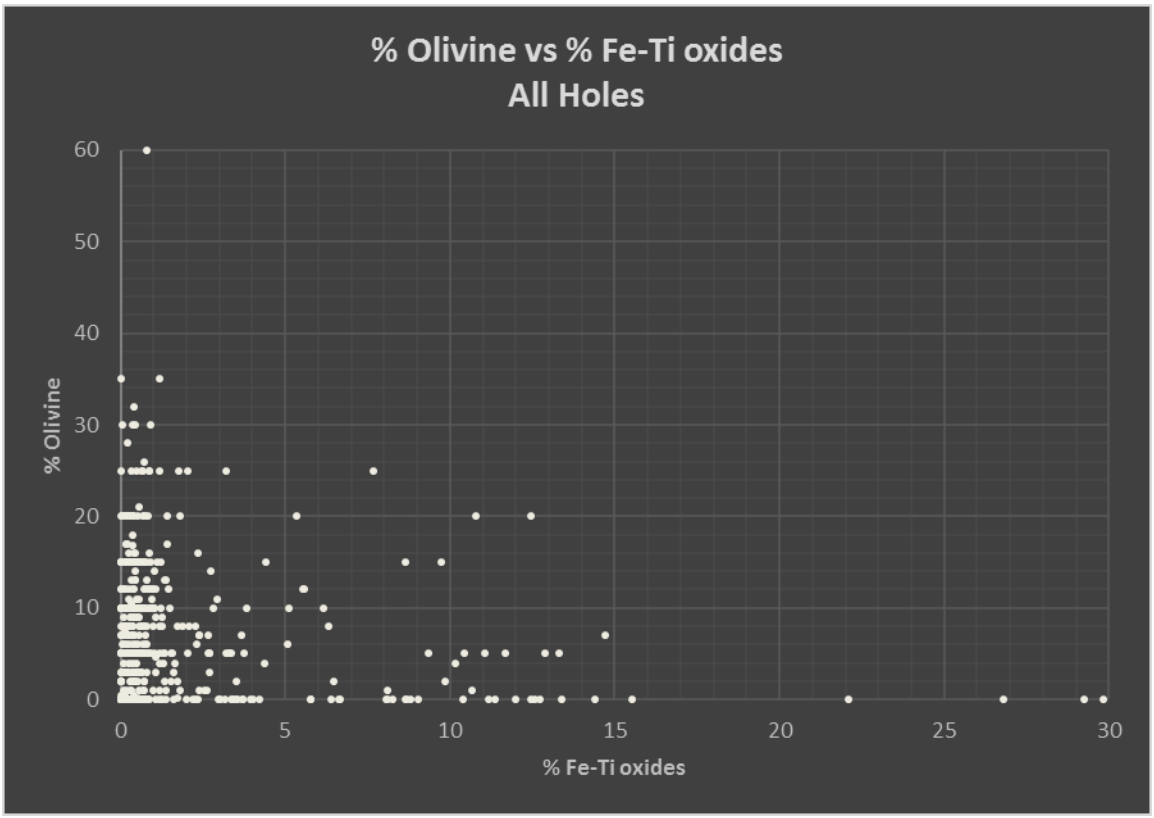

Figure 5.30 Fe-Ti oxide concentration by Olivine concentration, All three holes

Concentration of the mineral phase olivine versus the concentration of Fe-Ti oxides within the samples from IODP Hole U1473A, ODP Holes 1105A and 735B.

5.1.5.5 Grain size versus other variables

Grain size had a negative correlation value among all three holes. Based on the datasets, of samples with 5% or more Fe-Ti oxide content had smaller grain sizes, with higher CPF values and lower olivine contents with ~80.48% being fine-medium grained samples (41.46% fine, and 39.02% medium). In IODP Hole U1473A 63.63% of samples with 5% or more Fe-Ti oxide concentrations were medium grained, with the others being coarse grained. The medium grained samples within IODP Hole U1473A had a higher average Fe-Ti oxide concentration and CPF intensity, and a lower average olivine concentration. In ODP Hole 1105A 55% of the samples with 5% or more Fe-Ti oxide

concentrations were fine grained, 40% were medium grained, and 5% were coarse grained. The fine-grained samples within ODP Hole 1105A had the highest average Fe-Ti oxide concentration and CPF intensity ranking, and low olivine concentration. In ODP Hole 735B 60% of the samples with 5% or more Fe-Ti oxide concentration were fine grained, 30% were coarse grained, and 10% were medium grained. The fine-grained samples within ODP Hole 735B had the highest average Fe-Ti oxide concentration and CPF intensity, and low olivine.

5.1.5.6 *R* results

5.1.5.6.1 All three holes

The same statistical test was run on all of the data to test the relationships across all three holes used in this study (Figure 5.31). The results of running all three datasets through R showed the same general trends seen in the individual holes testing, with Fe-Ti oxide concentration remaining the only positively correlating variable with CPF intensity. The correlation value between Fe-Ti oxide concentration and CPF intensity is 0.18, about the same as the individual hole *R* tests (i.e., 0.12 for IODP U1473A, 0.1 for ODP 1105A, and 0.24 for ODP 735B). As for the other variables, the R software calculated a negative correlation value of -0.19 for depth, a -0.36 for grain size, and a -0.14 for olivine concentration for these variables correlation with CPF intensity.

As with all the individual holes the final stage of the statistical testing was to run the tests on the subpopulation of thin sections with over 5% Fe-Ti oxide concentration from all three holes (Figure 5.32). Based on the results seen in Figure 5.32, it can be stated that there were the same general trends present with all of the individual Hole tests. With the concentrations of Fe-Ti oxides and olivine being the only positive correlation

values with CPF intensity, and depth and grain size having negative correlation values with CPF intensity. The subpopulation of thin sections with 5% or more Fe-Ti oxide concentration from all three datasets produced the highest positive correlation between Fe-Ti oxides and CPF intensity at a value of 0.26. The subpopulation also and had a correlation value of 0.08 for olivine concentration and CPF intensity, a -0.2 correlation value for depth and a -0.56 correlation value for grain size with regards to CPF intensity.

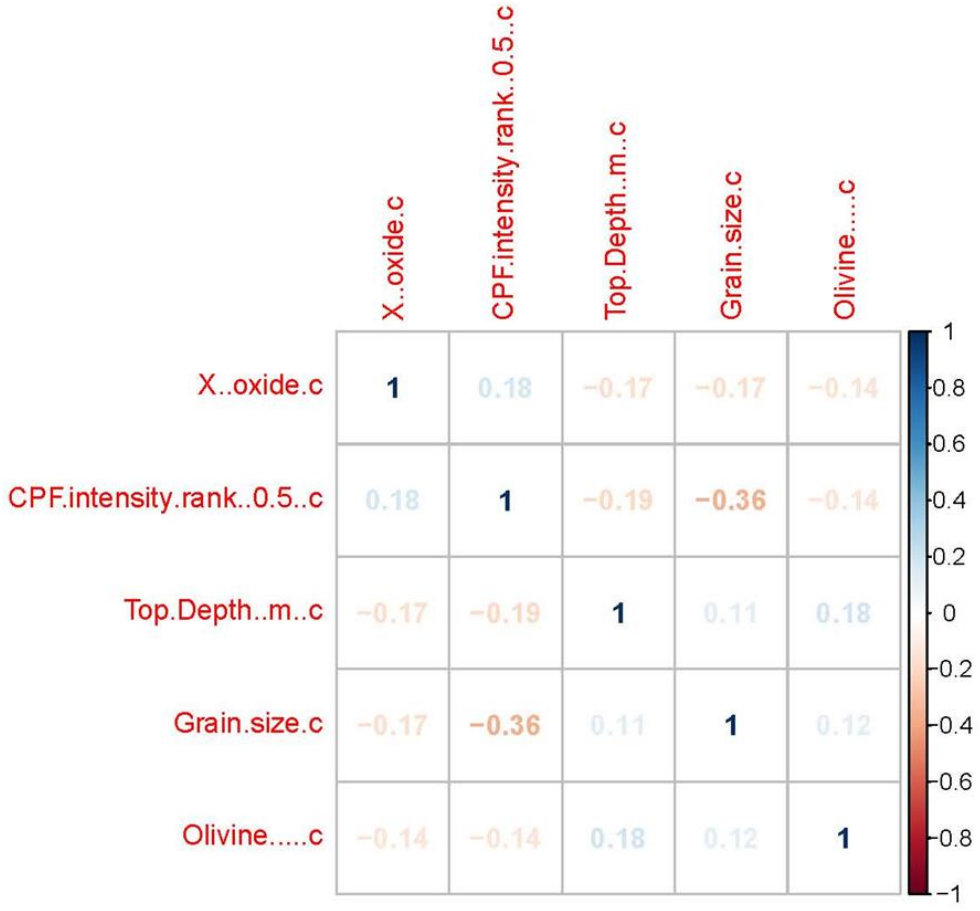

Figure 5.31 *R* results correlation plot for all three holes

This correlation plot was created in the *R* statistical software to show the correlation values between the five variables used in this study for all three holes.

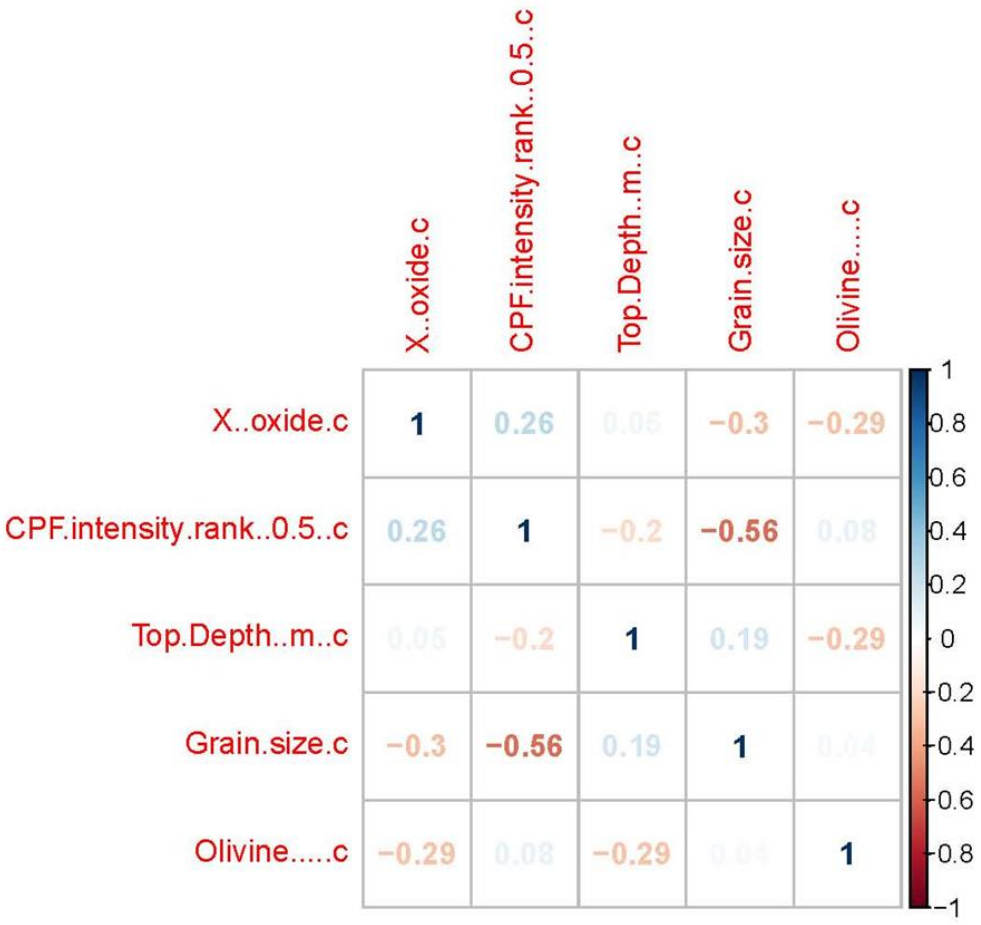

Figure 5.32 *R* results correlation plot for the subpopulation of all three holes

This correlation plot was created in the *R* statistical software to show the correlation values between the five variables used in this study for the subpopulation of thin sections with Fe-Ti oxide concentrations over 5% within all three holes.

5.1.5.6.2 *R* test results in general

The statistical models run in the R software package produced some interesting results that agree in some aspects across the three holes, but also disagrees in a few respects. The first major similarity in this study was the fact that in all tests, aside for the ODP 1105A subpopulation test, there was a positive correlation between Fe-Ti oxide content and CPF intensity rank. Within the subpopulation datasets and complete datasets testing the grain size correlation with CPF intensity was the only variable to stay the same, with respect to negative or positive correlation.

There were a couple of points where the tests did not all produce similar results. For example, in all three datasets Fe-Ti oxide concentration was always in positive correlation with CPF intensity ranking; however, in ODP Hole 735B this correlation value was double that of IODP Hole U1473A and ODP Hole 1105A. Depth below the seafloor was another aspect in which the correlations were not always in agreement. ODP Hole 1105A had a positive correlation between depth below the seafloor and the CPF intensity ranking, with the CPF values starting out low at the top and getting higher as depth increased (Figure 5.11). This correlation, however, was not present in either of the other two holes.

There were a few cases where the statistics did not agree across all three holes in the subpopulation testing as with the full datasets. The subpopulation test of ODP 1105A was the only hole to have a negative correlation value for Fe-Ti oxide concentration, and it was also the only hole to have a positive correlation value for depth. Aside from IODP Hole U1473A, all of the subpopulation tests produced a positive correlation value for olivine.

CHAPTER VI Discussion

6.1 Discussion

One of the main goals of this study was to create a dataset detailing Fe-Ti oxide concentrations within Atlantis Bank by utilizing thin section samples from IODP Hole U1473A and ODP Holes 1105A and 735B. Another aspect of this study was to utilize these data in conjunction with data from previous studies to discern potential relationships between the presence and concentration of Fe-Ti oxides and crystal-plastic deformation within Atlantis Bank. Several observations must be explained to form a model for the relationship between Fe-Ti oxides, crystal-plastic deformation, and other characteristics from Atlantis Bank. Those observations are as follows: 1) the correlation between Fe-Ti oxide concentration and crystal-plastic deformation in all three holes; 2) how the association between Fe-Ti oxide concentration and olivine concentration affects crystal-plastic deformation; 3) the anomalous correlation between CPF and depth within ODP Hole 1105A; 4) the correlation between Fe-Ti oxides, CPF, and grain size. The following discussion will attempt to explain these phenomena and to discuss the significance of Fe-Ti oxides in the formation of oceanic core complexes.

6.1.1 Fe-Ti oxides and CPF intensity

Till and Moskowitz (2013) stated how zones of increased Fe-Ti oxide concentration can facilitate localization of deformation and also that Fe-Ti oxides deform plastically at lower temperatures than silicates, thus supporting the link between Fe-Ti oxide content and CPF intensity. Several other experimental studies have demonstrated that Fe-Ti oxides are weaker than silicate phases (Atkinson, 1977; Siemes and Hennig-Michaeli, 1985). Bateman (1951) discussed how Fe-Ti oxides can become localized due

to gravitative setting, which causes them to form bands within the rocks they occur in. These bands of Fe-Ti oxides can later be the initiating sites of deformation given that they deform more readily than silicates, and by extension localize shear into those. John and Cheadle (2010) stated that the strain created by detachment faults in OCC's like Atlantis Bank and Kane Mega Mullion, may have been localized into the Fe-Ti oxide gabbros present there. The results from this study including the analysis of the presence of Fe-Ti oxides and CPF indicate a positive correlation between the presence of Fe-Ti oxides and crystal-plastic deformation. The results of this study agree with predictions given that the majority of Fe-Ti oxide-rich thin section samples also have higher degrees of crystal-plastic deformation.

Only 10.3% of the thin section samples used to examine Atlantis Bank did not exhibit the presence of both Fe-Ti oxide mineral phase and crystal-plastic deformation. There are however, possible explanations for this 10.3% of the dataset that does not fit the model. One explanation for this discrepancy is that these thin sections simply did not experience any deformation while Atlantis Bank was being exhumed. So, these samples with more than 5% Fe-Ti oxide must have been shielded from the deformation, with the strain being partitioned elsewhere such as a preexisting weakness (faults, joints, other shear zones, etc.). This is possible since a pre-existing shear zone can be up to 4X weaker than the surrounding gabbro (Mehl and Hirth, 2008). Therefore, even with a high concentration of weaker phases, like Fe-Ti oxides present, this may not be enough to partition strain if there is a weaker zone nearby to facilitate this deformation.

6.1.1.1 Different Fe-Ti oxide-CPF correlation factors between holes

The rocks from Holes IODP U1473A, ODP 1105A, and ODP 735B from Atlantis Bank are similar in age. However, Rioux et al. (2016) noted that the rocks in the upper portion of ODP Hole 735B, which is where the majority of Fe-Ti oxides are concentrated, are older than the rocks of the other holes in Atlantis Bank. This means that with more time ODP Hole 735B should have experienced more deformation than the other two holes. The correlation values for IODP Hole U1473A and ODP Hole 1105A between Fe-Ti oxides and CPF intensity are very close and are half the value of the correlation value from ODP Hole 735B for the same variables. So, it is possible that the relationship between Fe-Ti oxides and CPF intensity may develop with time leading to a stronger correlation through time for older parts of the crust. This is supported by the number of samples that have both Fe-Ti oxides and deformation present. ODP Hole 735B has experienced more deformation through time and has the smallest percentage of undeformed samples (2.88%), but does have Fe-Ti oxide mineral phases present in the undeformed samples.

6.1.1.2 Timing of Fe-Ti oxide localization

Fe-Ti oxide clusters typically crystalize around mafic phases such as clinopyroxene, an observation that has been made by other studies such as Agar and Lloyd (1997) (Figure 6.1). Duchesne (1996) and Bernard et al. (2015) stated how Fe-Ti oxides can move in the melt body or through solid state migration by being forced into low-stress zones creating microstructures called pressure shadows. There are several examples of pressure shadows observed in thin sections from all of the holes used in this study; two thin sections exhibiting this phenomenon from IODP Hole U1473A are in

Figure 6.1. Additionally, Fe-Ti oxide clusters typically have their longest dimension parallel to the crystal-plastic foliations present in the samples. These types of structures are important since they are an indicator that the Fe-Ti oxides were present at the time of the deformation event instead of arriving after.

Another example of Fe-Ti oxide behavior from previous studies is how they can form a lining around shear zones (Agar and Lloyd, 1997). There were several examples of Fe-Ti oxides lining shear zones within thin section samples from IODP Hole U1473A as well; two of the thin sections characterized by this are in Figure 6.2. Both of these phenomena are important indicators of why there is a correlation between Fe-Ti oxides and crystal-plastic deformation as both of these structures are only seen when the Fe-Ti oxides are present during the deformation.

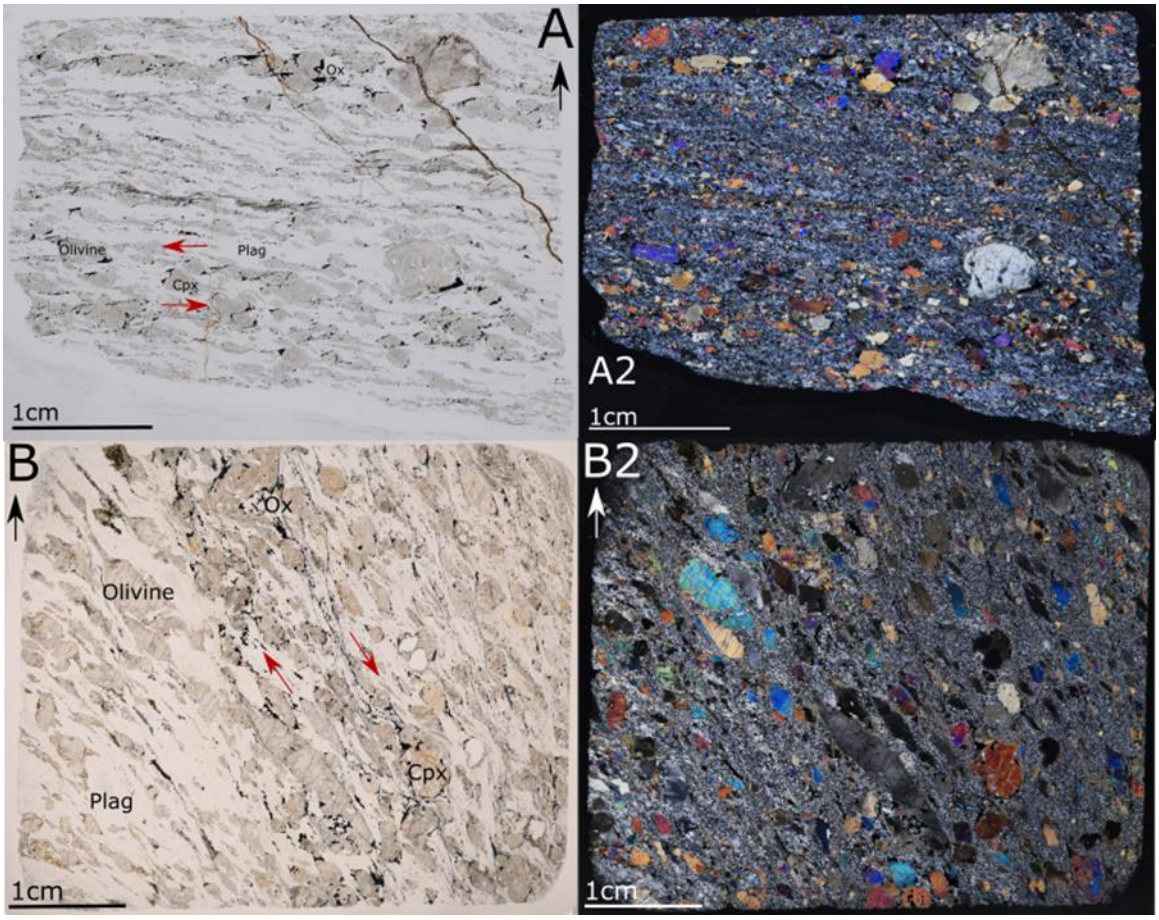

Figure 6.1 Pressure shadows and Fe-Ti oxide mineral association

These thin sections were chosen to illustrate the pressure shadows effects of Fe-Ti oxides within Atlantis Bank. The black/white arrows represent up core direction and the red arrows represent the sense of shear experienced by the respective thin section. The pressure shadows are the Fe-Ti oxide 'tails' streaming to one side or another on the more resistant mineral phases present such as plagioclase feldspar and olivine. A and A2 are the plain polar and crossed polar images respectively of thin section sample 360-U1473A-26R-2-TS-86 taken from a depth of 228.4mbsf within IODP Hole U1473A. B and B2 are the plain polar and cross polar images respectively of thin section sample 360-U1473A-61R-4-TS-207 taken from a depth of 552.35mbsf within IODP Hole U1473A.

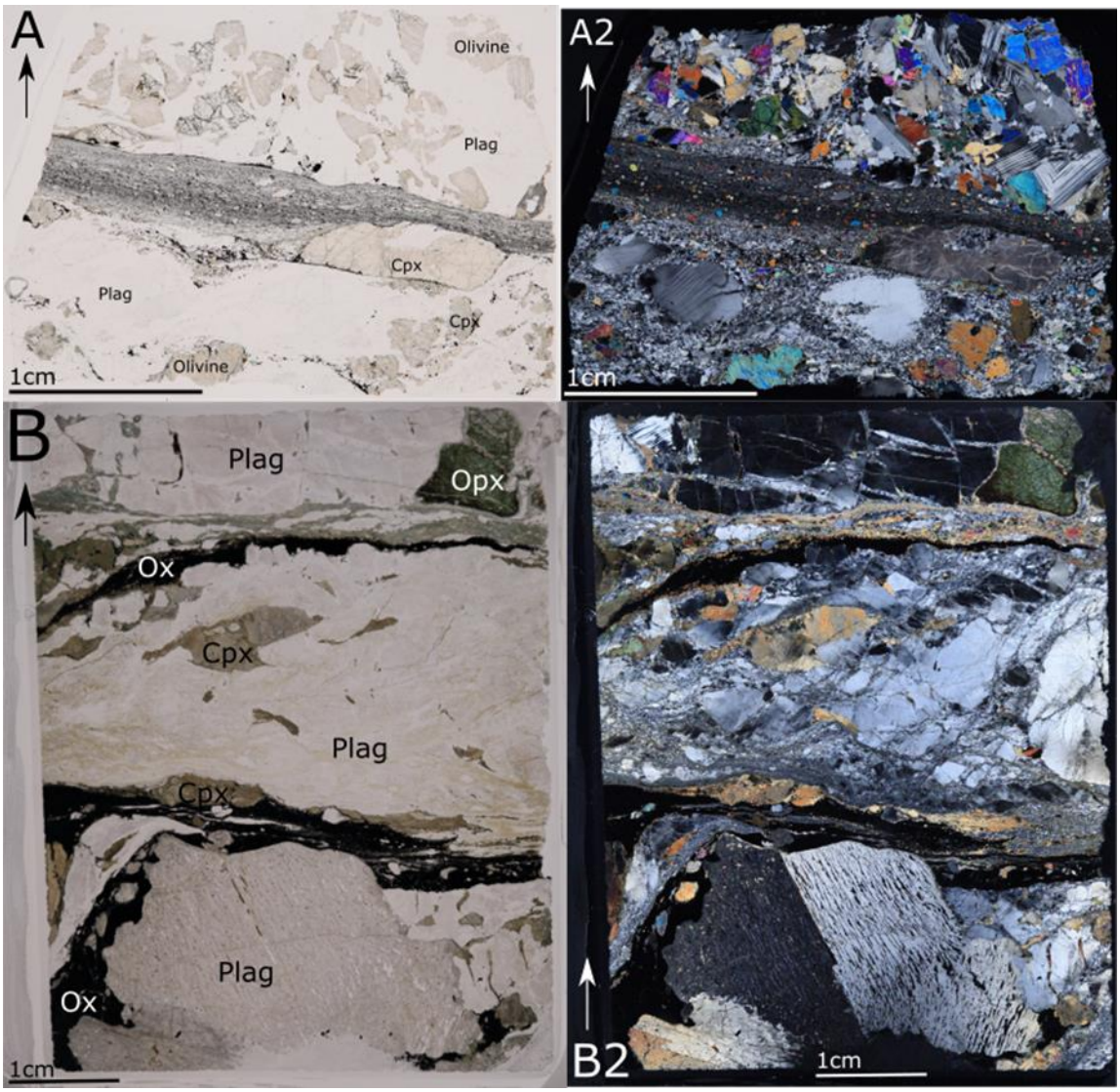

Figure 6.2 Shear zones

The above thin sections have been chosen from IODP Hole U1473A to illustrate how Fe-Ti oxides can sometimes form linings along the outside of shear zones. The black/white arrows represent up core direction. A and A2 are the plain polar and crossed polar images respectively of thin section sample 360-U1473A-68R-6-TS-235 taken from a depth of 623.9mbsf within IODP Hole U1473A. B and B2 are the plain polar and cross polar images respectively of thin section sample 360-U1473A-3R-1-TS-3 taken from a depth of 13.59mbsf within IODP Hole U1473A.

6.1.2 Olivine, Fe-Ti oxides and CPF intensity

As for why olivine would show a positive correlation with CPF intensity within the subpopulation, the relationship between the concentration of olivine and Fe-Ti oxides must be considered. Throughout all three holes examined in this study, there is a reverse relationship between Fe-Ti oxide concentration and olivine concentration, i.e. where one would rise the other would fall and vice versa, which is related to how and when they form. Olivine is usually formed early in the fractionation process of magma bodies; this fractionation process occurs as a magma cools causing different minerals to form at different temperatures. This fractionation process creates more evolved magmas which over time become enriched in elements such as Fe (3+) and Ti which will later form Fe-Ti oxides within the cooled magma body. Models have shown that by the time Fe-Ti oxides appear on the liquidus, only up to 5% porosity is left (Clague et al., 1981; Juster et al., 1989). This would indicate that only up to 5% Fe-Ti oxides would be expected to be present in olivine gabbro and gabbro. Therefore, the more Fe-Ti oxide present in the sample, the more evolved the starting composition must have been or Fe-Ti rich liquids infiltrated the area, and olivine would have been on the liquidus for a short period of time or not at all.

The reason that olivine calculated as a positive correlation factor with CPF for the subpopulation test and as a negative correlation factor for the complete dataset test is twofold. This has to do with the lithology of the samples being tested, which is controlled by which population is being tested (i.e., everything or the subpopulation) and the amount of variation within the olivine content of samples that also exhibit deformation. When all a hole's data was being tested, the majority of the samples would be from olivine gabbro,

meaning more samples with olivine present. Because the olivine concentration is highly variable throughout the hole, there would be no apparent trend between olivine content and CPF intensity. However, the majority of the samples with high CPF intensity had low olivine content; this causes the negative correlation between olivine concentration and CPF intensity since there would be no trend between the two variables. When the subpopulation of a hole was being tested, i.e., only samples with 5% or more Fe-Ti oxides, the principle lithology of these samples would be a Fe-Ti bearing gabbro. This means that there would be higher concentrations of Fe-Ti oxides present than there was of olivine. This lithologic difference removes the variability of the olivine (i.e., all samples had either low olivine or no olivine present), which leads to the positive correlation between Fe-Ti oxides, olivine, and CPF intensity. The main cause of this is the inherent susceptibility of the weaker Fe-Ti oxides to deformation compared to olivine.

6.1.3 CPF intensity and Depth

In both IODP Hole U1473A and ODP Hole 735B, there was more variation with respect to the CPF intensity values. These variations were within general trends of overall increase and then overall decrease of the average CPF intensity, that cover several hundreds of meters within the core. These trends are depicted in Figure 3.1, created using thickness corrected, running average of the CPF intensity. Figure 3.1 also depicts how IODP Hole U1473A and ODP Hole 1105A have very similar deformation profiles in the first 150 meters, then around 200 meters IODP Hole U1473As' deformation profile begins to decrease. This decrease is not exhibited in ODP Hole 1105A, given that it is only 160 meters deep. Even in ODP Hole 735B, there is a general increase and decrease

in the deformation profile, sometimes covering several hundred meters of the core. The statistical results for CPF intensity by depth identified a positive correlation within ODP Hole 1105A and not within the other to holes; the reason for this is the hole's shallow depth. The cause of this positive correlation between depth and CPF intensity is the fact that ODP Hole 1105A was simply too shallow to exhibit the same amount of variation as the other two holes, and also too shallow to include the complete rise and fall of a zone of intensified deformation. Should ODP Hole 1105A be drilled to a deeper depth, it is possible that the continued deformation profile would show a general decrease in the overall deformation intensity just like IODP Hole U1473A and ODP Hole 735B, and lead to a negative correlation.

6.1.4 Grain size and its control on other variables

An interesting result of this study was that grain size potentially plays a role in the relationship between Fe-Ti oxide concentration and CPF intensity. Nearly half of each hole's samples with 5% or more Fe-Ti oxides were present within samples of the finer grain size for that respective hole. These finer grained samples also had the highest average CPF intensity of each respective hole. This is because of the convoluted relationship between the three variables: Fe-Ti oxide concentration, grain size and CPF intensity. As this study has shown higher Fe-Ti oxide content within a sample tends to correlate with higher CPF intensities, and higher CPF intensities tend to correlate with samples of finer grain sizes. This is important because of how the crystal-plastic deformation is facilitated within Atlantis Bank. The crystal-plastic deformation process at Atlantis Bank occurs by recrystallization which leads to a smaller grain size as CPF intensity increases.

6.1.5 Implications for OCC development

As stated by John and Cheadle (2010), and shown in the Fe-Ti oxide concentration and CPF intensity results from ODP Hole 735B, Fe-Ti oxides can facilitate the localization of strain from detachments faults, like the one at Atlantis Bank. This type of strain localization caused by the detachment shear zone is observed in ODP Hole 735B on the deformation profile created by the Shipboard Scientific Party (1999), where the deformation intensity is very high at the surface of the hole then tapers off with depth. This is also echoed by this study's dataset for ODP Hole 735B, which exhibits the increased Fe-Ti oxide concentration correlated with increased CPF values at the seafloor which then tapers off with depth. This indicates that the concentration of Fe-Ti oxides near the detachment fault may facilitate the continued evolution of an OCC by localizing strain and creating a net flow preferentially along these bands of Fe-Ti oxides.

Fe-Ti oxides are an important mechanism for continued crystal-plastic deformation at lower temperatures within OCCs like Atlantis Bank. The reason for this is that the principal mineral phase present within the crustal column that makes up Atlantis Bank is plagioclase that only deforms plastically at temperatures exceeding ~750°C when dry (Mehl and Hirth, 2008; John and Cheadle, 2010). This allows for a small temperature/depth window of mylonite development within OCCs like Atlantis Bank because the lower crust is exhumed and cooled from ~1200°C to 750°C along the detachment shear zone/fault relatively quickly (>~800°C/Ma over the first ~500,000 years (John et al., 2004)). However, mylonitic rocks are present throughout Atlantis Bank, so crystal-plastic deformation most likely continued well below the ~750°C threshold. Also, the presence of abundant Fe-Ti oxides (5% or more) and CPF down to

~850 mbsf, indicates that the strain was distributed throughout much of the footwall, not just along the detachment shear zone. There are a few ways this process can be accomplished at lower temperatures: 1) already present shear zones are much weaker than the rocks around them (Mehl and Hirth, 2008) and 2) the presence of weak mineral phases like Fe-Ti oxides can preferentially partition strain. Because the majority of samples used in this study exhibit a positive relationship between the concentration of Fe-Ti oxides and CPF intensity and grain size, it is very likely that deformation was accommodated by Fe-Ti oxide-rich zones between 750°C and the lower limit of ductile deformation in Fe-Ti oxides of ~400°C. Below this temperature brittle-plastic deformation mechanisms like dissolution-precipitation (amphibole) and reaction softening (chlorite) would have facilitated the majority of the strain within Atlantis Bank (Miranda and John, 2010).

CHAPTER VII Future Studies

7.1 Future Studies

The primary weakness of this study includes the anomalies and gaps within the data, most of which would be remediated by obtaining thin sections this study did not have access to. This study could also be fortified with aspects such as magnetic susceptibility (which should line up with the Fe-Ti oxide concentrations) and other factors such as brittle deformation intensities, concentrations of alteration states, and metamorphic grades of the shear zones. The next phase could include samples from future holes within Atlantis Bank or holes from other OCCs to ascertain if the relationships found by this study hold true for other OCCs. There have been studies done on Atlantis Massif, such as that by Schoolmeesters et al. (2012), that suggest the Fe-Ti oxide bearing gabbros of Atlantis Massif have affected its cooling history; there was also some lithologic work done to show where these Fe-Ti oxide gabbros occur within the hole. This is important because temperature plays a very important role in crystal-plastic deformation. If the future studies find that there are different relationships present at the other OCCs, another study could look into if an OCC's location could have anything to do with the relationship present based on ridge type or magma composition, and rate of spreading.

CHAPTER VIII Conclusion

8.1 Conclusion

This study is the first to quantify the concentration of Fe-Ti oxides across a wide sample suite and to test the statistical significance of the relationship between Fe-Ti oxides and CPF intensity. This study confirms statements from previous studies of Atlantis Bank and other OCCs on the positive correlation between Fe-Ti oxides and CPF intensity rank based on the samples used from IODP Hole U1473A and ODP Holes 735B and 1105A. This study demonstrated that the Fe-Ti oxide concentrations in Atlantis Bank range from 0.00% to as high as 26.78%. Previous studies have used anecdotal evidence and inferences to make this prediction. Based on the analysis of the data from all three holes, there is a trend that samples with an Fe-Ti oxide concentration of 5% or more have a corresponding CPF intensity of 2 or more out of 5. While this trend was not a perfect fit, there was a discernable positive correlation between CPF intensity and Fe-Ti oxide concentration based on statistical analysis, and ~90% of the samples with Fe-Ti oxides exhibited some form of crystal-plastic deformation. These data indicate that while the Fe-Ti oxides were not completely controlling the CPF intensity (based on the factors used in this study), it was the only constant positive correlation between them. Another interesting result of this study is that grain size might also play a role in the relationship between Fe-Ti oxides and CPF intensity; and that where there is a high concentration of Fe-Ti oxides, there is a corresponding lack of olivine. The other interesting idea gleaned from the statistical analysis is that time might play a role in this relationship. IODP Hole U1473A and ODP Hole 1105A are from a younger portion of Atlantis Bank's structure, are from the middle of the complex, and had relatively equal correlation factors of 0.12

and 0.1, respectively. Whereas ODP Hole 735B is from an older portion of Atlantis Bank, along the western margin of the complexes structure, and has a correlation factor of 0.24. Results indicate that Fe-Ti oxides are integral in the formation of an oceanic core complex and play a significant role in the continuation and progression of crystal-plastic deformation in the footwall of oceanic core complexes. This study also begs the question if this relationship is something specific to Atlantis Bank along the Southwest Indian Ridge or is it present in other OCCs such as Atlantis Massif and Kane Mega Mullion along the Mid-Atlantic Ridge?

```
############
#load libraries
############
library(car)
library(corrplot) # We'll use corrplot later on in this example too.
library(visreg) # This library will allow us to show multivariate graphs.
library(rgl)
library(knitr)
library(scatterplot3d)
library(Hmisc)
####
#making citations for basic R
####
citation()
####
#making citations for the packages
####
citation("car")
citation("corrplot")
citation("visreg")
citation("rgl")
citation("knitr")
citation("scatterplot3d")
citation("Hmisc")
##########
##setting directory for excel files
##########
getwd()
##########
##read in my data csv file
##change the file name as needed
##########
alldata<-read.csv("735B_subpop.csv",header=T)
names(alldata)
##########
##create a subset of the data
##########
stats_data2<-subset(alldata,select=-c(Label))
summary(stats_data2)
##########
#plotting the data from stats_data2
```

```
##########
plot(stats_data2,pch=20,col="red",main="Matrix Scatterplot of % Fe-Ti oxide, CPF
Intensity Rank, Top Depth and % Olivine")
##########
#center predictors
##########
names(stats_data2)
X..oxide.c=scale(stats_data2$X..oxide,center=TRUE,scale=FALSE)
CPF.intensity.rank..0.5..c=scale(stats_data2$CPF.intensity.rank..0.5.,center=TRUE,scale
=FALSE)
Top.Depth..m..c=scale(stats_data2$Top.Depth..m.,center=TRUE,scale=FALSE)
Grain.size.c=scale(stats_data2$Grain.size,center=TRUE,scale=FALSE)
Olivine.....c=scale(stats_data2$Olivine....,center=TRUE,scale=FALSE)
#bind these new variables into stats_data2 and display a summary
new.c.vars=cbind(X..oxide.c,CPF.intensity.rank..0.5..c,Top.Depth..m..c,Grain.size.c,Oliv
ine.....c)
stats_data2=cbind(stats_data2,new.c.vars)
names(stats_data2)=c("X..oxide.c","CPF.intensity.rank..0.5..c","Top.Depth..m..c","Grain.
size.c","Olivine.....c")
summary(stats_data2)
##########
#create the linear model and display a summary
##########
mod1=lm(CPF.intensity.rank..0.5..c~X..oxide.c+Top.Depth..m..c+Grain.size.c
+Olivine.....c,data=stats_data2)
summary(mod1)
###########
#Plot a correlation graph
###########
newdatacor=cor(stats_data2[1:5])
corrplot(newdatacor,method="number")
#############################################################
#############################################################
#############################################################
```

APPENDIX B – Datasets from all of the Holes

Datasets from all three Holes

	Brightness/Contrast Values		Threshold Values		Measured area (pixels)			CPF intensity rank	Top Depth	Olivine original	Grain size
Label	Low	High	Low	High	total area	output	% oxide	(0-5)	(m)	(%)	
360-U1473A-2R-1-W 120/121-TSB	0	160	0	45	7928245	986182	12.43884	3	10.7	20	coarsegrained
360-U1473A-2R-2-W 25/30-TSB	0	150	0	100	12251769	21040	0.17173	0	11.12	5	coarsegrained
360-U1473A-3R-1-W 79/85-TSB	0	150	0	12	10392169	575986	5.5425	3	13.59	12	coarsegrained
360-U1473A-3R-2-W 89/98-TSB	0	130	0	66	11867805	11066	0.093244	0	15.04	15	coarsegrained
360-U1473A-3R-4-W 40/42-TSB	0	170	0	100	8644120	24561	0.284135	0	17.43	15	coarsegrained
360-U1473A-3R-4-W 64/67-TSB	0	140	0	82	8413599	2413	0.02868	0	17.67		medium grained
360-U1473A-4R-1-W 68/73-TSB	0	100	0	38	11304587	3442	0.030448	0	23.08	2	medium grained
360-U1473A-4R-3-W 40/44-TSB	0	55	0	150	9849885	150645	1.531439	2	25.81	2	finegrained
360-U1473A-4R-3-W 114/117-TSB	0	130	0	75	7908856	1011	0.012783	2	26.55		finegrained
360-U1473A-4R-4-W 26/30-TSB							0.01	2	27.17	10	pegmatitic
360-U1473A-4R-4-W 127/130-TSB	0	80	0	140	10005546	118894	1.188281	4	28.18	1	medium grained
360-U1473A-5R-1-W 56/60-TSB							0.01	0.5	32.56	5	coarsegrained
360-U1473A-6R-3-W 52/54-TSB	0	120	0	60	8753099	256819	2.934035	1	45.12	11	finegrained
360-U1473A-6R-3-W 58/61-TSB	30	190	0	5	8822737	1297599	14.707	3	45.18	7	medium grained
360-U1473A-6R-3-W 95/97-TSB	60	124	0	70	9421453	145486	1.544	0	45.55	5	finegrained
360-U1473A-7R-1-W 131/134-TSB	0	164	0	40	9791697	1180	0.012	0.5	52.61	0.5	medium grained
360-U1473A-8R-3-W 21/27-TSB	0	100	0	63	11891528	11509	0.097	3	64.05	3	medium grained
360-U1473A-9R-2-W 44/48-TSB	0	108	0	34	9159363	1439	0.016	0	72.57		medium grained
360-U1473A-9R-2-W 141/145-TSB	0	85	0	100	9511567	77973	0.82	0	73.54	10	coarsegrained
360-U1473A-9R-4-W 51/54-TSB	0	100	0	77	9487791	708	0.007	4	75.63		finegrained
360-U1473A-9R-4-W 126/129-TSB	0	143	0	105	9240412	16111	0.174	4	76.38	1	medium grained
360-U1473A-9R-5-W 2/8-TSB	0	110	0	158	7857334	2537	0.032	2	76.58		medium grained
360-U1473A-9R-5-W 40/44-TSB	0	100	0	107	12008461	7872	0.066	0	76.96	5	coarsegrained
360-U1473A-9R-5-W 115/118-TSB	0	136	0	63	9894598	217183	2.197		77.71		finegrained
360-U1473A-10R-1-W 88/91-TSB	0	100	0	20	11200760	57968	3.446	4	81.28		medium grained
360-U1473A-10R-1-W 128/131-TSB	0	96	0	55	7713480	124480	1.614	4	81.68		medium grained
360-U1473A-10R-2-W 87/91-TSB	0	61	0	79	11321842	185262	1.725	0.5	82.65	2	coarsegrained
360-U1473A-10R-3-W 72/75-TSB	0	74	0	104	10186980	33539	0.329	0.5	83.59		coarsegrained
360-U1473A-11R-1-W 43/47-TSB	0	90	0	78	9818040	11863	0.121	4	90.53		medium grained
360-U1473A-11R-2-W 2/6-TSB	0	94	0	55	9124382	47706	0.523	3	91.61		medium grained
360-U1473A-11R-3-W 42/46-TSB	0	134	0	70	10926216	215062	2.089	4	93.46	8	medium grained
360-U1473A-11R-3-W 63/65-TSB	0	90	0	30	9149212	1010385	11.044	3	93.67	5	medium grained
360-U1473A-11R-3-W 111/117-TSB	0	80	0	82	11211842	29503	0.263	4	94.15		medium grained
360-U1473A-12R-1-W 0/3-TSB	?	?	?	?	?	?	0	3	99.8		medium grained
360-U1473A-12R-3-W 104/107-TSB	0	101	0	108	9814431	227517	2.318	3	103.76	6	medium grained
360-U1473A-12R-4-W 60/64-TSB	0	87	0	30	11629397	156222	1.343	3	104.82	2	medium grained
360-U1473A-13R-1-W 65/72-TSB	0	71	0	100	10692752	40996	0.383	0.5	110.15	16.8	medium grained
360-U1473A-13R-1-W 106/108-TSB	0	100	0	70	9111168	68379	0.75	1	110.56	10	coarsegrained
360-U1473A-13R-4-W 57/60-TSB	0	102	0	86	10959634	2485	0.023	0	113.88		coarsegrained
360-U1473A-14R-1-W 27/28-TSB	0	93	0	144	11729983	15964	0.136	4	119.47	12	medium grained
360-U1473A-14R-4-W 134/136-TSB	0	96	0	60	10537781	39872	0.378	1.5	124.87	5	medium grained
360-U1473A-14R-5-W 80/83-TSB	0	105	0	66	8738223	23	0.000263	1.5	125.83		medium grained
360-U1473A-15R-1-W 27/32-TSB	0	154	0	34	9648650	31361	0.325	3	129.17	13	medium grained
360-U1473A-15R-1-W 69/73-TSB	0	97	0	145	8869978	11091	0.125	4	129.59	0.5	finegrained
360-U1473A-15R-2-W 21/23-TSB	0	100	0	42	9588154	0	0	0	130.61		coarsegrained
360-U1473A-15R-2-W 47/50-TSB	0	104	0	127	9162507	2975	0.032	4	130.87		finegrained
360-U1473A-15R-3-W 5/9-TSB	0	124	0	64	10265355	13357	0.13	3	131.65	10	medium grained
360-U1473A-15R-3-W 60/62-TSB	0	90	0	100	10308372	263168	2.553	3	132.2	1	medium grained
360-U1473A-15R-3-W 119/123-TSB	0	94	0	56	11155684	35904	0.322	3	132.79	10.5	medium grained
360-U1473A-16R-1-W 34/38-TSB	0	52	0	34	10476846	30657	0.292	2	138.94	5	medium grained
360-U1473A-16R-2-W 74/78-TSB	0	105	0	60	10809786	52310	0.484	4	140.84	5	finegrained
360-U1473A-16R-2-W 89/93-TSB	0	100	0	110	8835870	78587	0.889	2	140.99	5	finegrained
360-U1473A-16R-4-W 129/135-TSB	0	70	0	72	11641855	107791	0.926	4	144.35	5	medium grained
360-U1473A-16R-5-W 24/28-TSB	0	100	0	93	8434921	48697	0.577	4	144.75		medium grained
360-U1473A-16R-6-W 130/137-TSB	0	130	0	83	12435301	461982	3.715	3	147.23		medium grained
360-U1473A-17R-2-W 102/106-TSB	0	117	0	100	9816193	267034	2.72	2	150.78	14	finegrained
360-U1473A-17R-4-W 44/48-TSB	?	?	?	?	?	?	0	3	153.01	2	medium grained
360-U1473A-18R-1-W 108/113-TSB	0	144	0	120	10360074	24730	0.239	2	159.08	15	finegrained
360-U1473A-18R-2-W 58/61-TSB	0	85	0	78	9851450	103166	1.037	3	159.92	14	medium grained
360-U1473A-19R-1-W 55/59-TSB	0	128	0	88	10195458	42606	0.418	4	168.25	5	medium grained
360-U1473A-19R-2-W 133/137-TSB	0	130	0	90	7881639	15562	0.197	4	170.54		finegrained
360-U1473A-20R-1-W 129/135-TSB	0	120	0	76	11538581	78395	0.679	4	178.69	1	medium grained
360-U1473A-20R-2-W 9/12-TSB	0	200	0	105	10186850	58217	0.572	4	178.95	8	finegrained
360-U1473A-20R-2-W 68/74-TSB	0	109	0	154	12351868	108068	0.875	4	179.54	16	coarsegrained
360-U1473A-21R-1-W 12/15-TSB	0	213	0	47	10205999	1161982	11.38528	4	180.22		medium grained
360-U1473A-21R-2-W 22/26-TSB	0	165	0	70	10268716	35976	0.35	3	181.7	8	medium grained
360-U1473A-22R-1-W 35/38-TSB	0	147	0	101	10810602	13858	0.128	3	187.45		medium grained
360-U1473A-22R-1-W 50/53-TSB	0	120	0	114	9874792	3608	0.037	1.5	187.6		medium grained
360-U1473A-22R-2-W 32/34-TSB	0	145	0	109	9792873	98200	1.003	3	188.85	8	medium grained
360-U1473A-23R-1-W 83/90-TSB	0	80	0	112	12056601	12397	0.103	3	197.63		medium grained
360-U1473A-23R-2-W 71/73-TSB	0	150	0	141	9380284	283077	3.018	4	199.01		finegrained
360-U1473A-23R-2-W 106/110-TSB	0	114	0	57	11638244	40714	0.348	1	199.36	4	medium grained
360-U1473A-23R-3-W 3/6-TSB	0	120	0	74	8737833	1794	0.021	0.5	199.8	2	coarsegrained
360-U1473A-23R-3-W 41/45-TSB	0	170	0	139	11183544	111824	0.999	2	200.18	12	coarsegrained
360-U1473A-23R-3-W 52/55-TSB	0	138	0	65	8524244	1976	0.023	4	200.29	5	medium grained
360-U1473A-23R-3-W 65/72-TSB	0	186	0	156	12632588	58739	0.465	4	200.42	3	medium grained
360-U1473A-24R-1-W 54/57-TSB	0	125	0	94	10292584	18560	0.18	4	207.04		finegrained
360-U1473A-24R-1-W 66/68-TSB	0	140	0	148	8457414	14118	0.167	4	207.16		finegrained
360-U1473A-24R-2-W 96/100-TSB	0	122	0	71	9054291	156155	1.725	3	208.96	0.2	medium grained
360-U1473A-24R-3-W 47/50-TSB	0	100	0	152	8160987	34429	0.422	4	209.86		medium grained
360-U1473A-25R-1-W 5/8-TSB	0	130	0	90	9291500	26158	0.282	4	216.25		finegrained
360-U1473A-25R-1-W 74/77-TSB	0	170	0	110	10278379	31654	0.308	5	216.94	2	medium grained
360-U1473A-25R-1-W 84/90-TSB	0	138	0	95	11852584	60246	0.508	3	217.04	3	medium grained
360-U1473A-25R-2-W 39/42-TSB	0	110	0	155	9075516	45987	0.507	4	218.09	0.1	finegrained
360-U1473A-25R-2-W 53/55-TSB	?	?	?	?	?	?	0	4	218.23		finegrained
360-U1473A-26R-2-W 101/104-TSB	0	70	0	148	10243860	139300	1.36	4	228.4	1	finegrained
360-U1473A-26R-3-W 52/57-TSB	0	122	0	138	9201286	69187	0.752	1	229.41	7	coarsegrained
360-U1473A-27R-1-W 111/117-TSB	0	107	0	160	11186554	89521	0.8	3	236.71		medium grained
360-U1473A-27R-2-W 38/42-TSB	0	110	0	141	9095274	22283	0.245	3	237.18		medium grained
360-U1473A-28R-1-W 68/71-TSB	0	55	0	104	9998689	20507	0.218	2	245.98		finegrained
360-U1473A-28R-3-W 41/44-TSB	0	172	0	103	8938184	14891	0.167	4	248.65		medium grained
360-U1473A-28R-5-W 9/12-TSB	0	146	0	133	9196808	65983	0.717	0.5	251.24	15	coarsegrained
360-U1473A-29R-1-W 32/36-TSB	0	130	0	92	9397453	53389	0.568	0.5	255.32	3	coarsegrained
360-U1473A-29R-1-W 69/73-TSB	0	111	0	50	9264619	1740	0.019	0	255.69		medium grained
360-U1473A-29R-2-W 32/36-TSB	0	122	0	32	10693559	8864	0.083	0	256.82		medium grained
360-U1473A-29R-3-W 48/51-TSB	0	113	0	113	8949738	7432	0.083	0.5	258.39		coarsegrained
360-U1473A-29R-4-W 112/116-TSB	0	110	0	45	8896529	1661	0.019	0.5	260.46		medium grained
360-U1473A-30R-1-W 86/90-TSB	0	100	0	82	8735933	725161	8.244	3	265.56		medium grained
360-U1473A-30R-3-W 40/44-TSB	0	88	0	43	10570121	15978	0.151	2	267.95	5	medium grained
360-U1473A-30R-5-W 4/8-TSB	0	120	0	102	10230509	57397	0.561	2	270.59	15	coarsegrained
360-U1473A-30R-5-W 27/31-TSB	0	168	0	110	10515800	39079	0.372	1.5	270.82	2	medium grained

360-U1473A-31R-1-W 106/108-TSB	0	100	0	30	10367283	1316	0.013	1	275.46	3	medium grained
360-U1473A-31R-2-W 118/122-TSB	0	166	0	95	10385615	75299	0.725	1	277.08	2	medium grained
360-U1473A-31R-3-W 6/10-TSB	0	130	0	110	8415145	71292	0.847	4	277.46		medium grained
360-U1473A-32R-2-W 85/89-TSB	0	152	0	124	10301909	65575	0.637	1.5	286.22	3	medium grained
360-U1473A-32R-2-W 143/147-TSB	0	160	0	139	10309932	208164	2.019	4	286.8	25	medium grained
360-U1473A-32R-4-W 43/46-TSB	0	110	0	50	9428485	2814	0.03	0.5	288.75	10	coarse grained
360-U1473A-32R-5-W 131/136-TSB	0	150	0	58	9276020	2335	0.025	4	291.13	5	fine grained
360-U1473A-32R-6-W 38/43-TSB	0	138	0	46	10848507	1695	0.016	2	291.7	10	medium grained
360-U1473A-33R-1-W 3/7-TSB	0	106	0	46	9935215	39289	0.393	1	293.83	15	coarse grained
360-U1473A-33R-2-W 30/33-TSB	0	138	0	74	10774393	7999	0.074	0	295.4	5	medium grained
360-U1473A-33R-3-W 33/38-TSB	0	122	0	31	10237898	2609	0.025	3	296.75	8	coarse grained
360-U1473A-33R-3-W 94/97-TSB	0	100	0	80	8844762	16753	0.189	0.5	297.36	10	coarse grained
360-U1473A-33R-4-W 11/15-TSB	0	144	0	132	9331397	55549	0.595	0.5	297.67	8	medium grained
360-U1473A-33R-5-W 55/58-TSB	0	146	0	64	9623120	5830	0.061	0.5	299.5		coarse grained
360-U1473A-34R-5-W 88/91-TSB	0	136	0	94	9551869	5959	0.062	1	309.06	15	fine grained
360-U1473A-34R-5-W 98/101-TSB	0	168	0	129	9330660	119438	1.28	3	309.16	9	medium grained
360-U1473A-35R-1-W 55/58-TSB	0	160	0	80	10160882	14506	0.143	4	313.75	5	medium grained
360-U1473A-36R-3-W 1/6-TSB	0	70	0	66	9101677	16269	0.179	3	325.82	17	medium grained
360-U1473A-37R-2-W 86/90-TSB	0	150	0	122	10068211	41260	0.41	3	334.96	0.5	medium grained
360-U1473A-37R-3-W 45/49-TSB	0	80	0	70	9230636	11707	0.127	3	336.05	5	medium grained
360-U1473A-37R-4-W 133/137-TSB	0	180	0	84	9146266	26481	0.29	3	338.33	5	medium grained
360-U1473A-38R-4-W 72/76-TSB	0	140	0	100	7876161	13236	0.168	3	346.82	20	coarse grained
360-U1473A-38R-4-W 101/105-TSB	0	155	0	150	9315486	164665	1.661	4	347.11	4	medium grained
360-U1473A-39R-4-W 3/8-TSB	0	116	0	70	11105758	311371	2.804	4	355.98	10	medium grained
360-U1473A-39R-4-W 15/18-TSB	0	100	0	90	10700650	30100	0.281	3	356.1	9	coarse grained
360-U1473A-39R-5-W 11/14-TSB	0	110	0	46	10700460	340628	3.183	0.5	357.48		coarse grained
360-U1473A-39R-5-W 125/128-TSB	0	110	0	100	9032706	21460	0.238	0	358.62		medium grained
360-U1473A-39R-6-W 7/11-TSB	0	120	0	74	9781138	105047	1.074	1	358.94	12	coarse grained
360-U1473A-40R-1-W 69/73-TSB	0	106	0	114	10090627	26770	0.265	3	362.39	5	medium grained
360-U1473A-40R-1-W 121/128-TSB	0	160	0	96	11261286	33086	0.294	4	362.91	20	medium grained
360-U1473A-40R-2-W 3/10-TSB	0	166	0	96	10859210	41104	0.379	5	363.09	8	medium grained
360-U1473A-41R-2-W 24/28-TSB	0	125	0	95	10503221	850295	8.096	4	373.09	1	medium grained
360-U1473A-41R-2-W 39/43-TSB	?	?	?	?	?	?	0	1	373.24	2	coarse grained
360-U1473A-41R-3-W 73/76-TSB	0	155	0	71	9482180	48128	0.508	1	375	3	medium grained
360-U1473A-41R-3-W 112/115-TSB	0	180	0	30	10852966	38268	0.353	1.5	375.39	18	coarse grained
360-U1473A-41R-4-W 92/96-TSB	0	140	0	100	9818314	22241	0.227	1	376.55	5	medium grained
360-U1473A-42R-1-W 47/49-TSB	0	130	0	120	10163820	270306	2.659	0	381.57	5	fine grained
360-U1473A-42R-2-W 30/33-TSB	0	105	0	69	11121253	34262	0.308	0	382.9	5	fine grained
360-U1473A-42R-2-W 79/85-TSB	0	100	0	62	10181094	12670	0.124	1	383.39	5	medium grained
360-U1473A-42R-3-W 4/8-TSB	0	136	0	84	10184303	20311	0.199	0.5	383.98	17	coarse grained
360-U1473A-42R-4-W 42/46-TSB	0	140	0	140	9097183	28214	0.31	1	385.74	10	medium grained
360-U1473A-43R-1-W 35/37-TSB	0	120	0	82	10082326	8420	0.084	2	391.15	1	coarse grained
360-U1473A-43R-2-W 42/46-TSB	0	150	0	70	9355960	33044	0.392	3	392.5	15	coarse grained
360-U1473A-43R-5-W 124/127-TSB	0	110	0	105	9993865	299434	2.996	1.5	397.04		coarse grained
360-U1473A-43R-6-W 56/60-TSB	0	150	0	85	10542740	33520	0.318	1	397.65	2	medium grained
360-U1473A-44R-1-W 8/12-TSB	0	100	0	75	10607502	28471	0.268	3	400.58	5	medium grained
360-U1473A-44R-1-W 85/89-TSB	0	100	0	130	10055562	29911	0.297	2	401.35	5	medium grained
360-U1473A-44R-2-W 117/120-TSB	0	140	0	47	11068803	577	0.005	1	403.13		medium grained
360-U1473A-44R-4-W 65/69-TSB	0	120	0	110	10589061	61655	0.582	5	405.52	5	medium grained
360-U1473A-44R-4-W 93/97-TSB	0	130	0	130	9942327	87196	0.877	0.5	405.8	25	medium grained
360-U1473A-44R-5-W 6/12-TSB	0	125	0	68	10610929	22203	0.209	1	406.43	28	coarse grained
360-U1473A-45M-1-W 44/47-TSB	0	85	0	65	9724323	18339	0.189	2	410.64	10	medium grained
360-U1473A-45M-1-W 83/93-TSB	0	140	0	164	11586062	66738	0.576	1	411.09	7	medium grained
360-U1473A-46R-1-W 33/36-TSB	0	150	0	100	9832186	58770	0.598	2	411.13	15	medium grained
360-U1473A-46R-1-W 139/142-TSB	0	65	0	100	7972079	1899	0.024	3	412.19	12	medium grained
360-U1473A-46R-2-W 76/80-TSB	0	134	0	60	10390523	3534	0.034	1.5	413.06	7	medium grained
360-U1473A-46R-3-W 32/35-TSB	0	80	0	20	9792808	6	0.01	3	414.12	10	coarse grained
360-U1473A-47R-1-W 21/26-TSB	0	90	0	42	11373767	916678	8.06	3	420.71		medium grained
360-U1473A-47R-1-W 36/42-TSB	0	140	0	120	10114973	118168	1.168	3	420.86		medium grained
360-U1473A-47R-1-W 115/119-TSB	0	136	0	63	9359403	55009	0.588	4	421.65		medium grained
360-U1473A-47R-2-W 110/114-TSB	0	145	0	112	8270122	37613	0.455	1	423.1	2	coarse grained
360-U1473A-47R-2-W 142/149-TSB	0	165	0	152	11026686	146752	1.331		423.42	13	medium grained
360-U1473A-47R-3-W 24/27-TSB	0	145	0	110	9444145	317687	3.364	4	423.74	5	medium grained
360-U1473A-47R-3-W 65/70-TSB	0	185	0	170	10153206	24077	0.237	3	424.15	15	medium grained
360-U1473A-47R-3-W 108/110-TSB	0	136	0	36	9352433	19880	0.213	1	424.58	5	medium grained
360-U1473A-48R-1-W 16/20-TSB	0	125	0	72	9009314	19704	0.219	0.5	430.36	3	medium grained
360-U1473A-48R-2-W 19/21-TSB	0	115	0	84	8683233	2981	0.034	3	431.89		medium grained
360-U1473A-48R-3-W 79/82-TSB	0	136	0	115	10623163	34765	0.327	0.5	433.99	9	coarse grained
360-U1473A-49R-1-W 62/64-TSB	0	145	0	135	9909714	27362	0.276	0.5	440.52	5	coarse grained
360-U1473A-49R-1-W 119/122-TSB	0	136	0	106	9864061	7849	0.08	1.5	441.09	8	medium grained
360-U1473A-50R-1-W 113/116-TSB	0	155	0	155	9600201	78735	0.82	3	450.73	5	medium grained
360-U1473A-50R-2-W 47/51-TSB	0	125	0	103	8769738	15927	0.182	1	451.57	8	medium grained
360-U1473A-50R-2-W 83/85-TSB	0	95	0	49	8540579	13093	0.153	0	451.93		coarse grained
360-U1473A-51R-1-W 47/50-TSB	0	105	0	56	10578817	1862	0.018	1	459.77	12	coarse grained
360-U1473A-51R-1-W 50/55-TSB	0	175	0	100	113151652	7858	0.069	3	459.8	30	medium grained
360-U1473A-51R-1-W 91/93-TSB	0	55	0	54	9931148	122195	1.223	1	460.21	10	medium grained
360-U1473A-51R-1-W 97/100-TSB	0	115	0	35	8348176	34562	0.386	0	460.27	5	medium grained
360-U1473A-51R-1-W 100/106-TSB	0	85	0	105	11197123	33013	0.295	0.5	460.3	7	coarse grained
360-U1473A-51R-1-W 142/147-TSB	0	75	0	37	11262164	6417	0.057	0	460.72	15	coarse grained
360-U1473A-51R-2-W 7/10-TSB	0	105	0	75	9143310	29555	0.323	0	460.87	1	medium grained
360-U1473A-51R-2-W 91/95-TSB	0	75	0	44	9818841	5912	0.06	1	461.71	5	coarse grained
360-U1473A-51R-3-W 144/147-TSB	0	95	0	46	8913548	1267	0.014	0	463.68	25	coarse grained
360-U1473A-51R-4-W 87/91-TSB	0	115	0	50	9157022	7398	0.081	0.5	464.61	8	coarse grained
360-U1473A-52R-1-W 2/4-TSB	0	65	0	53	10200185	56197	0.551	0	469.02	21	coarse grained
360-U1473A-52R-1-W 40/44-TSB	0	125	0	44	9834713	12262	0.125	0	469.4	12	coarse grained
360-U1473A-57R-1-W 32/35-TSB	0	145	0	108	10361193	17129	0.165	3	519.52	7	medium grained
360-U1473A-58R-2-W 12/16-TSB	0	185	0	145	9539506	63902	0.664	1	520.79	15	coarse grained
360-U1473A-58R-2-W 95/102-TSB	0	155	0	118	11646388	82441	0.708	3	521.62	12	coarse grained
360-U1473A-58R-3-W 101/104-TSB	0	175	0	130	11600322	140186	1.208	1	523.15	15	fine grained
360-U1473A-58R-4-W 111/114-TSB	0	165	0	95	10268970	7077	0.069	4	524.59	6	medium grained
360-U1473A-58R-5-W 28/31-TSB	0	155	0	113	9970775	36705	0.368		525.26		medium grained
360-U1473A-58R-8-W 71/77-TSB	0	175	0	84	11281963	65256	0.578	5	529.64	11	coarse grained
360-U1473A-59R-1-W 68/71-TSB	0	175	0	105	10852871	25896	0.25	1	529.88	6	coarse grained
360-U1473A-59R-2-W 101/104-TSB	0	165	0	95	8503222	54255	0.638		531.61		medium grained
360-U1473A-59R-3-W 87/90-TSB	0	155	0	127	10817981	15212	0.141	1	532.75	5	medium grained
360-U1473A-59R-4-W 57/60-TSB	0	185	0	135	8730575	28698	0.329	2	533.78	7	medium grained
360-U1473A-59R-4-W 95/98-TSB	0	145	0	145	10978329	725	0.007		534.16	10	fine grained
360-U1473A-60R-1-W 17/19-TSB	0	215	0	90	9173092	5227	0.057	2	538.97	12	coarse grained
360-U1473A-60R-2-W 77/80-TSB	0	145	0	125	10755386	86655	0.806	1	540.62	13	medium grained
360-U1473A-60R-3-W 132/136-TSB	0	165	0	145	11510641	4072	0.035	4	542.45		fine grained
360-U1473A-61R-1-W 31/34-TSB	0	175	0	109	9391674	19890	0.212	2	548.71	3	coarse grained
360-U1473A-61R-3-W 100/103-TSB	0	165	0	135	12379738	81172	0.656	1	551.83	10	coarse grained
360-U1473A-61R-4-W 31/35-TSB	0	155	0	48	12392716	127972	1.038	3	552.35	10	medium grained

360-U1473A-62R-1-W 79/84-TSB	0	135	0	155	12072465	87777	0.727	1	558.89	1	coarse grained
360-U1473A-62R-3-W 114/118-TSB	0	145	0	80	11593928	96259	0.83	0	561.51	12	coarse grained
360-U1473A-62R-4-W 129/132-TSB	0	135	0	95	10277738	4337	0.042	3	563.16		medium grained
360-U1473A-62R-5-W 68/70-TSB	0	125	0	105	9090626	6661	0.073	1	564.05		medium grained
360-U1473A-62R-6-W 22/25-TSB	0	145	0	105	9165372	9531	0.104	1	565.09	7	fine grained
360-U1473A-63R-1-W 61/64-TSB	0	145	0	85	10741708	26631	0.248	2	568.41		medium grained
360-U1473A-63R-2-W 110/112-TSB	0	145	0	85	9400314	63294	0.673	2	570.32	8	coarse grained
360-U1473A-64R-2-W 47/51-TSB	0	125	0	135	11112063	14574	0.131	2	578.15	7.5	medium grained
360-U1473A-64R-2-W 110/114-TSB	0	165	0	105	10987113	435136	3.96	1.5	578.78		medium grained
360-U1473A-64R-8-W 11/14-TSB	0	155	0	117	10528948	31865	0.303	1	584.37	7	medium grained
360-U1473A-65R-1-W 123/129-TSB	0	165	0	115	11046589	89022	0.806		588.43	6	coarse grained
360-U1473A-65R-2-W 41/44-TSB	0	175	0	95	8275190	32119	0.388		589.09	10	coarse grained
360-U1473A-65R-3-W 65/70-TSB	0	155	0	45	11985713	10920	0.091	3	590.66	6	medium grained
360-U1473A-65R-5-W 2/4-TSB	0	145	0	125	10103050	42733	0.423	1	593.09	9	fine grained
360-U1473A-65R-5-W 5/9-TSB	0	165	0	144	10063131	104129	1.035	0.5	593.06	5	medium grained
360-U1473A-65R-5-W 17/20-TSB	0	145	0	125	9471814	135280	1.428	0.5	593.18	17	coarse grained
360-U1473A-65R-5-W 30/33-TSB	0	135	0	132	8857730	77465	0.875	0.5	593.31	12	medium grained
360-U1473A-65R-5-W 51/54-TSB	0	155	0	85	10114392	55450	0.548	1	593.52	9	coarse grained
360-U1473A-65R-5-W 94/98-TSB	0	145	0	175	9089622	123798	1.37	0	593.95	13	fine grained
360-U1473A-65R-5-W 102/105-TSB	0	165	0	115	10887630	103533	0.951	1	594.03	12	coarse grained
360-U1473A-65R-5-W 112/115-TSB	0	145	0	105	10551997	99405	0.942	1	594.13	11	medium grained
360-U1473A-65R-7-W 40/44-TSB	0	125	0	57	11419003	426134	3.749	4	596.22	5	medium grained
360-U1473A-66R-1-W 81/85-TSB	0	125	0	105	10544551.7	24383	0.231	0.5	597.71	16	fine grained
360-U1473A-66R-4-W 139/142-TSB	0	145	0	90	10374243	206898	2.014	4	602.75		medium grained
360-U1473A-66R-7-W 12/18-TSB	0	165	0	145	11289069	47033	0.417		605.66	32	coarse grained
360-U1473A-67R-1-W 124/127-TSB	0	185	0	145	11391349	35143	0.309		607.84	5	medium grained
360-U1473A-67R-3-W 23/26-TSB	0	185	0	115	12273916	3305	0.027		609.47		coarse grained
360-U1473A-67R-3-W 41/44-TSB	0	175	0	95	11101575	22882	0.206		609.65	7	coarse grained
360-U1473A-67R-6-W 34/38-TSB	0	155	0	132	11345731	3230	0.028		613.72	2	coarse grained
360-U1473A-67R-7-W 70/74-TSB	0	195	0	95	11885956	41539	0.349	2	615.51	6	coarse grained
360-U1473A-67R-7-W 74/77-TSB	0	175	0	115	11972388	125709	1.05		615.55	9	coarse grained
360-U1473A-68R-2-W 74/78-TSB	0	165	0	125	12344837	287639	2.33		618.37	16	coarse grained
360-U1473A-68R-3-W 79/83-TSB	0	165	0	118	12267913	34878	0.284	1	619.9	5	medium grained
360-U1473A-68R-6-W 58/60-TSB	0	205	0	114	9092578	133850	1.473	4	623.9	12	medium grained
360-U1473A-68R-6-W 107/111-TSB	0	165	0	75	11003249	141278	1.284		624.39	5	coarse grained
360-U1473A-68R-7-W 51/55-TSB	0	145	0	135	11126144	84647	0.761	2	625.15	12	medium grained
360-U1473A-69R-1-W 109/112-TSB	0	165	0	85	11353141	53602	0.473		627.09	9	coarse grained
360-U1473A-69R-4-W 107/111-TSB	0	155	0	145	10160760	53881	0.53	3	630.91	5	medium grained
360-U1473A-69R-5-W 41/43-TSB	0	195	0	103	8253971	39604	0.48	1	631.75	5	fine grained
360-U1473A-69R-6-W 68/74-TSB	0	205	0	53	11137523	49000	0.44	5	632.02	6	medium grained
360-U1473A-69R-6-W 132/136-TSB	0	155	0	105	10014473	45936	0.459	3	633.95	13	medium grained
360-U1473A-70R-1-W 52/55-TSB	0	165	0	105	8852217	22491	0.254	1	636.22	8	coarse grained
360-U1473A-70R-1-W 71/75-TSB	0	175	0	105	12194772	37842	0.31		636.41	10	medium grained
360-U1473A-70R-3-W 70/73-TSB	0	165	0	95	8973094	211430	2.356		639.26		coarse grained
360-U1473A-70R-4-W 27/30-TSB	0	145	0	125	10885549	3602	0.033	1	639.79	15	medium grained
360-U1473A-70R-4-W 93/95-TSB	0	165	0	115	11017332	27506	0.25		640.45	12	coarse grained
360-U1473A-70R-6-W 0/4-TSB	0	145	0	125	11433243	20086	0.176	1	642	5	medium grained
360-U1473A-70R-6-W 84/87-TSB	0	145	0	95	10511153	107031	1.018	1	642.84	10	medium grained
360-U1473A-71R-1-W 67/70-TSB	0	165	0	135	11038624	79699	0.722	1	646.07	8	medium grained
360-U1473A-71R-1-W 83/86-TSB	0	185	0	125	9321311	45154	0.484	1	646.23	11	medium grained
360-U1473A-71R-2-W 55/58-TSB	0	145	0	100	10643459	44602	0.419		647.44	5	medium grained
360-U1473A-72R-2-W 73/76-TSB	0	145	0	115	9837724	62512	0.635		650.39	3	coarse grained
360-U1473A-72R-3-W 40/43-TSB	0	165	0	92	10131789	19443	0.192	0.5	651.35	8	
360-U1473A-72R-3-W 74/77-TSB	0	155	0	160	10232065	54192	0.53	0	651.69	6	medium grained
360-U1473A-73R-2-W 31/34-TSB	0	185	0	95	11073238	21080	0.19	0	653.25	5	coarse grained
360-U1473A-74R-2-W 30/36-TSB	0	155	0	75	11565973	27987	0.242	0.5	655.71	5	coarse grained
360-U1473A-74R-2-W 101/104-TSB	0	175	0	85	9811225	31776	0.341		656.42	10	medium grained
360-U1473A-74R-5-W 74/77-TSB	0	165	0	95	11918971	95969	0.805		660.09	8	medium grained
360-U1473A-74R-7-W 45/47-TSB	0	145	0	75	11504470	44898	0.39		662.39	12	medium grained
360-U1473A-75R-1-W 47/51-TSB	0	165	0	42	9895683	85846	0.914		664.77	10	medium grained
360-U1473A-75R-4-W 80/86-TSB	0	155	0	115	11901213	37960	0.319	3	668.52	8	coarse grained
360-U1473A-75R-4-W 105/109-TSB	0	135	0	85	11102074	1383992	12.466	4	668.77		medium grained
360-U1473A-75R-6-W 2/5-TSB	0	165	0	65	10302671	46934	0.456	4	670.43	14	coarse grained
360-U1473A-75R-6-W 58/62-TSB	0	135	0	75	9855532	15614	0.167	0	670.99	7	medium grained
360-U1473A-76R-3-W 1/5-TSB	0	145	0	75	11641577	12829	0.11	2	676.39	8	medium grained
360-U1473A-76R-3-W 38/42-TSB	0	165	0	130	8686163	14472	0.167	1	676.76	7	fine grained
360-U1473A-76R-3-W 53/55-TSB	0	85	0	120	10337541	4197	0.041	1	676.91	5	medium grained
360-U1473A-76R-5-W 34/38-TSB	0	145	0	35	9683242	38167	0.394	4	678.87	16	medium grained
360-U1473A-77R-2-W 56/60-TSB	0	125	0	115	12590271	330352	2.624	4	682.5	1	medium grained
360-U1473A-77R-2-W 100/102-TSB	0	145	0	53	8938445	111331	1.246	3	682.94		coarse grained
360-U1473A-78R-4-W 72/77-TSB	0	125	0	60	11299060	118651	1.05	3	688.07	4.7	coarse grained
360-U1473A-78R-4-W 132/136-TSB	0	125	0	115	9877761	186965	1.893	1	692.14	8	medium grained
360-U1473A-78R-7-W 48/51-TSB	0	105	0	100	9697256	256219	2.642		692.6	7	coarse grained
360-U1473A-78R-7-W 94/97-TSB	0	135	0	133	10337931	43919	0.425		693.52	16	medium grained
360-U1473A-78R-8-W 41/45-TSB	0	115	0	115	8620848	36255	0.421	0	694.07	20	coarse grained
360-U1473A-79R-1-W 67/71-TSB	0	145	0	79	11726632	21106	0.18		694.21	17	medium grained
360-U1473A-79R-1-W 81/87-TSB	0	125	0	125	11341496	11799	0.104		695.1	8	medium grained
360-U1473A-79R-2-W 24/27-TSB	0	125	0	129	10144058	75061	0.74	5	697.88	6	coarse grained
360-U1473A-79R-4-W 53/57-TSB	0	125	0	90	11032877	129782	1.176		699.53	8	coarse grained
360-U1473A-79R-5-W 76/79-TSB	0	135	0	80	10616451	43983	0.414	0	707.85	9	coarse grained
360-U1473A-80R-4-W 117/121-TSB	0	115	0	76	10254899	8449	0.082		708.86	7	coarse grained
360-U1473A-80R-5-W 68/71-TSB	0	85	0	70	11359595	4720	0.042		709.55	5	coarse grained
360-U1473A-80R-6-W 33/36-TSB	0	135	0	50	10657974	614323	5.764	0	711.18		coarse grained
360-U1473A-80R-7-W 111/114-TSB	0	145	0	70	9677173	1048812	12.722	1	716.51		coarse grained
360-U1473A-81R-3-W 77/80-TSB	0	95	0	74	11004092	1419001	12.895		719.47	5	coarse grained
360-U1473A-81R-5-W 77/80-TSB	0	105	0	95	9713480	29669	0.305	4	721.29	1	coarse grained
360-U1473A-81R-6-W 127/131-TSB	0	125	0	95	11209828	254994	2.275		728.41		fine grained
360-U1473A-82R-6-W 85/88-TSB	0	165	0	103	12416947	42449	0.342		729.83	15	coarse grained
360-U1473A-82R-7-W 90/94-TSB	0	125	0	117	9267600	28946	0.312		731.1	9	medium grained
360-U1473A-83R-1-W 10/14-TSB	0	155	0	77	10673295	2358844	22.1		733.09		coarse grained
360-U1473A-83R-2-W 75/77-TSB	0	105	0	80	11363751	22980	0.202	3	736.17	15	coarse grained
360-U1473A-83R-5-W 89/95-TSB	0	145	0	56	11374245	57945	0.509	4	737.98	2	coarse grained
360-U1473A-83R-7-W 66/70-TSB	0	135	0	76	11616901	211260	1.819	2	739.7	1	coarse grained
360-U1473A-83R-8-W 115/121-TSB	0	165	0	74	10930170	553248	5.062		744.9	6	medium grained
360-U1473A-84R-4-W 1/5-TSB	0	165	0	60	10917336	74971	0.687	1	748.46	6	medium grained
360-U1473A-84R-6-W 72/75-TSB	0	115	0	165	10737627	430	0.004	1	750.79		coarse grained
360-U1473A-85R-1-W 39/42-TSB	0	165	0	115	10298180	22265	0.216	0	752.28	8	medium grained
360-U1473A-85R-2-W 38/41-TSB	0	145	0	110	8866862	27820	0.314		754.19	10	coarse grained
360-U1473A-85R-3-W 94/97-TSB	0	135	0	66	9358383	1055389	11.98		754.45		coarse grained
360-U1473A-85R-3-W 120/123-TSB	0	145	0	90	10605530	859064	8.1		755.33		medium grained
360-U1473A-85R-4-W 64/68-TSB	0	135	0	75	9934034	70057	0.705		756.42	8	medium grained
379-1105A-1R-2-W 88/91-TSB-TSS	0	90	0	50	10159733	17587	0.173	2	16.96	6	fine-medium
379-1105A-1R-4-W 95/98-TSB-TSS	0	80	0	140	11297725	46595	0.412	1	19.85	7	coarse

179-1105A-1R-4-W 141/144-TSB-TSS	0	100	0	80	10876534	77997	0.717	0	20.31	0	pegmatitic
179-1105A-1R-5-1 0/5	0	130	0	40	63.887	0.03	0.046	1	20.36	3	coarse grained
179-1105A-1R-5-W 137/141-TSB-TSS_1	0	50	0	70	11928111	27674	0.232	1	21.73	11	coarse
179-1105A-2R-1-W 79/82-TSB-TSS	0	60	0	80	7345542	7912	0.108	1	24.49	4	coarse
179-1105A-3R-1-W 51/54-TSB-TSS	0	110	0	45	10715699	2184	0.02	1	29.21	5	medium
179-1105A-3R-2-W 16/20-TSB-TSS	0	90	0	80	10978568	2786	0.027	1	30.36	7	coarse
179-1105A-3R-2-W 87/91-TSB-TSS	0	90	0	30	11561126	101483	0.878	0	31.07	0	fine
179-1105A-4R-2-W 43/46-TSB-TSS	0	100	0	70	9551508	37175	0.389	0	34.91	10	coarse
179-1105A-4R-3-W 46/60-TSB-TSS	0	190	0	90	10718733	12896	0.12	0	36.28	20	medium
179-1105A-4R-4-W 57/62-TSB-TSS_1	0	100	0	50	12070166	779264	6.456	1	37.79	2	medium-coarse
179-1105A-4R-4-8 63/67	0	140	0	26	62.171	5.483	8.819	1	37.85	0	medium grained
179-1105A-5R-1-W 115/118-TSB-TSS_1	0	170	0	60	8614853	531153	6.166	2	39.45	10	pegmatitic
179-1105A-5R-1-W 144/147-TSB-TSS	0	90	0	130	10769610	1123589	10.433	4	39.74	5	fine-medium
179-1105A-5R-2-W 55/58-TSB-TSS	0	80	0	100	10709085	30895	0.288	1	40.33	0	medium
179-1105A-6R-2-W 32/36-TSB-TSS	0	80	0	60	11411340	57640	0.505	2	44.58	5	coarse
179-1105A-7R-1-1A 24/29	0	130	0	63	77.801	0.091	0.117	1	48.04	15	medium grained
179-1105A-7R-3-W 33/36-TSB-TSS	0	120	0	40	12404116	1924184	15.512	3	50.96	0	fine-medium
179-1105A-7R-4-W 30/33-TSB-TSS	0	80	0	50	9895572	26658	0.269	1	52.12	4	medium
179-1105A-8R-1-W 68/70-TSB-TSS	0	100	0	70	9326074	346405	3.714	1	53.08	0	fine-medium
179-1105A-8R-1-11 96/100	0	100	0	80	73557	0.181	0.245	1	53.36	10	medium grained
179-1105A-8R-3-W 53/56-TSB-TSS	0	100	0	40	7825722	65140	0.832	0	55.75	0	medium
179-1105A-9R-1-W 82/86-TSB-TSS	0	80	0	70	9823826	98544	1.003	1	58.22	1	fine-medium
179-1105A-9R-4-W 12/16-TSB-TSS	0	80	0	80	7679498	65143	0.848	1	61.81	20	medium
179-1105A-10R-1-W 38/42-TSB-TSS	0	70	0	80	10856048	37226	0.359	1	62.38	2	medium
179-1105A-10R-2-W 85/88-TSB-TSS_1,	0	110	0	60	6249345	541403	8.663	1	64.2	0	medium-coarse
179-1105A-10R-2-W 85/88-TSB-TSS_3,	0	90	0	41	8451991	1062278	12.568	1	64.2	0	medium-coarse
179-1105A-11R-1-5A 40/45	0	110	0	60	79.826	7.227	9.053	3	67.4	0	fine grained to medium grained
179-1105A-11R-2-W 51/54-TSB-TSS_1,	0	100	0	50	9182679	1072926	11.684	1	68.91	5	fine-medium
179-1105A-11R-2-W 129/133-TSB-TSS_	0	70	0	40	12297057	1196294	9.745	1	69.69	15	medium
179-1105A-12R-1-2 9/14	0	80	0	55	78.102	2.107	2.697	2	71.39	3	fine grained to coarse grained
179-1105A-12R-1-W 106/108-TSB-TSS	0	110	0	50	10129271	7722	0.076	0	72.36	9	medium
179-1105A-12R-2-W 50/53-TSB-TSS_1,	0	110	0	80	9269992	35723	0.385	1	73.27	10	fine
179-1105A-12R-2-W 123/127-TSB-TSS_	0	100	0	110	10712661	13416	0.125	1	74	3	fine-medium
179-1105A-13R-1-2 3/9	0	120	0	100	71.325	0.69	0.967	1	76.33	10	medium grained
179-1105A-13R-1-W 24/26-TSB-TSS_3,	0	80	0	80	12277545	133770	1.09	1	76.54	15	fine-medium
179-1105A-13R-1-W 87/89-TSB-TSS	0	100	0	40	10748744	61448	0.572	1	77.17	10	medium
179-1105A-13R-3-W 38/42-TSB-TSS_1,	0	90	0	90	7227017	52769	0.73	1	79.42	2	fine
179-1105A-13R-3-5 68/74	0	130	0	40	80.977	0.015	0.018	1	79.72	15	medium grained
179-1105A-13R-3-W 79/82-TSB-TSS_3,	0	100	0	100	12364850	279841	2.263	0	79.83	8	medium
179-1105A-14R-1-W 42/45-TSB-TSS	0	100	0	55	11354835	22947	0.202	0	81.42	10	medium
179-1105A-14R-3-W 91/94-TSB-TSS	0	90	0	70	11610342	62653	0.54	2	84.55	15	fine-medium
179-1105A-15R-1-W 113/116-TSB-TSS	0	100	0	60	13113014	671109	5.118	2	87.13	10	medium-coarse
179-1105A-15R-2-W 71/74-TSB-TSS	0	80	0	120	11173675	303350	2.715	1	88.21	5	fine-medium
179-1105A15R-3-4A 43/49	0	140	0	80	75.562	0.181	0.24	1	89.4	10	coarse grained
179-1105A-15R-3-W 83/86-TSB-TSS_3,	0	60	0	110	11747593	653658	5.564	3	89.8	12	fine-coarse
179-1105A-16R-1-W 56/58-TSB-TSS_1,	0	60	0	70	11705191	469585	4.012	2	91.16	0	fine-medium
179-1105A-16R-1-W 91/94-TSB-TSS	0	80	0	50	10376435	49932	0.481	2	91.51	10	fine
179-1105A-16R-2-W 14/17-TSB-TSS	0	60	0	110	9921482	760810	7.668	4	92.07	25	fine-coarse
179-1105A-16R-3-W 22/25-TSB-TSS	0	90	0	70	9631318	42177	0.438	0	93.56	13	medium
179-1105A-17R-2-1 0/5	0	120	0	100	63.085	0.132	0.21	1	97.02	15	medium grained
179-1105A-17R-2-W 23/26-TSB-TSS	0	70	0	80	11715185	32672	0.279	0	97.25	5	medium
179-1105A-17R-4-W 35/39-TSB-TSS	0	60	0	50	12157163	1235740	10.165	3	100.3	4	medium-coarse
179-1105A-18R-1-2 13/18	0	110	0	10	53503	0.004	0.007	1	100.33	20	medium grained
179-1105A-18R-2-W 53/57-TSB-TSS	0	50	0	60	13745140	45087	3.28	2	102.15	5	medium-coarse
179-1105A-18R-2-8 63/70	0	140	0	40	82.682	3.043	3.68	3	102.25	7	fine grained to medium grained
179-1105A-19R-2-W 65/68-TSB-TSS_1,	0	90	0	33	11340281	79394	0.7	1	107.35	26	coarse
179-1105A-19R-2-W 95/98-TSB-TSS_3,	0	70	0	30	10303374	134758	1.308	2	107.65	4	medium
179-1105A-19R-3-W 94/97-TSB-TSS	0	90	0	70	9857234	527472	5.351	2	108.99	20	medium
179-1105A-21R-1-W 49/52-TSB-TSS	0	90	0	100	11120303	102683	0.923	2	111.29	15	coarse
179-1105A-22R-1-W 103/106-TSB-TSS	0	100	0	55	11830831	350710	2.964	4	116.13	0	fine-medium
179-1105A-22R-2-W 74/78-TSB-TSS	0	120	0	60	9873206	345801	3.502	3	117.24	2	fine-coarse
179-1105A-22R-3-W 130/133-TSB-TSS	0	90	0	100	11756206	147722	1.257	1	118.98	8	medium
179-1105A-23R-1-W 94/98-TSB-TSS	0	100	0	60	11093051	263617	2.376	2	120.34	7	fine-medium
179-1105A-23R-2-W 98/101-TSB-TSS	0	70	0	70	9738398	341693	3.509	2	121.88	0	fine-coarse
179-1105A-24R-1-W 32/36-TSB-TSS	0	100	0	50	10319206	121009	1.173	2	124.72	4	medium
179-1105A-25R-1-W 26/30-TSB-TSS_1,	0	120	0	40	12534173	546747	4.362	2 (fg) and 3 (cg)	129.26	4 and 0	fine-medium
179-1105A-25R-1-W 133/137-TSB-TSS_	0	80	0	40	10619629	1139751	10.676	3	130.33	1	fine-medium
179-1105A-25R-3-W 10/13-TSB-TSS	0	120	0	80	12461041	299493	2.403	5	131.93	1	fine-medium
179-1105A-26R-3-W 80/81-TSB-TSS	0	110	0	40	9733622	36999	0.38	1	137.56	12	coarse
179-1105A-27R-1-W 27/28-TSB-TSS	0	100	0	50	8610692	33445	0.388	1	138.97	7	coarse
179-1105A-27R-3-W 93/94-TSB-TSS	0	120	0	60	9363792	53983	0.577	0	141.95	1	coarse
179-1105A-28R-1-W 98/99-TSB-TSS	0	140	0	130	8776757	41286	0.47	1	144.68	4	coarse
179-1105A-29R-1-W 102/106-TSB-TSS	0	120	0	70	10811456	185626	1.717	5	149.42	8	fine
179-1105A-29R-1-W 102/106-TSB-TSS	0	110	0	30	11399401	716270	6.317	3	149.42	8	fine-medium
179-1105A-29R-3-W 112/114-TSB-TSS	0	90	0	70	13255261	1304117	9.838	3	152.21	2	fine-medium
179-1105A-29R-4-W 31/33-TSB-TSS	0	90	0	60	21026304	745701	3.547	3	152.71	0	fine-coarse
179-1105A-30R-1-W 27/31-TSB-TSS	0	80	0	110	11699630	777993	6.65	2	153.67	0	fine
179-1105A-30R-2-W 109/113-TSB-TSS	0	80	0	60	10848875	624136	5.753	3	155.85	0	fine
179-1105A-30R-3-W 102/106-TSB-TSS	0	90	0	52	12100541	74780	0.618	3	157.12	3	fine-medium
118-735B-1D-1W-1 2/9	0	70	0	0	3.351	0.001	0.044	3 (Cg) 4 (Fg)	0.02	0	fine to coarse grained
a	0	90	0	50	1.653	0.002	0.137	3	0.02	0	coarse grained
b	0	110	0	90	1.712	0.000233	0.014	4	0.02	0	fine grained
118-735B-1D-1W-3 15/23	0	30	0	50	4.015	0.007	0.18	4	0.14	alt	fine to medium grained
118-735B-3D-1W-2 7/11	0	0	0	0	1.178	0.345	29.264	4 in middle; 3 for most	14.57	0	fine grained
118-735B-7D-2W-1 9/11	0	90	0	40	0.755	9.37E-05	0.012	3	27.53	10	fine to medium grained
118-735B-8D-1W-5 29/32	0	20	0	60	0.945	0.009	0.931	2 at top; 3 on bottom; 4 at contact	29.49	10	fine to coarse grained
a	0	40	0	62	0.271	0.000188	0.069	2	29.49	10	coarse
b	0	10	0	250	0.283	0.01	3.827	4	26.49	10	fine
c	0	10	0	204	0.389	0.000741	0.191	3	26.49	10	medium
118-735B-11D-1W-1 6/8	0	20	0	30	0.776	0.064	10.789	4	39.26	20	fine to medium grained
118-735B-12R-3W-1 8/10	0	110	0	68	0.762	0.000205	0.027	3	42.36	15	fine to medium grained
118-735B-13R-1W-1 18 102/105	0	80	0	90	0.487	0.000635	0.11	5 in middle; 4 main	45.52	20	fine to medium grained
a	0	90	0	160	0.048	0.000183	0.381	5	45.52	20	fine
b	0	70	0	130	0.433	0.000646	0.149	4	45.52	20	medium
118-735B-14R-3W-2A 31/35	0	8	0	0	3.72	0.127	3.414	4	54	alt	fine to coarse grained
118-735B-15R-1W-7B 90/93	0	30	0	2	2.625	0.005	0.182	3	57.1	alt	fine to coarse grained
118-735B-16R-4W-5 77/79	0	60	0	190	0.768	5.6E-06	0.000723	3 half; 2 half	66.91	0	fine to medium grained
a	0	90	0	70	0.224	0	0	3	66.91	0	fine
b	0	110	0	180	0.539	1.66E-05	0.003	2	66.91	0	medium
118-735B-19R-3W-12A 128/132	0	80	0	100	3.69	0.00061	0.017	3	78.89	10	fine to medium grained
118-735B-19R-5W-16 126/129	0	140	0	70	0.78	4.03E-05	0.005	1	81.82	alt, but was high	fine grained
118-735B-27R-1W-8B 84/88	0	90	0	30	0.595	1.11E-05	0.002	1	122.34	5	coarse grained
118-735B-30R-5W-6A 91/93	0	40	0	80	0.765	0.008	1.069	3 half; 2 half	143.31	3	fine to coarse grained

a	0	40	0	50	0.461	0.007	1.619	3	143.31	3	fine
b	0	140	0	50	0.314	0.000224	0.071	2	143.31	3	coarse
118-735B-31R-2W-2B 40/45	0	50	0	60	3.755	0.001	0.029	2	145.4	5	medium to coarse grained
118-735B-34R-2W-1C 18/22	0	140	0	70	1.139	0.000569	0.05	1	159.98	20	medium grained
118-735B-35R-5W-5E 131/133	0	120	0	50	0.777	0.000484	0.062	2	170.6	10	medium grained
118-735B-36R-2W-1A 11/13	0	20	0	10	0.777	0.019	2.4	1	172.61	7	coarse grained
118-735B-36R-2W-1E 98/102	0	110	0	120	3.607	0.000554	0.015	2	173.48	15	coarse grained
118-735B-36R-3W-1C 36/38	0	50	0	40	0.778	0.006	0.71	2 with ol; 1 on other	174.13	on one side; 0 on oth	fine grained with ol; medium grained no ol
a	0	40	0	120	0.436	0.006	1.427	2	174.13	20	fine
b	0	50	0	90	0.34	0.001	0.403	1	174.13	0	medium
118-735B-37R-3W-4 80/82	0	10	0	1	0.77	0.049	6.378	2	179.55	0	fine to medium grained
118-735B-38R-2W-4B 78/84	0	50	0	120	4.341	0.023	0.518	2	183.28	20	coarse grained
118-735B-40R-4W-1A 1/5	0	80	0	2	1.147	0.009	0.782	2	194.4	15	fine grained
118-735B-41R-4W-1A 20/27	0	80	0	90	4.157	0.004	0.089	2	199.47	15	medium grained
118-735B-42R-2W-3D 119/122	0	100	0	90	0.772	0.004	0.578	2	203.62	10	fine grained
118-735B-46R-2W-7B 128/130	0	0	0	10	0.584	0.174	29.828	3	223.71	0	fine to medium grained
118-735B-46R-3W-2D 24/28	0	25	0	100	3.13	0.293	9.364	3 top R; 5 in middle; 2 bottom L	224.17	5	fine to medium grained
a	0	80	0	50	0.3	4.58E-05	0.015	3	224.17	5	medium
b	0	20	0	70	1.53	0.204	13.31	5	224.17	5	fine
c	0	40	0	40	1.273	0.041	3.205	2	224.17	5	fine
118-735B-47R-4W-5 80/86	0	140	0	100	3.281	0.002	0.046	2	231.17	15	medium to coarse grained
118-735B-48R-1W-3B 42/46	0	10	0	0	3.447	0.385	11.17	2	235	0	medium grained
118-735B-53R-1W-2C 47/54	0	10	0	60	3.68	0.492	13.375	3	253.47	0	fine to medium grained
118-735B-56R-2W-1C 33/35	0	60	0	28	0.762	0.004	0.57	1	282.08	10	medium grained
118-735B-58R-3W-1F 107/114	0	90	0	70	3.713	0.005	0.133	2	284.32	10	coarse grained
118-735B-62R-1W-3 91/94	0	140	0	100	3.045	0.002	0.05	1	301.41	8	coarse grained
118-735B-63R-3W-3C 80/82	0	110	0	40	0.749	0.000561	0.076	1	309.03	10	medium grained
118-735B-65R-3W-1D 54/56	0	100	0	90	3.012	0.004	0.136	2	323.14	10	coarse grained
118-735B-66R-3W-8B 66/68	0	100	0	90	0.959	2.01E-05	0.002	1	328.41	3	coarse grained
118-735B-69R-3W-5C 86/92	0	130	0	30	3.662	0.000555	0.015	1	344.46	10	medium grained
118-735B-71R-3W-1A 0/5	0	130	0	75	2.799	0.000441	0.016	1	353.85	10	medium grained
118-735B-72R-2W-1D 56/62	0	120	0	1	2.879	0.005	0.161	1	358.06	7	medium to coarse grained
118-735B-73R-3W-4 73/75	0	50	0	150	0.667	8.33E-05	0.012	1	369.13	5	medium grained
118-735B-75R-6W-3 75/77	0	130	0	40	0.758	0.004	0.481	1	392.25	15	medium grained
118-735B-83R-4W-5A 95/97	0	140	0	102	0.679	0.000534	0.079	3	457.85	15	fine to medium grained
118-735B-83R-7W-4D 77/81	0	120	0	50	2.976	0.024	0.806	3	462.02	60	medium grained
118-735B-84R-3W-1B 14/16	0	100	0	100	0.734	0.000176	0.024	2	465.07	15	fine to medium grained
118-735B-85R-4W-1B 9/11	0	70	0	100	0.78	3.12E-05	0.004	4	475.83	0	fine to coarse grained
118-735B-86R-6W-1 9 143/145	0	40	0	100	0.765	0.021	2.694	4	486.28	5 (alt)	fine to coarse grained
118-735B-87R-5W-3 20/22	0	10	0	10	0.769	0.206	26.781	4	496.54	0	fine to medium grained
118-735B-87R-7W-6 51/55	0	160	0	90	0.877	0.000245	0.0028	1	499.65	35	medium grained
176-735B-88R-2-1 8/13	0	90	0	10	65.454	0.03	0.046	1	506.15	20	coarse grained
176-735B-90-6 4 A 72/77	0	125	0	80	69.28	0.456	0.659	1	515.23	25	coarse grained
176-735B-91R-1-2A 25/31	0	100	0	100	66.832	0.293	0.348	1	517.65	20	medium grained
176-735B-91R-1-2A 25/31	0	120	0	70	58.164	0.083	0.143	1	517.65	20	medium grained
176-735B-91R-1-2A 25/31	0	120	0	50	36.712	0.099	0.27	1	517.65	20	medium grained
176-735B-94-3-1 1 109/114	0	84	0	90	62.739	0.361	0.576	2	540.28	3	medium to coarse grained
176-735B-95R-2-1A 20/25	0	100	0	50	72.887	0.048	0.067	5	546	5	fine to medium grained
176-735B-95-2-1C 63/69	0	105	0	90	68.164	0.251	0.369	3	546.57	10	fine to medium grained
176-735B-95R-2-1D 71/78	0	110	0	40	73.577	0.154	0.209	3	546.65	5	fine grained
176-735B-99-3-6A 102/107	0	135	0	69	68.249	0.22	0.322	1	568.83	3	coarse grained
176-735B-101-3-1G 82/87	0	105	0	94	67.068	0.171	0.255	1	588.44	5	coarse grained
176-735B-103-2-3E 94/99	0	115	0	79	68.48	0.097	0.141	1	597.13	5	coarse grained
176-735B-103-3-7C 141/146	0	65	0	58	61.356	0.274	0.447	2	599.06	2	fine to coarse grained
176-735B-105R-1-8A 43/52	0	130	0	50	46.482	0.421	0.906	2	609.23	10	medium grained
176-735B-105R-1-8A 43/52	0	130	0	46	76.561	0.258	0.337	2	609.23	10	medium grained
176-735B-107-1-3C 90/95	0	125	0	60	67.167	0.071	0.106	1	620.4	0	coarse grained
176-735B-109R-2-5A 84/90	0	150	0	50	77.074	0.133	0.173	1	631.04	5	medium grained
176-735B-109-3-1A 10/15	0	105	0	88	68.817	0.293	0.426	1	631.58	3	coarse grained
176-735B-114-1-6B 84/90	0	95	0	73	76.35	7.934	10.392	1	653.24	0	coarse grained
176-735B-114-2-3 109/114	0	125	0	60	73.828	0.451	0.611	2	654.99	5	medium grained
176-735B-114R-5-1C 53/58	0	100	0	50	85.869	2.852	3.333	4	658.74	5	fine to medium grained
176-735B-115R-4-3C 69/77	0	160	0	60	68.343	9.847	14.409	2	667.01	0	fine to medium grained
176-735B-115R-7-4 61/68	0	140	0	60	83.972	0.095	0.113	2	671.09	5	coarse grained
176-735B-117R-1-2B 24/30	0	130	0	76	75.023	0.542	0.722	2	681.44	0	fine to medium grained
176-735B-117R-3-1A 9/14	0	120	0	37	78.521	0.043	0.055	4	684.26	5	fine to medium grained
176-735B-119R-1-9 97/101	0	130	0	30	75.651	0.812	1.074	4	701.37	0	fine to medium grained
176-735B-120R-3-1 1/6	0	130	0	60	63.879	0.091	0.143	1	712.94	10	medium grained
176-735B-120R-3-1 1/6	0	150	0	40	28.705	0.034	0.117	1	712.94	10	medium grained
176-735B-120R-3-1 1/6	0	140	0	80	68.683	0.166	0.242	1	712.94	10	coarse to medium grained
176-735B-121-6-1C 37/42	0	105	0	53	65.386	5.681	8.689	0	727.08	0	coarse grained
176-735B-121R-7-2A 55/62	0	130	0	80	75.377	0.477	0.632	1	728.59	25	coarse grained
176-735B-123-3-1C 53/64	0	115	0	65	70.198	0.144	0.204	0	742.47	20	medium to coarse grained
176-735B-123R-4-3 98/103	0	140	0	100	67.552	0.149	0.22	0	744.16	10	medium grained
176-735B-123R-4-3 98/103	0	150	0	80	75.366	0.189	0.251	1	744.16	10	medium to coarse grained
176-735B-123R-4-3 98/103	0	140	0	70	41.714	0.056	0.133	1	744.16	10	medium grained
176-735B-123-4-3 106/11	0	105	0	73	69.749	0.173	0.247	0	744.24	10	medium grained
176-735B-124-1-2B 48/53	0	125	0	50	77.161	0.108	0.14	1	749.18	15	medium grained
176-735B-126-4-3A 90/95	0	104	0	68	58.745	0.134	0.228	1	760.4	5	coarse grained
176-735B-127-3-3 113/117	0	120	0	70	74.604	1.335	1.79	1	768.75	20	coarse grained
176-735B-127-6-4 27/34	0	105	0	90	65.488	0.264	0.403	1	771.9	3	coarse grained
176-735B-130-1-754/59	0	120	0	80	63.852	0.132	0.207	2	794.44	10	coarse grained
176-735B-130-4-3 23/28	0	140	0	78	66.343	0.3	0.452	1	798.37	30	coarse grained
176-735B-130R-5-2 14/19	0	140	0	66	81.298	0.528	0.649	2	799.74	5	medium grained
176-735B-130R-5-2 14/19	0	120	0	52	85.293	0.034	0.096	1	799.74	5	medium
176-735B-130R-5-2 14/19	0	100	0	60	63.103	0.363	0.576	1	799.74	5	medium
176-735B-131R-2-1 2 97/103	0	130	0	46	63.588	0.143	0.225	2	805.97	5	medium to coarse grained
176-735B-132-1-12 107/112	0	110	0	70	60.015	2.009	3.348	1	814.27	0	medium to coarse grained
176-735B-132-1-14 130/135	0	125	0	50	69.407	0.53	0.763	3	814.5	20	fine to coarse grained
176-735B-133R-1-5A 76/82	0	150	0	70	77.231	3.259	4.22	3	823.66	0	fine to medium grained
176-735B-133R-2-2 40/45	0	100	0	70	35.011	0.039	0.111	2	824.64	15	medium to coarse grained
176-735B-133R-2-2 40/45	0	130	0	60	47.423	0.191	0.402	2	824.64	10	medium
176-735B-134R-5-1A 0/8	0	150	0	70	56.87	0.111	0.195	3	838.11	10	fine to medium grained
176-735B-134-5-1B 70/75	0	145	0	90	70.06	0.418	0.597	3	838.81	10	fine to medium grained
176-735B-135R-2-3A 88/95	0	130	0	50	60.267	0.042	0.069	2	844.55	5	fine grained
176-735B-136-2-2 127/133	0	120	0	70	65.971	0.081	0.122	1	849.4	10	coarse grained
176-735B-137-3-2A 46/51	0	110	0	78	63.765	0.063	0.1	1	854.58	5	coarse grained
176-735B-137R-3-4A 125/128	0	150	0	80	61.849	0.137	0.221	2	856.18	20	fine to medium grained
176-735B-137-5-1B 30/36	0	100	0	54	74.13	0.146	0.197	1	857.31	5	coarse grained
176-735B-137-6-1D 52/58	0	100	0	60	65.149	4.31	6.615	1	858.84	0	coarse grained
176-735B-137R-4-2B 64/70	0	170	0	40	1.346	0.012	0.888	1	859	25	fine grained
176-735B-137R-4-2B 64/70	0	100	0	35	76.159	0.905	1.189	1	859	35	fine grained
176-735B-137R-6-5A 108/112	0	150	0	42	47.588	0.174	0.365	3	859.4	30	fine to coarse grained

176-735B-137-6-6B 128/131	0	130	0	86	62.361	5.387	8.638	3	859.6	15	fine to medium grained
176-735B-138-3-2B 86/90	0	120	0	60	69.823	0.502	0.719	2	864.84	10	fine to coarse grained
176-735B-138-7-248/53	0	100	0	110	60.939	0.445	0.73	2	870	15	coarse grained
176-735B-139-1-5 108/114	0	110	0	50	65.747	0.063	0.096	3	872.18	5	fine to medium grained
176-735B-139R-4-25 7/65	0	140	0	90	76.286	0.302	0.396	2	875.88	15	medium grained
176-735B-139R-4-3 81/87	0	180	0	94	1.181	0.0007	0.06	2	876.12	20	medium grained
176-735B-139-7-2A 36/43	0	100	0	65	57.486	0.416	0.724	1	879.49	5	medium grained
176-735B-140-4-2 34/40	0	100	0	76	72.13	0.338	0.469	2	884.56	15	medium grained
176-735B-142-1-1 6/12	0	100	0	77	81.439	0.127	0.156	2	892.96	5	coarse grained
176-735B-142R-2-3B 96/103	0	150	0	80	86.683	0.931	0.382	3	895.19	10	fine to coarse grained
176-735B-142-4-7 117/122	0	110	0	97	67.137	0.289	0.43	3	898.21	0	fine to medium grained
176-735B-142-6-1B 41/47	0	106	0	83	59.732	0.471	0.789	2	899.82	3	medium to coarse grained
176-735B-143-5-2A 46/54	0	100	0	75	65.151	0.14	0.215	1	908.34	5	medium to coarse grained
176-735B-144-4-2A 66/71	0	90	0	130	62.691	0.489	0.78	1	917.09	5	medium to coarse grained
176-735B-146-1-2 14/21	0	56	0	136	68.475	1.383	2.019	3	931.64	5	fine to medium grained
176-735B-147-1-2 73/83	0	110	0	90	68.213	0.481	0.705	2	941.93	5	fine to coarse grained
176-735B-147-4-1A 6/15	0	70	0	70	78.699	1.395	1.773	3	944.46	25	medium to coarse grained
176-735B-148R-5-1 21/28	0	130	0	70	96.009	0.648	0.675	4	956.89	10	fine to coarse grained
176-735B-149R-6-1 21/28	0	140	0	60	81.461	0.076	0.093	1	967.29	5	medium grained
176-735B-152R-4-3A 78/88	0	140	0	66	59.026	0.04	0.068	3	992.09	10	fine to coarse grained
176-735B-154R-6-1 21/28	0	140	0	80	78.142	0.097	0.124	1	1011.88	5	medium grained
176-735B-155-1-1 1/6	0	120	0	58	71.255	0.276	0.388	2	1015.01	15	medium grained
176-735B-155R-4-2D 102/112	0	120	0	110	55.978	0.131	0.233	1(left) 5(middle) 3(right)	1020.29	10	fine to coarse grained
176-735B-156-2-4 120/125	0	80	0	90	63.063	0.122	0.194	1	1026.83	3	medium to coarse grained
176-735B-156-4-4 106/111	0	120	0	62	66.612	0.139	0.209	1	1029.6	8	medium grained
176-735B-157-3-2A 40/47	0	118	0	70	75.563	0.318	0.421	1	1037.67	5	coarse grained
176-735B-157-5-6B 121/126	0	116	0	64	75.234	3.808	4.999	1	1041.48	15	medium to coarse grained
176-735B-158-3-4A 71/76	0	80	0	95	67.926	0.356	0.523	2	1047.42	5	medium to coarse grained
176-735B-159-1-9 121/125	0	120	0	50	65.301	0.38	0.581	2	1054.91	5	fine to coarse grained
176-735B-159-2-1A 8/14	0	100	0	80	70.314	0.193	0.275	1	1055.08	10	medium to coarse grained
176-735B-159-6-3 64/70	0	126	0	90	65.746	0.142	0.216	1	1061.45	15	medium grained
176-735B-159-6-4A 89/92	0	100	0	120	53.341	0.494	0.925	1	1061.7	30	medium to coarse grained
176-735B-161-4-3A 80/86	0	120	0	90	66.952	0.178	0.265	2	1077.96	20	fine to coarse grained
176-735B-161-6-2B 34/42	0	130	0	60	61.568	0.062	0.101	1	1080.28	3	medium to coarse grained
176-735B-162R-2-1A 16/22	0	130	0	80	71.64	0.325	0.454	1	1084.01	10	medium grained
176-735B-164R-1-4B 73/79	0	140	0	58	78.543	0.119	0.151	1	1100.13	5	medium grained
176-735B-166-6-9A 131/139	0	120	0	100	73	0.194	0.265	2	1118.7	0	medium to coarse grained
176-735B-169R-4-2A 34/36	0	130	0	90	71.377	0.097	0.136	1	1143	10	medium grained
176-735B-170R-7-7 49/54	0	140	0	80	66.621	0.034	0.051	1	1156	0	fine grained
176-735B-170R-7-8B 63/71	0	140	0	70	53.723	0.071	0.131	1	1158.14	5	fine grained
176-735B-171-3-3A 62/67	0	100	0	52	66.802	0.324	0.485	1	1162.57	5	medium to coarse grained
176-735B-171-4-2 25/32	0	110	0	70	69.232	0.818	1.181	3	1163.66	5	medium to coarse grained
176-735B-171-5-2 80/85	0	130	0	70	68.229	0.421	0.618	2	1165.71	3	medium to coarse grained
176-735B-172-3-2 105/111	0	100	0	90	71.062	0.945	1.329	2	1172.44	5	coarse grained
176-735B-172R-5-1 6/14	0	160	0	80	76.003	0.896	1.176	1	1174.22	25	coarse grained
176-735B-173-2-4 108/113	0	130	0	31	66.682	0.144	0.216	2	1180.98	3	medium to coarse grained
176-735B-173-5-8 122/127	0	110	0	60	69.088	0.244	0.353	1	1185.25	3	medium to coarse grained
176-735B-175-1-5 115/120	0	80	0	69	71.837	1.073	1.494	1	1192.25	10	coarse grained
176-735B-176-2-2 102/107	0	140	0	62	59.17	0.924	1.561	1	1199.15	5	coarse grained
176-735B-177-1-6 93/98	0	120	0	75	67.425	0.189	0.28	1	1202.69	15	coarse grained
176-735B-180-5-2 21/28	0	120	0	90	81.248	0.598	0.736	1	1236.49	0	coarse grained
176-735B-185-3-2B 121/126	0	90	0	70	65.105	0.217	0.333	1	1282.27	10	coarse grained
176-735B-186-3-2 111/117	0	130	0	115	60.459	1.944	3.216	0	1292.28	25	coarse grained
176-735B-186-5-2 80/87	0	110	0	70	65.231	0.9	1.38	1	1294.92	0	coarse grained
176-735B-187R-3-3B 133/139	0	150	0	110	78.337	0.407	0.519	1	1301.13	15	medium grained
176-735B-189R-3-2 103/110	0	160	0	80	71.811	0.07	0.097	1	1320.26	5	medium grained
176-735B-189R-7-1C 92/103	0	160	0	110	76.335	0.16	0.21	1	1325.55	10	medium grained
176-735B190R-1-2 97/103	0	130	0	120	48.835	0.328	0.672	2	1327.07	10	medium to coarse grained
176-735B-191-1-3 57/64	0	120	0	60	70.659	0.181	0.257	1	1335	5	medium to coarse grained
176-735B-191-2-1 2/7	0	100	0	110	62.937	0.322	0.512	1	1337.22	3	medium to coarse grained
176-735B-194R-3-2 100/107	0	130	0	80	54.881	0.292	0.533	1	1364.13	10	medium to coarse grained
176-735B-195R-1-4 36/43	0	130	0	70	77.168	0.073	0.094	1	1364.46	10	medium grained
176-735B-195R-8-1 18/25	0	110	0	130	91.027	0.615	0.675	1	1373.54	20	coarse grained
176-735B-199-4-3 28/35	0	100	0	65	65.605	0.028	0.042	1	1396.91	10	medium grained
176-735B199R-6-1 5/10	0	120	0	50	67.262	0.081	0.12	1	1399.68	15	coarse grained
176-735B-199R-6-2 44/46	0	130	0	45	74.064	0.122	0.165	1	1400.07	20	coarse grained
176-735B-199-6-6 115/120	0	90	0	70	68.768	0.461	0.671	1	1400.78	15	medium grained
176-735B-200-1-2 12/16	0	100	0	95	58.655	0.281	0.479	1	1402.12	25	medium grained
176-735B-200R-4-1B 29/36	0	140	0	60	71.818	0.079	0.11	2	1406.49	5	medium to coarse grained
176-735B-200-4-7 113/120	0	100	0	130	60.039	0.274	0.457	1	1407.33	15	coarse grained
176-735B-200-5-1 8/14	0	100	0	70	70.945	0.167	0.236	2	1407.78	20	coarse grained
176-735B-201-5-1 9/16	0	90	0	110	64.964	0.022	0.033	1	1416.75	0	coarse grained
176-735B-202R-8-1D 23/28	0	120	0	40	60.239	0.077	0.128	1	1430.78	5	fine grained
176-735B-202R-8-1D 23/28	0	130	0	70	34.474	0.24	0.696	1	1430.78	5	fine grained
176-735B-202R-8-1D 23/28	0	130	0	12	0.922	0.003	0.351	1	1430.78	20	fine grained
176-735B-204-1-3B 47/53	0	120	0	80	80.722	0.413	0.412	1	1440.97	10	medium grained
176-735B-206-4-3 90/97	0	100	0	80	68.274	0.022	0.032	1	1464.4	0	medium to coarse grained
176-735B-206R-4-3 123-129	0	150	0	60	73.03	0.096	0.132	1	1464.73	7	medium grained
176-735B-206-7-2 5/10	0	140	0	70	74.828	0.158	0.211	2	1467.9	10	coarse grained
176-735B-206R-7-3 35/42	0	150	0	85	69.406	0.488	0.704	1	1468.2	10	medium to coarse grained
176-735B-207-1-1C 18/24	0	110	0	100	76.537	0.433	0.565	2	1469.68	10	medium grained
176-735B-207R-4-1A 33/39	0	140	0	80	75.659	0.137	0.181	1	1473.4	5	medium to coarse grained
176-735B-207R-4-1B 76/81	0	150	0	45	73.628	0.044	0.06	1	1473.83	5	fine to coarse grained
176-735B-207R-6-2A 73/81	0	140	0	45	72.075	0.028	0.038	1	1476.65	5	coarse grained
176-735B-208R-2-1A 1/9	0	120	0	75	93.214	0.122	0.131	1	1480.15	10	coarse grained
176-735B-208-6-1 23/30	0	100	0	90	70.67	0.115	0.163	1	1485.54	0	coarse grained
176-735B-208R-6-2 64/71	0	140	0	80	75.405	0.201	0.266	3	1485.95	10	fine to coarse grained
176-735B-209R-2-1F 93/98	0	150	0	80	77.366	0.122	0.157	1	1490.67	3	medium to coarse grained
176-735B-209R-7-1 4/10	0	150	0	18	87.744	0.097	0.111	1	1496.23	20	coarse grained
176-735B-209R-7-1 30/37	0	140	0	50	71.236	0.246	0.346	1	1496.49	25	medium to coarse grained
176-735B-209-8-3 58/65	0	120	0	60	68.674	0.26	0.378	1	1498.19	15	coarse grained
176-735B-210R-2-8 101/108	0	150	0	50	69.953	0.191	0.274	1	1500.69	15	medium to coarse grained

REFERENCES

Agar, S., & Lloyd, G. (1997). Deformation of Fe-Ti oxides in gabbroic shear zones from the MARK area. *Proceedings of the Ocean Drilling Program, 153 Scientific Results Proceedings of the Ocean Drilling Program, 153,* 123-141. doi:10.2973/odp.proc.sr.153.009.1997

Allerton, S., & Tivey, M. A. (2001). Magnetic polarity structure of the lower oceanic crust. *Geophysical Research Letters, 28*(3), 423-426. doi:10.1029/2000gl008493

Atkinson, B. K. (1977). The kinetics of ore deformation: Its illustration and analysis by means of deformation-mechanism maps. *Geologiska Foereningan i Stockholm. Foerhandlingar, 99*(2), 186-197. doi:10.1080/1103589770945501

Baines, A. G., Cheadle, M. J., John, B. E., & Schwartz, J. J. (2008). The rate of oceanic detachment faulting at Atlantis Bank, SW Indian Ridge. *Earth and Planetary Science Letters, 273*(1-2), 105-114. doi:10.1016/j.epsl.2008.06.013

Baines, A. G., Cheadle, M. J., John, B. E., Grimes, C. B., Schwartz, J. J., & Wooden, J. L. (2009). SHRIMP Pb/U zircon ages constrain gabbroic crustal accretion at Atlantis Bank on the ultraslow-spreading Southwest Indian Ridge. *Earth and Planetary Science Letters,287*(3-4), 540-550. doi:10.1016/j.epsl.2009.09.002

Bateman, A. M. (1951). The formation of late magmatic oxide ores. *Economic Geology, 46*(4), 404-426. doi:10.2113/gsecongeo.46.4.404

Bernard Charlier, Olivier Namur, Olivier Bolle, Rais Latypo, Jean-Clair Duchesne (2015). Fe–Ti–V–P ore deposits associated with Proterozoic massif-type anorthosites and related rocks. *Earth-Science Reviews, 141. 56-81.*

Bowen, N. L. (1920). Differentiation by Deformation. *Proceedings of the National Academy of Sciences*,6(4), 159-162. doi:10.1073/pnas.6.4.159

Clague, D. A., Frey F. A., Thompson G., Rindge, S. (1981). Minor and trace element geochemistry of volcanic rocks dredged from the Galapagos Spreading Center Role of crystal fractionation and mantle heterogeneity. *J. Geophys*, 86, 9469-9482.

Daniel Adler, Duncan Murdoch and others (2017). rgl: 3D Visualization Using OpenGL. *R package version 0.98.1*. https://CRAN.R-project.org/package=rgl

Davis, G. H. (1983). Shear-zone model for the origin of metamorphic core complexes. *Geology*, 11(6), 342-347. doi:10.1130/0091-7613(1983)112.0.co;2

Dick, H. J., Natland, J. H., Alt, J. C., Bach, W., Bideau, D., Gee, J. S., . . . Yoshinobu, A. (2000). A long in situ section of the lower ocean crust: Results of ODP Leg 176 drilling at the Southwest Indian Ridge. *Earth and Planetary Science Letters*, *179*(1), 31-51. doi:10.1016/s0012-821x(00)00102-3

Dick, H., Meyer, P., Bloomer, S., Kirby, S., Stakes, D., & Mawer, C. (1991). Lithostratigraphic Evolution of an In-Situ Section of Oceanic Layer 3. *Proceedings of the Ocean Drilling Program, 118 Scientific Results Proceedings of the Ocean Drilling Program*. doi:10.2973/odp.proc.sr.118.128.1991

Dick, H.J.B., MacLeod, C.J., Blum, P., and the Expedition 360 Scientists, (2016). *Expedition 360 Preliminary Report: Southwest Indian Ridge lower crust and Moho.* International Ocean Discovery Program. http://dx.doi.org/10.14379/iodp.pr.360.2016

Duchesne, J. C. (1996). Liquid Ilmenite or Liquidus Ilmenite: A comment on the nature of ilmenite vein deposits. *Petrology and geochemistry of magmatic suites of rocks in the continental and oceanic crusts, 73-82.*

Frank E Harrell Jr, with contributions from Charles Dupont and many others. (2016). Hmisc: Harrell Miscellaneous. *R package version 4.0-2*. https://CRAN.R-project.org/package=Hmisc

Hansen, L. N., Cheadle, M. J., John, B. E., Swapp, S. M., Dick, H. J., Tucholke, B. E., & Tivey, M. A. (2013). Mylonitic deformation at the Kane oceanic core complex: Implications for the rheological behavior of oceanic detachment faults. *Geochemistry, Geophysics, Geosystems,14*(8), 3085-3108. doi:10.1002/ggge.20184

Hennig-Michaeli, C., & Siemes, H. (1983). Compression experiments on natural magnetite crystals at 200 and 400 deg C at 400MPA confining pressure. *International Journal of Rock Mechanics and Mining Sciences & Geomechanics Abstracts, 20*(3). doi:10.1016/0148-9062(83)91378-5

Hosford, A., Tivey, M., Matsumoto, T., Dick, H., Schouten, H., & Kinoshita, H. (2003). Crustal magnetization and accretion at the Southwest Indian Ridge near the Atlantis II fracture zone, 0-25 Ma. *Journal of Geophysical Research: Solid Earth,108*(B3), 1-23. doi:10.1029/2001jb000604

John, B. E., & Cheadle, M. J. (2010). Deformation and alteration associated with oceanic and continental detachment fault systems: Are they similar? *Geophysical Monograph Series Diversity of Hydrothermal Systems on Slow Spreading Ocean Ridges*, 188th ser., 175-205. doi:10.1029/2008gm000772

John, B. E., Foster, D. A., Murphy, J. M., Cheadle, M. J., Baines, A., Fanning, C., & Copeland, P. (2004). Determining the cooling history of in situ lower oceanic crust—Atlantis Bank, SW Indian Ridge. *Earth and Planetary Science Letters, 222*(1), 145-160. doi:10.1016/j.epsl.2004.02.014

John Fox and Sanford Weisberg (2011). An R Companion to Applied Regression, Second Edition. *Sage*. URL: http://socserv.socsci.mcmaster.ca/jfox/Books/Companion

Juster, T. C., Grover T. L., Perfit, M. R. (1989) Experimental constraints on the generation of Fe-Ti basalts, andesites and rhyodacites at the Galapagos Spreading Center, 85°W and 95°W. *J. Geophys*, 94, 9215-9247.

Ligges, U. and Mächler, M. (2003). Scatterplot3d - an R Package for Visualizing Multivariate Data. *Journal of Statistical Software* 8(11), 1-20.

Lister, G. S., & Davis, G. A. (1989). The origin of metamorphic core complexes and detachment faults formed during Tertiary continental extension in the northern Colorado River region, U.S.A. *Journal of Structural Geology,11*(1-2), 65-94. doi:10.1016/0191-8141(89)90036-9

MacLeod, C.J., Dick, H.J.B., Blum, P., and the Expedition 360 Scientists. (2017). Hole 1105A redescription. *Proceedings of the International Ocean Discovery Program, 360*, 1-34. doi:10.14379/iodp.proc.360.104.2017

MacLeod, C.J., Dick, H.J.B., Blum, P., and the Expedition 360 Scientists. (2017). Site U1473. *Proceedings of the International Ocean Discovery Program, 360*, 1-136. doi:10.14379/iodp.proc.360.103.2017

Mehl, L., & Hirth, G. (2008). Plagioclase preferred orientation in layered mylonites: Evaluation of flow laws for the lower crust. *Journal of Geophysical Research, 113*(B5), 1-19. doi:10.1029/2007jb005075

Miranda, E. A., & John, B. E. (2010). Strain localization along the Atlantis Bank oceanic detachment fault system, Southwest Indian Ridge. *Geochemistry, Geophysics, Geosystems, 11*(4). doi:10.1029/2009gc002646

Muller, R. D., M. Sdrolias, C. Gaina, and W. R. Roest (2008). Age, spreading rates and spreading symmetry of the worlds ocean crust. *Geochemistry, Geophysics, Geosystems,* (9). Q04006, doi:10.1029/2007GC001743

Natland, J., Meyer, P., Dick, H., & Bloomer, S. (1991). Magmatic Oxides and Sulfides in Gabbroic Rocks from Hole 735B and the Later Development of the Liquid Line of Descent. *Proceedings of the Ocean Drilling Program, 118 Scientific Results Proceedings of the Ocean Drilling Program.* doi:10.2973/odp.proc.sr.118.163.1991

Palmiotto, C., Corda, L., Ligi, M., Cipriani, A., Dick, H. J., Douville, E., . . . Bonatti, E. (2013). Nonvolcanic tectonic islands in ancient and modern oceans. *Geochemistry, Geophysics, Geosystems,14*(10), 4698-4717. doi:10.1002/ggge.20279

Passchier, C. W., & Trouw, R. A. (2005). *Microtectonics* (p. 366). Berlin, NY: Springer.

Patrick Breheny and Woodrow Burchett (2016). visreg: Visualization of Regression Models. *R package version 2.3-0*. https://CRAN.R-project.org/package=visreg

Pettigrew, T.L., Casey, J.F., Miller, D.J. (1999). Leg 179 Summary. *Proceedings of the Ocean Drilling Program Initial Reports, 179*, 1-26. doi:10.2973/odp.proc.ir.179.1999

R Core Team (2015). R: A language and environment for statistical computing. *R Foundation for Statistical Computing*. URL https://www.R-project.org/.

Rioux, M., Cheadle, M. J., John, B. E., & Bowring, S. A. (2016). The temporal and spatial distribution of magmatism during lower crustal accretion at an ultraslow-spreading ridge: High-precision U–Pb zircon dating of ODP Holes 735B and 1105A, Atlantis Bank, Southwest Indian Ridge. *Earth and Planetary Science Letters,449*, 395-406. doi:10.1016/j.epsl.2016.05.047

Sauter, D., Sloan, H., Cannat, M., Goff, J., Patriat, P., Schaming, M., & Roest, W. R. (2011, October 02). From slow to ultra-slow: How does spreading rate affect seafloor roughness and crustal thickness? *Geology, 39*(10), 911-914. doi:10.1130/g32028.1

Schindelin, J.; Arganda-Carreras, I. & Frise, E. et al. (2012), "Fiji: an open-source platform for biological-image analysis", Nature methods 9(7): 676-682, PMID 22743772

Schneider, C. A.; Rasband, W. S. & Eliceiri, K. W. (2012), "NIH Image to ImageJ: 25 years of image analysis", Nature methods 9(7): 671-675, PMID 22930834

Schoolmeesters, N., Cheadle, M. J., John, B. E., Reiners, P. W., Gee, J., & Grimes, C. B. (2012). The cooling history and the depth of detachment faulting at the Atlantis Massif oceanic core complex. *Geochemistry, Geophysics, Geosystems, 13*(10). doi:10.1029/2012gc004314

Schroeder, T., & John, B. E. (2004). Strain localization on an oceanic detachment fault system, Atlantis Massif, 30°N, Mid-Atlantic Ridge. *Geochemistry, Geophysics, Geosystems, 5*(11). doi:10.1029/2004gc000728

Schwartz, J. J. (2005). Dating the Growth of Oceanic Crust at a Slow-Spreading Ridge. *Science, 310*(5748), 654-657. doi:10.1126/science.1116349

Shipboard Scientific Party, (1991). Site u1473A. *In* Dick, H.J.B., MacLeod, C.J., and Blum, P., Southwest Indian Ridge lower crust and Moho: the nature of the lower crust and Moho at slower spreading ridges (SloMo-Leg 1). *International Ocean Discovery Program Scientific Prospectus,* 360. http://dx.doi.org/10.14379/iodp.sp.360.2015

Shipboard Scientific Party, (1999). Site 735. *In* Dick, H.J.B., Natland, J.H., Miller, D.J., et al., *Proc. ODP, Init. Repts.,* 176: College Station, TX (Ocean Drilling Program), 1–314. doi:10.2973/odp.proc.ir.176.103.1999

Taiyun Wei and Viliam Simko (2016). corrplot: Visualization of a Correlation Matrix. *R package version 0.77.* https://CRAN.R-project.org/package=corrplot

Till, J. L., & Moskowitz, B. (2013). Magnetite deformation mechanism maps for better prediction of strain partitioning. *Geophysical Research Letters, 40*(4), 697-702. doi:10.1002/grl.50170

Twiss, R. J., & Moores, E. M. (2007). Chapter 17 Microscopic Aspects of Ductile Deformation: Mechanisms and Fabrics. In *Structural Geology* (2nd ed., pp. 500-535). New York, NY: W. H. Freeman & Company.

Yihui Xie (2017). knitr: A General-Purpose Package for Dynamic Report Generation in R. *R package version 1.16.*